



A11L.UAS.101 – A55 Identify Flight Recorder Requirements for Unmanned Aircraft Systems (UAS) Integration into the National Airspace System (NAS)

Task 3: Crash Survivability of UAS Data Recorders

July 31st, 2023

NOTICE

This document is disseminated under the sponsorship of the U.S. Department of Transportation in the interest of information exchange. The U.S. Government assumes no liability for the contents or use thereof. The U.S. Government does not endorse products or manufacturers. Trade or manufacturers' names appear herein solely because they are considered essential to the objective of this report. The findings and conclusions in this report are those of the author(s) and do not necessarily represent the views of the funding agency. This document does not constitute FAA policy. Consult the FAA sponsoring organization listed on the Technical Documentation page as to its use.

LEGAL DISCLAIMER

The information provided herein may include content supplied by third parties. Although the data and information contained herein has been produced or processed from sources believed to be reliable, the Federal Aviation Administration makes no warranty, expressed or implied, regarding the accuracy, adequacy, completeness, legality, reliability or usefulness of any information, conclusions or recommendations provided herein. Distribution of the information contained herein does not constitute an endorsement or warranty of the data or information provided herein by the Federal Aviation Administration or the U.S. Department of Transportation. Neither the Federal Aviation Administration nor the U.S. Department of Transportation shall be held liable for any improper or incorrect use of the information contained herein and assumes no responsibility for anyone's use of the information. The Federal Aviation Administration and U.S. Department of Transportation shall not be liable for any claim for any loss, harm, or other damages arising from access to or use of data or information, including without limitation any direct, indirect, incidental, exemplary, special or consequential damages, even if advised of the possibility of such damages. The Federal Aviation Administration shall not be liable to anyone for any decision made or action taken, or not taken, in reliance on the information contained herein.

TECHNICAL REPORT DOCUMENTATION PAGE

1. Report No. A11L.UAS.101_A55		2. Government Accession No.		3. Recipient's Catalog No.	
4. Title and Subtitle ASSURE A55 – Identify Flight Recorder Requirements for Unmanned Aircraft Systems (UAS) Integration into the National Airspace System (NAS) Task 3: Crash Survivability of UAS Data Recorders				5. Report Date July 31st, 2023	
				6. Performing Organization Code	
7. Author(s) Javier Calderon del Rey Luis Daniel Castillo Gerardo Olivares, PhD. Luis Manuel Gomez Ana Isabel Luengo Rivero				8. Performing Organization Report No.	
9. Performing Organization Name and Address Wichita State University University of North Dakota Embry-Riddle Aeronautical University				10. Work Unit No.	
				11. Contract or Grant No. 15-C-UASA11L.UAS.101 15-C-UAS15-C-UASA11L.UAS.101	
12. Sponsoring Agency Name and Address Federal Aviation Administration 800 Independence Ave, SW Washington DC 20591				13. Type of Report and Period Covered Task 3: December 2022 – July 2023	
				14. Sponsoring Agency Code 5401	
15. Supplementary Notes					
16. Abstract The crash survivability of Flight Data Recorders (FDRs) holds significant importance in the field of aviation. These recorders must withstand extreme conditions to ensure the preservation and recovery of the aircraft flight data during and after an accident. These extreme conditions include mechanical forces, intense heat, vibrations, and other hazardous circumstances that are characteristic of crash events. This report provides insight into the level of accelerations and loads that a small FDR could observe during different impact scenarios. The results summarized in this document were obtained using validated numerical models of the sUAS and FDR systems under consideration.					
17. Key Words			18. Distribution Statement		
19. Security Classification (of this report) Unclassified		20. Security Classification (of this page) Unclassified		21. No. of Pages 228	
				22. Price	

TABLE OF CONTENTS

Chapter	Page
EXECUTIVE SUMMARY	1
1. INTRODUCTION	2
1.1 Background	2
1.2 History and current survivability standards	2
1.3 Objectives	4
2. STATE OF THE ART – SMALL FLIGHT DATA RECORDERS	5
2.1 Flight Data Recorders for Small and Medium-Sized UAS	5
2.2 Mechanical Standards for Micro SD Cards	7
3. ASSESSING MICRO SD CARD CRASH SURVIVABILITY	9
3.1 Current Ratings and Specifications for Common Micro SD Cards	9
3.2 Physical Tests	9
3.2.1 Compression	10
3.2.2 Low-Intensity Fire	14
3.2.3 Penetration Resistance	15
3.2.4 Physical Tests Key Findings Summary	19
4. NUMERICAL METHODS FOR SHOCK SURVIVABILITY OF ELECTRONIC DEVICES	19
4.1 Literature Review	19
4.2 Preliminary Analyses	22
4.3 Low-Velocity Impact of a sUAS Electronic Board	28
4.4 Conclusions	39
5. CRASH ANALYSES OF SMALL AND MEDIUM-SIZED UAS WITH FDR	40
5.1 UAS Finite Element Models	40
5.1.1 UAS 2.55 lb. Fixed-Wing	41
5.1.2 UAS 2.7 lb. Quadcopter	43
5.1.3 UAS 55 lb. Fixed-Wing	46
5.2 Target Definition and impact Location	49

5.2.1 Aircraft Structures	49
5.2.2 Operation Over People	53
5.2.3 Moving Vehicle	54
5.2.4 Other Critical Conditions	55
5.3 IMPACT CONDITIONS DEFINITION	Error! Bookmark not defined.
5.3.1 Impact Velocity	59
5.3.2 Impact Conditions	60
5.3.3 Load Case Name Convention	60
5.3.4 Simulation Matrix	62
5.4 Analysis Results	63
5.4.1 A55-RF2.55-C1C	63
5.4.2 A55-MVQ2.7-C1C	66
5.4.3 A55-GF55-C1C	69
5.5 Results Summary	73
6. CONCLUSIONS	78
6.1 Future Research	79
7. REFERENCES	81
APPENDIX A OVERVIEW OF UAS MARKET (ERAU)	Error! Bookmark not defined.
APPENDIX B UAS TERMINAL VELOCITY	Error! Bookmark not defined.
APPENDIX C UAS IMPACT ANALYSES	Error! Bookmark not defined.

LIST OF FIGURES

Figure	Page
1. FDR for common UAS.	6
2. SferiRec LCR 100 (left) and FDR01 (right) FDRs.	7
3. Static crush test setup.	12
4. Low-intensity fire test profile.	14
5. Low-intensity fire test setup.	14
6. Penetration resistance test setup.	17
7. Commercially available CSP [30] and simplification of a similar chip using the FEM [27][29].	20
8. Discretization of the board assembly with a single CSP at the center.	23
9. Cross-sections of the detailed CSP architecture (left) and simplified FEM (right).	24
10. Finite element model of the 6-support board level assembly drop test.	25
11. 6-support drop acceleration test data for damping coefficient calibration (plot from [25]).	26
12. Ten first modes for the 6-support drop test.	26
13. Acceleration comparison for the 6-support drop test validation exercise.	27
14. Finite element model of the 4-support board level assembly drop test.	27
15. Strain ϵ_{xx} comparison for the 4-support drop test validation exercise.	28
16. Representative DJI Phantom III board assembly specimen.	29
17. Electronic components captured in the FEM.	29
18. Top, bottom, and isometric view comparisons of the board test specimen and FEM mesh.	31
19. Board assembly FEM - Materials.	31
20. Board assembly LVI - Test schematic (left) and test setup (right).	32
21. Board assembly LVI – FEM details and comparison to test setup.	33
22. LVI FEM - Ten first modes of the modal analysis.	33
23. Board assembly LVI test - IMU's failed brackets.	34
24. Board assembly LVI - Front view comparison of the test and simulation kinematics.	34
25. Board assembly LVI – Load cell data validation.	35
26. Board assembly LVI – Discrepancies between test specimen and FEM.	35
27. Board assembly LVI – Tup displacement data validation.	36
28. Board assembly LVI – Accelerometer data validation.	37

29.	Shock profile specified in ED-112 [5].	37
30.	ED-112 shock profile and shock profile obtained by Kordowski, P., et al. [43].	38
31.	Board assembly LVI – Maximum effective acceleration validation.	39
32.	NIAR Building Block Approach.	40
33.	UAS 2.55 lb. Fixed-Wing (EbeePlus) FEM.	41
34.	F2.55 FEM development process [44].	42
35.	Virtual Sensor FEM and cross-section definitions.	42
36.	F2.55 FEM modification – Virtual Sensor.	43
37.	UAS 2.7 lb. quadcopter FE model center of gravity [46].	44
38.	UAS 2.7 lb. Quadcopter FEM development process [44][45][46][48].	44
39.	A55 Q2.7lb. FEM – PCB and Virtual Sensor connections.	45
40.	Comparison of the Q2.7 FEM board assembly to the actual DJI Phantom 3.	45
41.	A16 Q2.7 FEM vs. A55 Q2.7 FEM.	46
42.	Development of the NIAR-UAS hybrid VTOL/CTOL prototype [50].	46
43.	F55 FEM development process [50].	47
44.	F55 FEM dimensions and MTOW.	48
45.	Location of the F55's VS.	48
46.	General Aviation FEM – Windshield impact location.	50
47.	General Aviation FEM – Wing impact location.	50
48.	Business Jet FEM – Vertical stabilizer impact location.	51
49.	Business Jet FEM – Wing impact location.	51
50.	Commercial Transport FEM – Horizontal stabilizer impact location.	52
51.	Commercial Transport FEM – Wing impact location.	52
52.	Rotorcraft FEM – Front cowling impact location.	53
53.	Rotorcraft FEM – Blade impact location.	53
54.	Test vs. simulation comparison of the reference Test 15 from Task A14 [44].	54
55.	Operation over people – FEM and impact location.	54
56.	Moving Vehicle – FEM and impact location.	55
57.	Masonry wall FEM.	56
58.	Surface Water FEM.	57
59.	Material inputs for material model 5 [52].	58
60.	Surface Wet Soil FEM.	58
61.	Surface Concrete FEM.	59

62.	A55-RF2.55-C1C FEM setup.	64
63.	Isometric (top) and close-up (bottom) views of the A55-RF2.55-C1C impact event at t=0s (left), t=0.005s (middle) and t=0.03s (right).	64
64.	A55-RF2.55-C1C – Virtual Sensor loads.	65
65.	A55-RF2.55-C1C – Impulse transferred to the VS.	65
66.	A55-RF2.55-C1C – Unfiltered Virtual Sensor rigid body acceleration (left) and maximum average acceleration for a 0.5ms and 3.6ms time window (right).	66
67.	A55-MVQ2.7-C1C FEM setup.	67
68.	Isometric (top) and close-up (bottom) views of the A55-MVQ2.7-C1C impact event at t=0s (left), t=0.01s (middle) and t=0.025s (right).	67
69.	A55-MVQ2.7-C1C – Virtual Sensor loads.	68
70.	A55-MVQ2.7-C1C – Impulse transferred to the VS.	68
71.	A55-MVQ2.7-C1C – Unfiltered Virtual Sensor rigid body acceleration (left) and maximum average acceleration for a 0.5ms and 6.7ms time window (right).	69
72.	A55-GF55-C1C FEM setup.	70
73.	Isometric (top) and close-up (bottom) views of the A55-GF55-C1C impact event at t=0s (left), t=0.02s (middle) and t=0.035s (right).	71
74.	A55-GF55-C1C – VS damage at the end of the analysis.	71
75.	A55-GF55-C1C – Virtual Sensor loads.	72
76.	A55-GF55-C1C – Impulse transferred to the VS.	72
77.	A55-GF55-C1C – Unfiltered Virtual Sensor rigid body acceleration (left) and maximum average acceleration for a 0.5ms and 2.6ms time window (right).	73
78.	Virtual Sensor load results categorized by UAS type.	76
79.	Virtual Sensor acceleration results categorized by UAS type.	77
80.	Compression of the PCB and Virtual Sensor by the battery for the Q2.7 sUAS.	77
81.	UAS registered in the US as of April 2022 by category [A3].	Error! Bookmark not defined.
82.	UAS manufacturers [A4].	Error! Bookmark not defined.
83.	Predicted UAS market grow [10].	Error! Bookmark not defined.
84.	Q2.7 model orientations analyzed in the CFD analyses.	Error! Bookmark not defined.
85.	Velocity contour plot at X=0m for the 30ft/s and 50ft/s Q2.7lb. CDF analyses.	Error! Bookmark not defined.
86.	Mesh sensitivity study – Coarse medium and fine meshes.	Error! Bookmark not defined.
87.	Terminal velocity and drag coefficient for the 0o, 55o, and 90o cases.	Error! Bookmark not defined.

88. Orientation and projected area used for the F2.55lb. terminal velocity calculation. **Error! Bookmark not defined.**
89. A55-GF2.55-C1C FEM setup. **Error! Bookmark not defined.**
90. Isometric (top) and close-up (bottom) views of the A55-GF2.55-C1C impact event at t=0s (left), t=0.02s (middle) and t=0.04s (right). **Error! Bookmark not defined.**
91. A55-GF2.55-C1C – Virtual Sensor loads. **Error! Bookmark not defined.**
92. A55-GF2.55-C1C – Impulse transferred to the VS. **Error! Bookmark not defined.**
93. A55-GF2.55-C1C – Unfiltered Virtual Sensor rigid body acceleration (left) and maximum average acceleration for a 0.5ms and 8.3ms time window (right). **Error! Bookmark not defined.**
94. A55-GF2.55-W1C FEM setup. **Error! Bookmark not defined.**
95. Isometric (top) and close-up (bottom) views of the A55-GF2.55-W1C impact event at t=0s (left), t=0.006s (middle) and t=0.012s (right). **Error! Bookmark not defined.**
96. A55-GF2.55-W1C – Virtual Sensor loads. **Error! Bookmark not defined.**
97. A55-GF2.55-W1C – Impulse transferred to the VS. **Error! Bookmark not defined.**
98. A55-GF2.55-W1C – Unfiltered Virtual Sensor rigid body acceleration (left) and maximum average acceleration for a 0.5ms and 1.0ms time window (right). **Error! Bookmark not defined.**
99. A55-RF2.55-B1C FEM setup. **Error! Bookmark not defined.**
100. Isometric (top) and close-up (bottom) views of the A55-RF2.55-B1C impact event at t=0s (left), t=0.0005s (middle) and t=0.001s (right). **Error! Bookmark not defined.**
101. A55-RF2.55-B1C – Virtual Sensor loads. **Error! Bookmark not defined.**
102. A55-RF2.55-B1C – Impulse transferred to the VS. **Error! Bookmark not defined.**
103. A55-RF2.55-B1C – Unfiltered Virtual Sensor rigid body acceleration (left) and maximum average acceleration for a 0.5ms and 0.2ms time window (right). **Error! Bookmark not defined.**
104. A55-BF2.55-W1C FEM setup. **Error! Bookmark not defined.**
105. Isometric (top) and close-up (bottom) views of the A55-BF2.55-W1C impact event at t=0s (left), t=0.0075s (middle) and t=0.015s (right). **Error! Bookmark not defined.**
106. A55-BF2.55-W1C – Virtual Sensor loads. **Error! Bookmark not defined.**
107. A55-BF2.55-W1C – Impulse transferred to the VS. **Error! Bookmark not defined.**
108. A55-BF2.55-W1C – Unfiltered Virtual Sensor rigid body acceleration (left) and maximum average acceleration for a 0.5ms and 1.2ms time window (right). **Error! Bookmark not defined.**
109. A55-BF2.55-V3C FEM setup. **Error! Bookmark not defined.**
110. Isometric (top) and close-up (bottom) views of the A55-BF2.55-V3C impact event at t=0s (left), t=0.0075s (middle) and t=0.015s (right). **Error! Bookmark not defined.**

111. A55-BF2.55-V3C – Virtual Sensor loads. **Error! Bookmark not defined.**
112. A55-BF2.55-V3C – Impulse transferred to the VS. **Error! Bookmark not defined.**
113. A55-BF2.55-V3C – Unfiltered Virtual Sensor rigid body acceleration (left) and maximum average acceleration for a 0.5ms and 1.2ms time window (right). **Error! Bookmark not defined.**
114. A55-CF2.55-W1C FEM setup. **Error! Bookmark not defined.**
115. Isometric (top) and close-up (bottom) views of the A55-CF2.55-W1C impact event at t=0s (left), t=0.0075s (middle) and t=0.015s (right). **Error! Bookmark not defined.**
116. A55-CF2.55-W1C – Virtual Sensor loads. **Error! Bookmark not defined.**
117. A55-CF2.55-W1C – Impulse transferred to the VS. **Error! Bookmark not defined.**
118. A55-CF2.55-W1C – Unfiltered Virtual Sensor rigid body acceleration (left) and maximum average acceleration for a 0.5ms and 1.0ms time window (right). **Error! Bookmark not defined.**
119. A55-CF2.55-H1C FEM setup. **Error! Bookmark not defined.**
120. Isometric (top) and close-up (bottom) views of the A55-CF2.55-H1C impact event at t=0s (left), t=0.0075s (middle) and t=0.015s (right). **Error! Bookmark not defined.**
121. A55-CF2.55-H1C – Virtual Sensor loads. **Error! Bookmark not defined.**
122. A55-CF2.55-H1C – Impulse transferred to the VS. **Error! Bookmark not defined.**
123. A55-CF2.55-H1C – Unfiltered Virtual Sensor rigid body acceleration (left) and maximum average acceleration for a 0.5ms and 1.7ms time window (right). **Error! Bookmark not defined.**
124. A55-GCF2.55-H1S FEM setup. **Error! Bookmark not defined.**
125. Isometric (top) and close-up (bottom) views of the A55-GCF2.55-H1S impact event at t=0s (left), t=0.0125s (middle) and t=0.025s (right). **Error! Bookmark not defined.**
126. A55-GCF2.55-H1S – Virtual Sensor loads. **Error! Bookmark not defined.**
127. A55-GCF2.55-H1S – Impulse transferred to the VS. **Error! Bookmark not defined.**
128. A55-GCF2.55-H1S – Unfiltered Virtual Sensor rigid body acceleration (left) and maximum average acceleration for a 0.5ms and 10.4ms time window (right). **Error! Bookmark not defined.**
129. A55-MVF2.55-C1C FEM setup. **Error! Bookmark not defined.**
130. Isometric (top) and close-up (bottom) views of the A55-MVF2.55-C1C impact event at t=0s (left), t=0.02s (middle) and t=0.04s (right). **Error! Bookmark not defined.**
131. A55-MVF2.55-C1C – Virtual Sensor loads. **Error! Bookmark not defined.**
132. A55-MVF2.55-C1C – Impulse transferred to the VS. **Error! Bookmark not defined.**
133. A55-MVF2.55-C1C – Unfiltered Virtual Sensor rigid body acceleration (left) and maximum average acceleration for a 0.5ms and 2.1ms time window (right). **Error! Bookmark not defined.**

134. A55-WF2.55-xxS FEM setup. **Error! Bookmark not defined.**
135. Isometric (top) and close-up (bottom) views of the A55-WF2.55-xxS impact event at $t=0s$ (left), $t=0.015s$ (middle) and $t=0.03s$ (right). **Error! Bookmark not defined.**
136. A55-WF2.55-xxS – Virtual Sensor loads. **Error! Bookmark not defined.**
137. A55-WF2.55-xxS – Impulse transferred to the VS. **Error! Bookmark not defined.**
138. A55-WF2.55-xxS – Unfiltered Virtual Sensor rigid body acceleration (left) and maximum average acceleration for a 0.5ms and 5.2ms time window (right). **Error! Bookmark not defined.**
139. A55-SWF2.55-xxS FEM setup. **Error! Bookmark not defined.**
140. Isometric (top) and close-up (bottom) views of the A55-SWF2.55-xxS impact event at $t=0s$ (left), $t=0.006s$ (middle) and $t=0.012s$ (right). **Error! Bookmark not defined.**
141. A55-SWF2.55-xxS – Virtual Sensor loads. **Error! Bookmark not defined.**
142. A55-SWF2.55-xxS – Impulse transferred to the VS. **Error! Bookmark not defined.**
143. A55-SWF2.55-xxS – Unfiltered Virtual Sensor rigid body acceleration (left) and maximum average acceleration for a 0.5ms and 1.0ms time window (right). **Error! Bookmark not defined.**
144. A55-SSF2.55-xxS FEM setup. **Error! Bookmark not defined.**
145. Isometric (top) and close-up (bottom) views of the A55-SSF2.55-xxS impact event at $t=0s$ (left), $t=0.0125s$ (middle) and $t=0.025s$ (right). **Error! Bookmark not defined.**
146. A55-SSF2.55-xxS – Virtual Sensor loads. **Error! Bookmark not defined.**
147. A55-SSF2.55-xxS – Impulse transferred to the VS. **Error! Bookmark not defined.**
148. A55-SSF2.55-xxS – Unfiltered Virtual Sensor rigid body acceleration (left) and maximum average acceleration for a 0.5ms and 1.0ms time window (right). **Error! Bookmark not defined.**
149. A55-SCF2.55-xxS FEM setup. **Error! Bookmark not defined.**
150. Isometric (top) and close-up (bottom) views of the A55-SCF2.55-xxS impact event at $t=0s$ (left), $t=0.0125s$ (middle) and $t=0.025s$ (right). **Error! Bookmark not defined.**
151. A55-SCF2.55-xxS – Virtual Sensor loads. **Error! Bookmark not defined.**
152. A55-SCF2.55-xxS – Impulse transferred to the VS. **Error! Bookmark not defined.**
153. A55-SCF2.55-xxS – Unfiltered Virtual Sensor rigid body acceleration (left) and maximum average acceleration for a 0.5ms and 1.0ms time window (right). **Error! Bookmark not defined.**
154. A55-GQ2.7-C1C FEM setup. **Error! Bookmark not defined.**
155. Isometric (top) and close-up (bottom) views of the A55-GQ2.7-C1C impact event at $t=0s$ (left), $t=0.01s$ (middle) and $t=0.02s$ (right). **Error! Bookmark not defined.**
156. A55-GQ2.7-C1C – Virtual Sensor loads. **Error! Bookmark not defined.**

157. A55-GQ2.7-C1C – Impulse transferred to the VS. **Error! Bookmark not defined.**
158. A55-GQ2.7-C1C – Unfiltered Virtual Sensor rigid body acceleration (left) and maximum average acceleration for a 0.5ms and 4.3ms time window (right). **Error! Bookmark not defined.**
159. A55-GQ2.7-W1C FEM setup. **Error! Bookmark not defined.**
160. Isometric (top) and close-up (bottom) views of the A55-GQ2.7-W1C impact event at t=0s (left), t=0.01s (middle) and t=0.02s (right). **Error! Bookmark not defined.**
161. A55-GQ2.7-W1C – Virtual Sensor loads. **Error! Bookmark not defined.**
162. A55-GQ2.7-W1C – Impulse transferred to the VS. **Error! Bookmark not defined.**
163. A55-GQ2.7-W1C – Unfiltered Virtual Sensor rigid body acceleration (left) and maximum average acceleration for a 0.5ms and 2.0ms time window (right). **Error! Bookmark not defined.**
164. A55-RQ2.7-B1C FEM setup. **Error! Bookmark not defined.**
165. Isometric (top) and close-up (bottom) views of the A55-RQ2.7-B1C impact event at t=0s (left), t=0.0004s (middle) and t=0.0007s (right). **Error! Bookmark not defined.**
166. A55-RQ2.7-B1C – Virtual Sensor loads. **Error! Bookmark not defined.**
167. A55-RQ2.7-B1C – Impulse transferred to the VS. **Error! Bookmark not defined.**
168. A55-RQ2.7-B1C – Unfiltered Virtual Sensor rigid body acceleration (left) and maximum average acceleration for a 0.5ms and 0.2ms time window (right). **Error! Bookmark not defined.**
169. A55-RQ2.7-C1C FEM setup. **Error! Bookmark not defined.**
170. Isometric (top) and close-up (bottom) views of the A55-RQ2.7-C1C impact event at t=0s (left), t=0.015s (middle) and t=0.03s (right). **Error! Bookmark not defined.**
171. A55-RQ2.7-C1C – Virtual Sensor loads. **Error! Bookmark not defined.**
172. A55-RQ2.7-C1C – Impulse transferred to the VS. **Error! Bookmark not defined.**
173. A55-RQ2.7-C1C – Unfiltered Virtual Sensor rigid body acceleration (left) and maximum average acceleration for a 0.5ms and 2.2ms time window (right). **Error! Bookmark not defined.**
174. A55-BQ2.7-W1C FEM setup. **Error! Bookmark not defined.**
175. Isometric (top) and close-up (bottom) views of the A55-BQ2.7-W1C impact event at t=0s (left), t=0.0015s (middle) and t=0.003s (right). **Error! Bookmark not defined.**
176. A55-BQ2.7-W1C – Virtual Sensor loads. **Error! Bookmark not defined.**
177. A55-BQ2.7-W1C – Impulse transferred to the VS. **Error! Bookmark not defined.**
178. A55-BQ2.7-W1C – Unfiltered Virtual Sensor rigid body acceleration (left) and maximum average acceleration for a 0.5ms and 0.9ms time window (right). **Error! Bookmark not defined.**
179. A55-BQ2.7-V3C FEM setup. **Error! Bookmark not defined.**

180. Isometric (top) and close-up (bottom) views of the A55-BQ2.7-V3C impact event at $t=0s$ (left), $t=0.0075s$ (middle) and $t=0.015s$ (right). **Error! Bookmark not defined.**
181. A55-BQ2.7-V3C – Virtual Sensor loads. **Error! Bookmark not defined.**
182. A55-BQ2.7-V3C – Impulse transferred to the VS. **Error! Bookmark not defined.**
183. A55-BQ2.7-V3C – Unfiltered Virtual Sensor rigid body acceleration (left) and maximum average acceleration for a 0.5ms and 2.1ms time window (right). **Error! Bookmark not defined.**
184. A55-CQ2.7-W1C FEM setup. **Error! Bookmark not defined.**
185. Isometric (top) and close-up (bottom) views of the A55-CQ2.7-W1C impact event at $t=0s$ (left), $t=0.0006s$ (middle) and $t=0.0013s$ (right). **Error! Bookmark not defined.**
186. A55-CQ2.7-W1C – Virtual Sensor loads. **Error! Bookmark not defined.**
187. A55-CQ2.7-W1C – Impulse transferred to the VS. **Error! Bookmark not defined.**
188. A55-CQ2.7-W1C – Unfiltered Virtual Sensor rigid body acceleration (left) and maximum average acceleration for a 0.5ms and 1.0ms time window (right). **Error! Bookmark not defined.**
189. A55-CQ2.7-H1C FEM setup. **Error! Bookmark not defined.**
190. Isometric (top) and close-up (bottom) views of the A55-CQ2.7-H1C impact event at $t=0s$ (left), $t=0.003s$ (middle) and $t=0.006s$ (right). **Error! Bookmark not defined.**
191. A55-CQ2.7-H1C – Virtual Sensor loads. **Error! Bookmark not defined.**
192. A55-CQ2.7-H1C – Impulse transferred to the VS. **Error! Bookmark not defined.**
193. A55-CQ2.7-H1C – Unfiltered Virtual Sensor rigid body acceleration (left) and maximum average acceleration for a 0.5ms and 2.2ms time window (right). **Error! Bookmark not defined.**
194. A55-GCQ2.7-H1S FEM setup. **Error! Bookmark not defined.**
195. Isometric (top) and close-up (bottom) views of the A55-GCQ2.7-H1S impact event at $t=0s$ (left), $t=0.0125s$ (middle) and $t=0.025s$ (right). **Error! Bookmark not defined.**
196. A55-GCQ2.7-H1S – Virtual Sensor loads. **Error! Bookmark not defined.**
197. A55-GCQ2.7-H1S – Impulse transferred to the VS. **Error! Bookmark not defined.**
198. A55-GCQ2.7-H1S – Unfiltered Virtual Sensor rigid body acceleration (left) and maximum average acceleration for a 0.5ms and 3.0ms time window (right). **Error! Bookmark not defined.**
199. A55-WQ2.7-xxS FEM setup. **Error! Bookmark not defined.**
200. Isometric (top) and close-up (bottom) views of the A55-WQ2.7-xxS impact event at $t=0s$ (left), $t=0.0125s$ (middle) and $t=0.025s$ (right). **Error! Bookmark not defined.**
201. A55-WQ2.7-xxS – Virtual Sensor loads. **Error! Bookmark not defined.**
202. A55-WQ2.7-xxS – Impulse transferred to the VS. **Error! Bookmark not defined.**

203. A55-WQ2.7-xxS – Unfiltered Virtual Sensor rigid body acceleration (left) and maximum average acceleration for a 0.5ms and 4.9ms time window (right). **Error! Bookmark not defined.**
204. A55-SWQ2.7-xxS FEM setup. **Error! Bookmark not defined.**
205. Isometric (top) and close-up (bottom) views of the A55-SWQ2.7-xxS impact event at t=0s (left), t=0.01s (middle) and t=0.02s (right). **Error! Bookmark not defined.**
206. A55-SWQ2.7-xxS – Virtual Sensor loads. **Error! Bookmark not defined.**
207. A55-SWQ2.7-xxS – Impulse transferred to the VS. **Error! Bookmark not defined.**
208. A55-SWQ2.7-xxS – Unfiltered Virtual Sensor rigid body acceleration (left) and maximum average acceleration for a 0.5ms and 4.7ms time window (right). **Error! Bookmark not defined.**
209. A55-SSQ2.7-xxS FEM setup. **Error! Bookmark not defined.**
210. Isometric (top) and close-up (bottom) views of the A55-SSQ2.7-xxS impact event at t=0s (left), t=0.01s (middle) and t=0.02s (right). **Error! Bookmark not defined.**
211. A55-SSQ2.7-xxS – Virtual Sensor loads. **Error! Bookmark not defined.**
212. A55-SSQ2.7-xxS – Impulse transferred to the VS. **Error! Bookmark not defined.**
213. A55-SSQ2.7-xxS – Unfiltered Virtual Sensor rigid body acceleration (left) and maximum average acceleration for a 0.5ms and 4.0ms time window (right). **Error! Bookmark not defined.**
214. A55-SCF2.55-xxS FEM setup. **Error! Bookmark not defined.**
215. Isometric (top) and close-up (bottom) views of the A55-SCQ2.7-xxS impact event at t=0s (left), t=0.01s (middle) and t=0.02s (right). **Error! Bookmark not defined.**
216. A55-SCQ2.7-xxS – Virtual Sensor loads. **Error! Bookmark not defined.**
217. A55-SCQ2.7-xxS – Impulse transferred to the VS. **Error! Bookmark not defined.**
218. A55-SCQ2.7-xxS – Unfiltered Virtual Sensor rigid body acceleration (left) and maximum average acceleration for a 0.5ms and 2.7ms time window (right). **Error! Bookmark not defined.**
219. A55-GF55-W1C FEM setup. **Error! Bookmark not defined.**
220. Isometric (top) and close-up (bottom) views of the A55-GF55-W1C impact event at t=0s (left), t=0.0125s (middle) and t=0.025s (right). **Error! Bookmark not defined.**
221. A55-GF55-W1C – Virtual Sensor loads. **Error! Bookmark not defined.**
222. A55-GF55-W1C – Impulse transferred to the VS. **Error! Bookmark not defined.**
223. A55-GF55-W1C – Unfiltered Virtual Sensor rigid body acceleration (left) and maximum average acceleration for a 0.5ms and 2.2ms time window (right). **Error! Bookmark not defined.**
224. A55-RF55-B1C FEM setup. **Error! Bookmark not defined.**

225. Isometric (top) and close-up (bottom) views of the A55-RF55-B1C impact event at $t=0s$ (left), $t=0.002s$ (middle) and $t=0.004s$ (right). **Error! Bookmark not defined.**
226. A55-RF55-B1C – Virtual Sensor loads. **Error! Bookmark not defined.**
227. A55-RF55-B1C – Impulse transferred to the VS. **Error! Bookmark not defined.**
228. A55-RF55-B1C – Unfiltered Virtual Sensor rigid body acceleration (left) and maximum average acceleration for a 0.5ms and 0.2ms time window (right). **Error! Bookmark not defined.**
229. A55-RF55-C1C FEM setup. **Error! Bookmark not defined.**
230. Isometric (top) and close-up (bottom) views of the A55-RF55-C1C impact event at $t=0s$ (left), $t=0.0081s$ (middle) and $t=0.0161s$ (right). **Error! Bookmark not defined.**
231. A55-RF55-C1C – Virtual Sensor loads. **Error! Bookmark not defined.**
232. A55-RF55-C1C – Impulse transferred to the VS. **Error! Bookmark not defined.**
233. A55-RF55-C1C – Unfiltered Virtual Sensor rigid body acceleration (left) and maximum average acceleration for a 0.5ms and 2.2ms time window (right). **Error! Bookmark not defined.**
234. A55-BF55-W1C FEM setup. **Error! Bookmark not defined.**
235. Isometric (top) and close-up (bottom) views of the A55-BF55-W1C impact event at $t=0s$ (left), $t=0.005s$ (middle) and $t=0.0071s$ (right). **Error! Bookmark not defined.**
236. A55-BF55-W1C – Virtual Sensor loads. **Error! Bookmark not defined.**
237. A55-BF55-W1C – Impulse transferred to the VS. **Error! Bookmark not defined.**
238. A55-BF55-W1C – Unfiltered Virtual Sensor rigid body acceleration (left) and maximum average acceleration for a 0.5ms and 0.8ms time window (right). **Error! Bookmark not defined.**
239. A55-BF55-V3C FEM setup. **Error! Bookmark not defined.**
240. Isometric (top) and close-up (bottom) views of the A55-BF55-V3C impact event at $t=0s$ (left), $t=0.005s$ (middle) and $t=0.0067s$ (right). **Error! Bookmark not defined.**
241. A55-BF55-V3C – Virtual Sensor loads. **Error! Bookmark not defined.**
242. A55-BF55-V3C – Impulse transferred to the VS. **Error! Bookmark not defined.**
243. A55-BF55-V3C – Unfiltered Virtual Sensor rigid body acceleration (left) and maximum average acceleration for a 0.5ms and 0.8ms time window (right). **Error! Bookmark not defined.**
244. A55-CF55-W1C FEM setup. **Error! Bookmark not defined.**
245. Isometric (top) and close-up (bottom) views of the A55-CF55-W1C impact event at $t=0s$ (left), $t=0.0025s$ (middle) and $t=0.005s$ (right). **Error! Bookmark not defined.**
246. A55-CF55-W1C – Virtual Sensor loads. **Error! Bookmark not defined.**
247. A55-CF55-W1C – Impulse transferred to the VS. **Error! Bookmark not defined.**

248. A55-CF55-W1C – Unfiltered Virtual Sensor rigid body acceleration (left) and maximum average acceleration for a 0.5ms and 1.1ms time window (right). **Error! Bookmark not defined.**
249. A55-CF55-H1C FEM setup. **Error! Bookmark not defined.**
250. Isometric (top) and close-up (bottom) views of the A55-CF55-H1C impact event at $t=0s$ (left), $t=0.005s$ (middle) and $t=0.0071s$ (right). **Error! Bookmark not defined.**
251. A55-CF55-H1C – Virtual Sensor loads. **Error! Bookmark not defined.**
252. A55-CF55-H1C – Impulse transferred to the VS. **Error! Bookmark not defined.**
253. A55-CF55-H1C – Unfiltered Virtual Sensor rigid body acceleration (left) and maximum average acceleration for a 0.5ms and 1.2ms time window (right). **Error! Bookmark not defined.**
254. A55-MVF55-C1C FEM setup. **Error! Bookmark not defined.**
255. Isometric (top) and close-up (bottom) views of the A55-MVF55-C1C impact event at $t=0s$ (left), $t=0.02s$ (middle) and $t=0.04s$ (right). **Error! Bookmark not defined.**
256. A55-MVF55-C1C – Virtual Sensor loads. **Error! Bookmark not defined.**
257. A55-MVF55-C1C – Impulse transferred to the VS. **Error! Bookmark not defined.**
258. A55-MVF55-C1C – Unfiltered Virtual Sensor rigid body acceleration (left) and maximum average acceleration for a 0.5ms and 1.7ms time window (right). **Error! Bookmark not defined.**
259. A55-WF55-xxS FEM setup. **Error! Bookmark not defined.**
260. Isometric (top) and close-up (bottom) views of the A55-WF55-xxS impact event at $t=0s$ (left), $t=0.015s$ (middle) and $t=0.03s$ (right). **Error! Bookmark not defined.**
261. A55-WF255-xxS – Virtual Sensor loads. **Error! Bookmark not defined.**
262. A55-WF55-xxS – Impulse transferred to the VS. **Error! Bookmark not defined.**
263. A55-WF55-xxS – Unfiltered Virtual Sensor rigid body acceleration (left) and maximum average acceleration for a 0.5ms and 5.4ms time window (right). **Error! Bookmark not defined.**
264. A55-SWF55-xxS FEM setup. **Error! Bookmark not defined.**
265. Isometric (top) and close-up (bottom) views of the A55-SWF55-xxS impact event at $t=0s$ (left), $t=0.0075s$ (middle) and $t=0.015s$ (right). **Error! Bookmark not defined.**
266. A55-SWF55-xxS – Virtual Sensor loads. **Error! Bookmark not defined.**
267. A55-SWF55-xxS – Impulse transferred to the VS. **Error! Bookmark not defined.**
268. A55-SWF55-xxS – Unfiltered Virtual Sensor rigid body acceleration (left) and maximum average acceleration for a 0.5ms and 1.1ms time window (right). **Error! Bookmark not defined.**
269. A55-SSF55-xxS FEM setup. **Error! Bookmark not defined.**

270. Isometric (top) and close-up (bottom) views of the A55-SSF55-xxS impact event at $t=0s$ (left), $t=0.01s$ (middle) and $t=0.02s$ (right). **Error! Bookmark not defined.**
271. A55-SSF55-xxS – Virtual Sensor loads. **Error! Bookmark not defined.**
272. A55-SSF55-xxS – Impulse transferred to the VS. **Error! Bookmark not defined.**
273. A55-SSF55-xxS – Unfiltered Virtual Sensor rigid body acceleration (left) and maximum average acceleration for a 0.5ms and 1.1ms time window (right). **Error! Bookmark not defined.**
274. A55-SCF55-xxS FEM setup. **Error! Bookmark not defined.**
275. Isometric (top) and close-up (bottom) views of the A55-SCF55-xxS impact event at $t=0s$ (left), $t=0.005s$ (middle) and $t=0.0074s$ (right). **Error! Bookmark not defined.**
276. A55-SCF55-xxS – Virtual Sensor loads. **Error! Bookmark not defined.**
277. A55-SCF55-xxS – Impulse transferred to the VS. **Error! Bookmark not defined.**
278. A55-SCF55-xxS – Unfiltered Virtual Sensor rigid body acceleration (left) and maximum average acceleration for a 0.5ms and 1.3ms time window (right). **Error! Bookmark not defined.**

LIST OF TABLES

Table	Page
1. Most common UAS in the market and their flight data recording technology.	5
2. Specifications of SferiRec LCR 100 and FDR01 FDRs.	7
3. Crash-survivability standards for traditional, lightweight, and micro SD FDRs.	8
4. Physical requirements for SD cards.	9
5. Micro SD card compression test matrix – Preliminary tests.	10
6. Micro SD card compression test matrix – Benchmark tests.	11
7. Micro SD card compression tests results – Preliminary tests manufacturer 1.	12
8. Micro SD card compression tests results – Preliminary tests manufacturer 2.	13
9. Micro SD card compression tests results – Benchmark tests.	13
10. Micro SD card low-intensity fire tests matrix – Preliminary tests.	15
11. Micro SD card low-intensity fire tests results – Benchmark tests.	15
12. Micro SD card penetration resistance test matrix – Preliminary tests.	16
13. Micro SD card penetration resistance test matrix – Benchmark tests.	16
14. Micro SD card penetration resistance tests results – Preliminary tests manufacturer 1.	17
15. Micro SD card penetration resistance tests results – Preliminary tests manufacturer 2.	18
16. Micro SD card penetration resistance tests results – Benchmark tests.	18
17. Main aspects of the data acquisition procedures in the reviewed experimental work.	21
18. Mesh quality criteria.	22
19. PCB material properties used in the FEM.	23
20. Material properties of the CSP components.	24
21. Geometry and mesh details of the modeled electronic components.	30
22. Board assembly LVI - Impact conditions.	32
23. LVI FEM - Element count.	32
24. UAS FEMs and development project.	40
25. UAS 2.55lb. Fixed-Wing specifications.	41
26. Relevant specifications of the DJI Phantom 3 [46].	43
27. Relevant specifications of the 55lb. NIAR UAS fixed-wing configuration.	47
28. Reference airborne collision studies, impact location, velocity, and severity level.	49
29. Brick and mortar material properties.	56
30. * <i>MAT_NULL</i> water properties.	57
31. Concrete properties defined for the elastic material.	59

32. A55 crash analyses – Impact velocity.	60
33. F2.55 FEM simulation matrix.	62
34. Q2.7 FEM simulation matrix.	62
35. F55 FEM simulation matrix.	63
36. A55-RF2.55-C1C element count.	63
37. A55-MVQ2.7-C1C element count.	66
38. A55-GF55-C1C element count.	69
39. Virtual Sensor load and acceleration results for the F2.55 impact analyses.	74
40. Virtual Sensor load and acceleration results for the Q2.7 impact analyses.	74
41. Virtual Sensor load and acceleration results for the F55 impact analyses.	75
42. Analysis conditions for the 30ft/s and 50ft/s Q2.7lb. CDF analyses. Error! Bookmark not defined.	
43. Mesh sensitivity study – Element count, computational time, and terminal velocity. Error! Bookmark not defined.	
44. A55-GF2.55-C1C element count.	Error! Bookmark not defined.
45. A55-GF2.55-W1C element count.	Error! Bookmark not defined.
46. A55-RF2.55-B1C element count.	Error! Bookmark not defined.
47. A55-BF2.55-W1C element count.	Error! Bookmark not defined.
48. A55-BF2.55-V3C element count.	Error! Bookmark not defined.
49. A55-CF2.55-W1C element count.	Error! Bookmark not defined.
50. A55-CF2.55-H1C element count.	Error! Bookmark not defined.
51. A55-GCF2.55-H1S element count.	Error! Bookmark not defined.
52. A55-MVF2.55-C1C element count.	Error! Bookmark not defined.
53. A55-WF2.55-xxS element count.	Error! Bookmark not defined.
54. A55-SWF2.55-xxS element count.	Error! Bookmark not defined.
55. A55-SSF2.55-xxS element count.	Error! Bookmark not defined.
56. A55-SCF2.55-xxS element count.	Error! Bookmark not defined.
57. A55-GQ2.7-C1C element count.	Error! Bookmark not defined.
58. A55-GQ2.7-W1C element count.	Error! Bookmark not defined.
59. A55-RQ2.7-B1C element count.	Error! Bookmark not defined.
60. A55-RQ2.7-C1C element count.	Error! Bookmark not defined.
61. A55-BQ2.7-W1C element count.	Error! Bookmark not defined.
62. A55-BQ2.7-V3C element count.	Error! Bookmark not defined.

63. A55-CQ2.7-W1C element count.
64. A55-CQ2.7-H1C element count.
65. A55-GCQ2.7-H1S element count.
66. A55-WQ2.7-xxS element count.
67. A55-SWQ2.7-xxS element count.
68. A55-SSQ2.7-xxS element count.
69. A55-SCQ2.7-xxS element count.
70. A55-GF55-W1C element count.
71. A55-RF55-B1C element count.
72. A55-RF55-C1C element count.
73. A55-BF55-W1C element count.
74. A55-BF55-V3C element count.
75. A55-CF55-W1C element count.
76. A55-CF55-H1C element count.
77. A55-MVF55-C1C element count.
78. A55-WF55-xxS element count.
79. A55-SWF55-xxS element count.
80. A55-SSF55-xxS element count.
81. A55-SCF55-xxS element count.

LIST OF ACRONYMS

1D	One-Dimensional
2D	Two-Dimensional
3D	Three-Dimensional
CSP	Chip Scale Package
CTOL	Conventional Take-Off and Landing
ERAU	Embry Riddle Aeronautical University
F2.55	Fixed-Wing 2.55lb. FEM
F55	Fixed-Wing 55lb. FEM
FAA	Federal Aviation Administration
FDRs	Flight Data Recorders
FE	Finite Element
FEM	Finite Element Model
IMU	Inertial Measurement Unit
LVI	Low Velocity Impact
MTOW	Maximum Take Off Weight
NAS	National Airspace System
NIAR	National Institute for Aviation Research
NRB	Nodal Rigid Body
PCB	Printed Circuit Board
Q2.7	Quadcopter 2.7lb. FEM
SD	Secure Digital
SPH	Smoothed-Particle Hydrodynamics
sUAS	Small Unmanned Aircraft System
TSOs	Technical Standard Orders
UAM	Urban Air Mobility
UAS	Unmanned Aircraft System
VS	Virtual Sensor
VTOL	Vertical Take-Off and Landing

EXECUTIVE SUMMARY

The rapid growth of small Unmanned Aircraft Systems (sUAS) operations entails an increased risk of accidents caused by or involving sUAS. As with manned aircraft, the retrieval of relevant flight data is essential in finding the causes and circumstances of such events. This data will enable the industry to improve its products and allow authorities to establish new regulations or enhance existing ones to guarantee public safety. Based on the findings summarized in the literature review task of the present work [1], it was identified that currently there is a significant gap between manned and sUAS Flight Data Recording (FDR) requirements. The causes of this gap are:

- 1) The current FDRs for sUAS do not adhere to any existing standard.
- 2) Some manufacturers attempt to enhance the product performance by considering the criteria outlined in FDR standards such as the ED-112 or the ED-155. Some of these include shock, temperature, and water resistance. However, this document shows the substantial discrepancies between these attributes' actual values and the specified in the standards.

This document summarizes the research effort conducted toward understanding the current state of the art for sUAS FDR devices and assesses their crash survivability. A detailed literature review was completed to set the building blocks of the research effort. Parallelisms between manned aircraft and sUAS FDRs were established early on to recognize and embrace the current limitations of the latter while considering the criticality of their function in modern airspace. This allowed for determining relevant physical test conditions that could be evaluated. The research effort led to the generation of physical test data from destructive and non-destructive testing of flight data storage devices commonly used in modern sUAS and to a comprehensive evaluation of different crash conditions using high-fidelity numerical simulations.

Static loading, penetration resistance (with a 3/8" spherical indenter) and low-intensity fire tests were performed using two different commercially available UAS FDRs. The FDRs remained readable for static loads up to 2,785 lb. (12,388.3N), indentation loads up to 30lb. (133.45N) and temperatures up to 200°C. Additionally, an extensive simulation matrix was defined to assess the crash survivability of sUAS FDRs. Three sUAS configurations were used: Fixed-Wing (2.55lb) (F2.55), Quadcopter (2.70lb) (Q2.7), and Fixed-Wing (55.0lb) (F55). Each aircraft's corresponding Finite Element Model (FEM) included a Virtual Sensor (VS) representative of the physical FDR system. Various impact targets were studied, including critical aircraft structures, ground vehicles, pedestrians, buildings, and different ground surfaces. Based on the numerical simulation results, the maximum loads observed at the VS were 500.2N, 910.43N, and 559.6N for the F2.55, Q2.7, and F55 sUAS, respectively. These peak loads have durations of less than a few milliseconds (0.5-3ms), which is difficult to replicate in a standard mechanical test. The maximum load observed at the VS exceeds the minimum failure load of 35lb. obtained in the penetration resistance tests for 21 out of 41 analyses. In addition, the maximum average accelerations observed for a time window of 0.5ms were 4,850g, 9,800g, and 17,500g for the F2.55, Q2.7, and F55 sUAS, respectively. Note that only in 8 of the 41 analyzed crash scenarios the acceleration values were below the critical value used as a reference by some sUAS FDR manufacturers (1,500g for 0.5ms) to test these devices. These values indicate that crash protection is vital to increase the FDR's chance of survival. The loads and acceleration levels presented in this report for the studied sUAS impact conditions can be used as a reference to define future sUAS FDR requirements.

1. INTRODUCTION

1.1 Background

The crash survivability of Flight Data Recorders (FDRs) holds significant importance in the field of aviation. These recorders must withstand extreme conditions to ensure the preservation and recovery of the aircraft flight data during and after an accident. These extreme conditions include mechanical forces, intense heat, vibrations, and other hazardous circumstances that are characteristic of crash events. By maintaining their integrity under such challenging conditions, crash-survivable FDRs play a pivotal role in providing valuable information for accident investigation, analysis, and the development of enhanced safety measures.

The exponential growth of Unmanned Aircraft Systems (UAS) operations has amplified the need for crash-survivable FDRs specific to this domain. The increased probability of UAS accidents necessitates the recovery of data from these events. However, current standards do not explicitly define the critical conditions applicable to UAS accidents, resulting in a gap between existing regulations and the unique requirements of UAS FDRs. Therefore, the development of comprehensive standards that encompass the crash survivability demands specific to UAS becomes essential. By addressing these gaps, the aviation industry can ensure the effective preservation and retrieval of data, enabling thorough accident investigations and facilitating continuous improvements in UAS safety standards.

1.2 History and current survivability standards

The history of crash survivability requirements for FDRs dates back to 1940, when the predecessor of the Federal Aviation Administration (FAA), the Civil Aeronautics Board, required that the data recorded during the flight be safeguarded beyond the crash impact [2].

The initial development of FDRs faced challenges in meeting design requirements, as early units were unable to withstand the forces and fire exposure resulting from aircraft crashes. However, with the advent of the "Jet Age" in 1958, advancements were made in FDR technology, including the introduction of Incanol Steel enclosures to protect the recorded data. While these devices were initially believed to be indestructible, several accidents revealed their limitations, prompting the need for updated crash survivability requirements [3].

To improve the chances of data recovery, significant steps were taken in refining the survivability requirements of FDRs. In 1965, the FAA increased the crash survivability requirement to a 1,000g and mandated that the FDR be positioned at the rear of the aircraft, minimizing the impact velocity [2]. These measures aimed to enhance the survivability of the FDR during crash events.

Early Technical Standard Orders (TSOs) primarily considered high-intensity and short-duration fire scenarios. However, it was observed that many cases of unrecoverable data were associated with post-impact fires. Recognizing this discrepancy, EUROCAE incorporated a low-intensity fire requirement (10 hours at 260°C) into ED-56A (December 1993), acknowledging the significance of prolonged, low-intensity post-impact fires. Moreover, the National Transportation Safety Board and the FAA further increased the survivability standards for high-intensity fires, extending the requirement from 30 minutes to 60 minutes (50,000 BTUs, 1,100°C) in TSO-C123a and TSO-C124a, in 1998 [3].

These cumulative efforts have been aimed at achieving a probability of 100% data recovery from FDRs, addressing crash forces, fire exposures, and other hazardous conditions. By continuously refining survivability requirements and incorporating lessons learned from real-world incidents, the aviation industry has made significant strides in improving the crash survivability of FDRs and enhancing their crucial role in accident investigations. As mentioned in the literature review task of the present work, the latest versions of TSO-C123 [4] and TSO-C124 [5] include:

- Impact Shock – 3,400g's for 6.5ms.
- Static Crush – 5,000 pounds for 5 minutes on each axis.
- Penetration Resistance – 500lb. dropped from 10ft. with a ¼-inch diameter contact point.
- Hydrostatic Pressure – Pressure equivalent to a depth of 20,000ft.
- Fire (High Intensity) – 1,100°C flame covering 100% of the recorder for 30 minutes. (60 minutes if ED56 test protocol is used).
- Fire (Low Intensity) – 260°C Oven test for 10 hours.
- Fluid Immersion – Immersion in aircraft fluids (fuel, oil, etc.) for 24 hours.
- Water Immersion – Immersion in sea water for 30 days.

In response to the industry's increasing pressure for lighter aircraft to incorporate FDRs, new standards were introduced, such as the EUROCAE ED-155 [7] (2009). This document defines the minimum specifications for aircraft required to carry lightweight flight recording systems. Some of these specifications include the crash survivability requirements for both general and deployable lightweight FDRs.

I) Fixed Recorder Systems

The recorder has to be capable of preserving recorded information after the following sequence of tests:

Ia.) Impact shock: The energy content of the impact shock has to be equal or greater than that contained in a half-sine wave shock of 5 ± 1 ms duration and a peak acceleration of 1,000g. This test has to be performed in all directions.

Ib.) Static crush: A load of 4.54kN (1,000lb.) for a period of 5 minutes. A minimum of 4 locations shall be tested, including (when applicable) each of the main diagonals and main faces.

Ic.) High temperature fire: The test article has to be subjected to a fire producing a minimum thermal flux of 158 kW/m^2 for a period of at least 15 minutes. The temperature may vary between 950°C and 1,100°C as long as the minimum thermal flux is maintained

II) Deployable Recorders

The recorder has to be capable of preserving recorded information after the following sequence of tests:

Ila.) Impact shock: The test article shall be subjected to an impact shock applied to the most probable landing attitude in the most damage vulnerable direction. The shock shall be such a level as to simulate a landing velocity of 25m/s (80ft/s) onto a hard surface such as rock, concrete, or steel.

Iib.) Radio Location Beacon Transmission: The deployable recorder has to be able to transmit from a shielded bag on 121.5MHz with enough power to operate for at least 150 hours.

Iic.) Seaworthiness: The deployable body must be buoyant and self-righting in fresh and salt water to keep the antenna operating normally. Confirmation of 121.5MHz transmissions shall be performed in both fresh and salt water. The conditions should replicate an open sea state 7 (Beaufort scale force 10).

Iid.) High Temperature Fire: A minimum thermal flux of 158kW/m² (50,000 Btu/ft²/hour) during at least 5 minutes.

Additionally, this document references the Standard Test Conditions as defined in documents EUROCAE ED-14F/RTCA DO-160F.

- Temperature: +15 to +35°C
- Relative Humidity: Not greater than 85%
- Ambient Pressure: 85 to 107 kPa

As of now, there are no established standards exclusively tailored to UAS FDRs. Furthermore, the limited availability of accident data for UAS makes it difficult to determine the suitability of existing crash survivability standards. Therefore, establishing specific standards and evaluating their compatibility with UAS requirements are vital steps toward enhancing safety and data recording capabilities in UAS operations.

1.3 Objectives

Considering the limitations mentioned in Section 1.2, the following objectives were specified for this research effort:

- Research what type of FDRs are used in small and medium-sized UAS. This objective is addressed in Section 2.1.
- Evaluate the current crash survivability standards for this type of FDR. This objective is addressed in Section 2.2.
- Evaluate the mechanical performance of the FDR for static crush, penetration resistance, and low-intensity fire conditions. This objective is addressed in Section 3.
- Explore numerical methods to develop predictive tools for assessing the applicability of crash survivability standards to FDRs for UAS. This objective is addressed in Section 4.
- Application of the numerical methods in different crash scenarios to predict a range of loads and accelerations that will contribute to future decision-making on FDR standards for small and medium-sized UAS. This objective is addressed in Section 5.

2. STATE OF THE ART – SMALL FLIGHT DATA RECORDERS

This chapter provides a description of the current flight data recording technology integrated into small and medium size UAS. Additionally, it summarizes the crash survivability standards required for this technology.

2.1 Flight Data Recorders for Small and Medium-Sized UAS

Flight data storage technology for UAS is constrained by the size, mass, and mission requirements unique to this type of aircraft. Micro Secure Digital (SD) card flash memory units are the preferred technology for the vast majority of available UAS because of their small size, low mass, high-speed performance (UAS sensors store data at ~200Hz), and high-storage capabilities (up to 2TB). A study conducted to forecast the global market share of consumer and commercial drone manufacturers (see Appendix A) indicates that DJI dominates 76% of the UAS global market [8], followed by Intel [9] (4.1%), Yuneec [10] (3.6%), 3D Robotics (acquired by Kittyhawk [11] - 2.6%), Parrot [1] (2.5%) and other brands with less than 1% of the market. Table 1 collects the most representative UAS in the market together with the Maximum Take Off Weight (MTOW) and the type of FDR being used. Note that the other brands with smaller market size were also documented for completeness.

Table 1. Most common UAS in the market and their flight data recording technology.

Manufacturer	Model	Weight [g]	FDR Technology
DJI	Mavic 3	895	Micro SD
DJI	Inspire 2	3,440	Micro SD
DJI	Phantom 4	1,375	Micro SD
Wingtra	One Gen II	3,700	Micro SD
Yuneec	Typhoon H+	1,645	Micro SD
Yuneec	H520 RTK	1,645	Micro SD
Ruko	F11GIM2	584	Micro SD
Ruko	Bwine F7	549	Micro SD
Autel Robotics	EVO II	1,127	Micro SD
Autel Robotics	Pro V3	1,191	Micro SD
Parrot	ANAFI Ai	898	Micro SD
HUBSAN	Ace Pro	600	Micro SD
HUBSAN	Mini	249	Micro SD
HUBSAN	ZINO Pro+	792	Micro SD
Intel	Falcon 8+	1,200	Micro SD

It is interesting to notice that some sUAS models gather all their data into a single memory unit, while other sUAS models store the image and video data separately from the flight data by utilizing two distinct memory units. This solution is ideal from an FDR system point of view, as it avoids over writing or deleting old flight data to store video data. Figure 1 illustrates the FDR location for some of the most representative small and medium-sized UAS.



Figure 1. FDR for common UAS.

In contrast to the conventional crash-protected FDRs found in manned aircraft, the majority of UAS use slot socket readers to attach the data recording devices to the UAS electronic board. It is important to note that these card readers are not designed to provide crash or fire protection to the flight data recorders. Instead, the UAS's internal components and surrounding structures serve as the primary means of safeguarding the flight data recorders in the event of an accident or hazardous condition.

Additional crash-protected lightweight FDRs are available in the market, such as the SferiRec LCR [16] and the FDR01 [17]. SferiRec FDR is compliant with EUROCAE ED-155 and ETSO-2C197 [18] and is able to record video, data, and voice with a total weight of 1kg. The FDR01 only collects and saves the navigation data, with a total weight of 70g. The FDR01's technical brochure does not specify if it is compliant with any of the existing crash-survivability standards. Figure 2 shows these two crash-protected FDRs, and Table 2 summarizes some of their specifications. The weight and the dimensions of these FDRs would not make them suitable for small and medium size UAS. For example, the DJI's volume inside the carcass is approximately 100mmx100mmx80mm, and its total weight is 1,216g. Both of these FDRs would not be suitable

due to their larger size. In addition, the SferiRec LCR 100 weight is too large to be incorporated into a sUAS of these characteristics.



Figure 2. SferiRec LCR 100 (left) and FDR01 (right) FDRs.

Table 2. Specifications of SferiRec LCR 100 and FDR01 FDRs.

	SferiRec LCR 100	FDR01
Weight [g]	1,000	70
Dimensions [mm]	80 (diam.) x 195 (L)	21.5 x 43 x 102
Capabilities	Record and save voice, data, and video	Save data from sensors and control commands
Crash-Survivability Compliance	ED-155	N/A

2.2 Mechanical Standards for Micro SD Cards

In Section 2.1, it was established that a flash memory micro SD with a slot socket reader is the preferred method to store the flight data in a UAS. This section summarizes the crash survivability standards applied to flash memory micro SD cards and compares them to the standards for traditional (TSO-123(c), TSO-C124(b), ED-112), and lightweight (ED-155) FDRs. This allows to identify any potential gaps and assess the suitability of these standards for UAS. Furthermore, it serves as the foundation for generating new standards and helps assess the adequacy of the current requirements towards the goal of a safe operation and high probability of crash survival for lightweight FDRs in UAS.

The most common standards applied to electronic devices such as micro SD cards are:

- JEDEC (JESD22-B104 [19]) and MIL-STD (882-2-2002.5 [20]): Mechanical shock
- EN 60529 [21] or IEC 605:1989 [22]: Ingress Protection (IP)

It should be noted that these standards are not mandatory and are used to demonstrate the product's quality and performance. Other less common mechanical standards are used in the electronics industry (constant acceleration, vibration fatigue, vibration at variable frequency). However, none of these were found in the technical brochure of the most common commercially available micro

SD cards, such as the SanDisk Extreme PRO [23] and ATP Industrial Grade [24]. Table 3 compares the standards for traditional, lightweight FDRs and the standards found in the specifications of the aforementioned commercially available micro SD cards.

Table 3. Crash-survivability standards for traditional, lightweight, and micro SD FDRs.

Test	Traditional FDRs (ED-112)	Lightweight FDRs (ED-155)	Micro SD FDRs
Impact shock	<ul style="list-style-type: none"> • 3,400g for 6.5ms (fixed) • 152ft/s impact with hard surface (deployable) 	<ul style="list-style-type: none"> • 1,000g for 5±1ms (fixed) • 80ft/s impact with hard surface (deployable) 	ATP: 1,500g for 0.5ms SanDisk: 1,500g for 0.5ms
Penetration resistance	<ul style="list-style-type: none"> • 500lb. dropped from 10ft. with a 1/4in. diameter contact point (fixed) • 55lb. dropped from 6in. with a 0.25x0.98in. (max.) sized impactor (deployable) 	N/A	N/A
Static crush	<ul style="list-style-type: none"> • 5,000lb. for 5min (fixed) • 2,000lb. for 5min (deployable) 	• 1,020lb. for 5min (fixed)	N/A
Hydrostatic pressure	• 20,000ft. pressure for 30 days (fixed and deployable)	N/A	ATP: 3.28ft. (1m) for 72 hours SanDisk: 3.28ft. (1m) for 72 hours
High intensity fire	<ul style="list-style-type: none"> • 158 kW/m² for 60min (fixed) • 158 kW/m² for 20min (deployable) 	<ul style="list-style-type: none"> • 158 kW/m² for 15min (fixed) • 158 kW/m² for 5min (deployable) 	N/A
Low intensity fire	<ul style="list-style-type: none"> • 260°C for 10 hours (fixed) • 260°C for 10 hours (deployable) 	N/A	ATP: up to 85°C SanDisk: up to 85°C
Salt water submersion	• Ability to be buoyant (deployable)	• Ability to be buoyant (deployable)	ATP: 3.28ft. for 72 hours SanDisk: 3.28ft for 72 hours
Fluid immersion	• A selection of fluids depending on Certification Authority for 48 hours (fixed and deployable)	N/A	N/A

It is worth mentioning that while it is possible to consider the application of the standards for lightweight FDRs (ED-155) for UAS, these do not include some potential post-crash hazardous

scenarios such as penetration resistance (from secondary impacts), hydrostatic pressure (water landing) and low-intensity fire (proximity to hazardous electronic components such as the battery). Additionally, because of the size and mass of the UAS FDRs, the accelerations expected in a UAS crash scenario are greater than the specified for traditional (ED-112) and lightweight (ED-155) FDRs. A deeper evaluation of these metrics and their application is offered in Chapter 3, where the survivability of commercially available micro SD cards is tested for low-intensity fire, penetration resistance, and static crash. Furthermore, Chapter 4 and Chapter 5 provide the foundation and application of new methodologies that help evaluate and estimate representative post-impact metrics such as impact loads (penetration resistance) and accelerations (shock vibration).

3. ASSESSING MICRO SD CARD CRASH SURVIVABILITY

3.1 Current Ratings and Specifications for Common Micro SD Cards

As previously mentioned, micro SD cards are the predominant flight data storage devices used by sUAS. Due to the range of possible applications for micro SD cards, manufacturers have established test procedures to guarantee the quality and operation of these devices under harsh environments. In fact, some test conditions may be equivalent in nature to those conducted on manned aircraft flight data recorders. A series of physical tests were conducted to understand these cards' capabilities and limitations. The test conditions were selected to resemble those applicable to manned aircraft flight data recorders where possible. Based on the scope of the project, the evaluated test conditions were compression (static crush), low-intensity fire, and penetration resistance. Two different SD card manufacturers were selected. These two cards are equivalent in terms of specifications and are both recommended for use in sUAS. It was observed that the majority of manufacturers producing commercially available SD cards adopt comparable values for these test conditions. Therefore, the selected cards can be considered representative of the market. Table 4 summarizes the physical test that these cards are put through.

Table 4. Physical requirements for SD cards.

Test Condition	Test Criteria by Manufacturer
Crash Impact	500 g's shock
Penetration Resistance	Impact Proof: 5m drop
Static Crush	N/A
Salt Water Submersion	1m salt water up to 72 hrs
Temperature	-25° C to 85°C
X-Ray Proof	Airport X-Ray Immunity
Magnet Proof	Up to 5000 Gauss of static magnetic field

3.2 Physical Tests

To prevent bias by the test operators, different technicians performed mechanical tests for each micro SD card type. Note that technician access to the test data was limited to only one manufacturer. Each of the evaluated test conditions was divided into “preliminary” and

“benchmark” tests. The preliminary tests served to establish the required test parameters for benchmark tests based on the micro SD cards' performance. For the purpose of this investigation, failure was defined as the state at which the SD card was no longer readable or became corrupted, regardless of the physical state of the cards. In turn, benchmark tests were used to define the upper bound of a load range over which the studied cards remained readable. Prior to any of the tests, all micro SD cards were documented and dimensioned. In addition, a combination of text and comma-separated values files were saved on the pristine cards. Out of a minimum of seven files, at least one consisted of a data set equivalent to 10 channels of data recorded at 200Hz for 20 minutes. The health of the cards was assessed prior to the test and after the test. Upon encountering a faulty card, three attempts to read it with three different devices were made. A card was marked as failed if the data on it became unreadable after testing. The following sections summarize the procedures and results for each of the test conditions that the SD cards were subjected to.

3.2.1 Compression

Preliminary static compression tests were conducted, as summarized in the test matrix contained in Table 5. Different levels of compression were evaluated. Based on the results of the preliminary tests, the parameters for the benchmark testing were set individually for each of the card manufacturers. Table 6 summarizes the test matrix for the static crush benchmark tests.

Table 5. Micro SD card compression test matrix – Preliminary tests.

Test #	Test Speed [in/min]	Stopping Criteria	
		Manufacturer 1	Manufacturer 2
1-2	0.005	10 % Avg. Thickness Compression	10 % Avg. Thickness Compression
3-4	0.005	15 % Avg. Thickness Compression	15 % Avg. Thickness Compression
5-6	0.005	20 % Avg. Thickness Compression	20 % Avg. Thickness Compression
7-8	0.005	22.5 % Avg. Thickness Compression	22.5 % Avg. Thickness Compression
9-10	0.005	25 % Avg. Thickness Compression	25 % Avg. Thickness Compression
11-12	0.005	20 % Avg. Thickness Compression	22.5 % Avg. Thickness Compression
13-14	0.005	20 % Avg. Thickness Compression	22.5 % Avg. Thickness Compression
15-16	0.005	20 % Avg. Thickness Compression	22.5 % Avg. Thickness Compression

Table 6. Micro SD card compression test matrix – Benchmark tests.

Test #	Test Speed [in/min]	Stopping Criteria	
		Manufacturer 1	Manufacturer 2
1	0.005	20 % Avg. Thickness Compression or 1,800lbf	22 % Avg. Thickness Compression or 2,400lbf
2	0.005	20 % Avg. Thickness Compression or 1,800lbf	22 % Avg. Thickness Compression or 2,400lbf
3	0.005	20 % Avg. Thickness Compression or 1,800lbf	22 % Avg. Thickness Compression or 2,400lbf
4	0.005	20 % Avg. Thickness Compression or 1,800lbf	22 % Avg. Thickness Compression or 2,400lbf
5	0.005	20 % Avg. Thickness Compression or 1,800lbf	22 % Avg. Thickness Compression or 2,400lbf
6	0.005	20 % Avg. Thickness Compression or 1,800lbf	22 % Avg. Thickness Compression or 2,400lbf
7	0.005	20 % Avg. Thickness Compression or 1,800lbf	22 % Avg. Thickness Compression or 2,400lbf
8	0.005	20 % Avg. Thickness Compression or 1,800lbf	22 % Avg. Thickness Compression or 2,400lbf
9	0.005	20 % Avg. Thickness Compression or 1,800lbf	22 % Avg. Thickness Compression or 2,400lbf
10	0.005	20 % Avg. Thickness Compression or 1,800lbf	22 % Avg. Thickness Compression or 2,400lbf

All tests were conducted at the Advanced Virtual Engineering and Testing Laboratories of the National Institute for Aviation Research (NIAR). The tests were conducted at room temperature and ambient relative humidity. A 35kip test frame was used for testing. The frame was equipped with 22kip strain gauge load cells. The system is able to operate as a standard universal test machine. This configuration was used for testing. A pair of 2” cylindrical platens were used to compress the SD cards. The setup is illustrated in Figure 3.

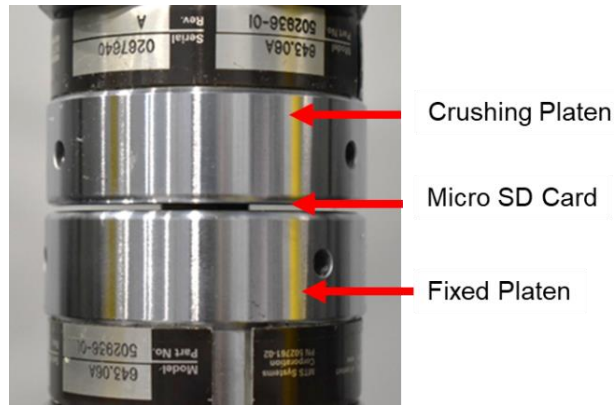


Figure 3. Static crush test setup.

Table 7 summarizes the test results for the preliminary tests conducted on the manufacturer 1 micro SD card. Sixteen tests were conducted; five different compression levels were evaluated. Failure was obtained for 20% and 25% of thickness nominal compression levels. Based on the results, the following parameters were used as stopping criteria for benchmark testing: 18.5% of thickness or 3,060 lbf. These values represent the lowest compression percentage and lowest load at which failure occurred.

Table 7. Micro SD card compression tests results – Preliminary tests manufacturer 1.

Test #	Nominal Compression [%]	Max. Load [lbf]	Card Status
1	10	246.3	Readable
2	10	405.1	Readable
3	15	2,068.7	Readable
4	15	71.0	Readable
5	20	3,584.3	Readable
6	20	3,738.9	Failed
7	22.5	4,162.7	Readable
8	22.5	4,459.9	Readable
9	25	3,911.2	Failed
10	25	4,748.1	Failed
11	20	3,577.8	Readable
12	20	3,732.6	Failed
13	20	4,267.6	Readable
14	20	3,061.7	Failed
15	20	4,673.4	Readable
16	20	2,825.0	Readable

Table 8 summarizes the preliminary test results for the SD card made by manufacturer 2. These cards were also tested at five different compression levels. For benchmark testing, the following criterion was established: 22.4% nominal compression or 3,740lbf.

Table 8. Micro SD card compression tests results – Preliminary tests manufacturer 2.

Test #	Nominal Compression [%]	Max. Load [lbf]	Card Status
1	10.0	1,245.7	Readable
2	10.0	947.7	Readable
3	15.0	2,104.7	Readable
4	15.0	2,275.8	Readable
5	20.0	3,134.6	Readable
6	20.0	3,415.9	Readable
7	22.5	3,915.2	Failed
8	22.5	4,249.3	Readable
9	25.0	4,452.6	Failed
10	25.0	4,946.1	Failed
11	22.5	4,449.3	Readable
12	22.5	3,836.6	Failed
13	22.5	3,740.1	Failed
14	22.5	Null	Null
15	22.5	3,781.3	Readable
16	22.5	3,948.4	Readable

For benchmark testing, ten tests were conducted per card manufacturer. The results are summarized in Table 9. It is worth noting that none of the tested cards sustained visible damage. In other words, the physical appearance remained intact after the test, regardless of the compression level to which the cards were exposed and the status of the card after testing.

Table 9. Micro SD card compression tests results – Benchmark tests.

Manufacturer ID	Benchmark Tests	Failed Samples	Number of Failed Samples/Stopping Criteria Met	
			Displacement	Load
1	10	1	0	1
2	10	1	0	1

As can be seen, the benchmark testing resulted in a single failure for each micro SD card manufacturer. NIAR found that the minimum load under static crush at which a micro SD card stopped reading was 3,061 lbs. This does not entail that any card, even within the same

manufacturer brand or specific model would be able to survive such load but instead serves as qualitative reference for the purposes of the current study.

3.2.2 Low-Intensity Fire

As previously mentioned, a low-intensity fire was to be evaluated. The two manufacturers of the SD cards used for this program already provide a range of temperatures for the operation of the devices. The temperature ranges from -25 to 85°C. In an effort to explore the limitations of the SD cards, NIAR evaluated temperatures above 85°C. Figure 4 illustrates the test profile.

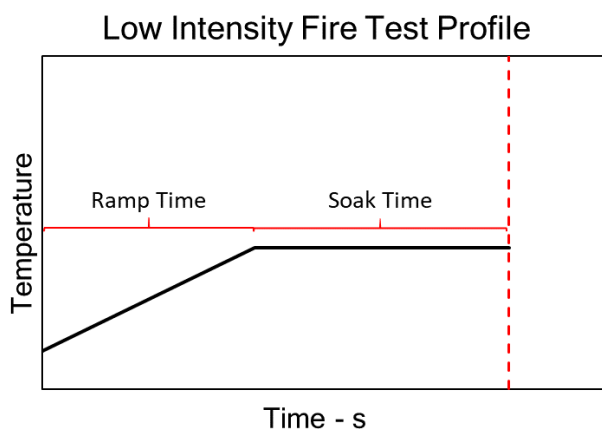


Figure 4. Low-intensity fire test profile.

The ramp time was defined as the time elapsed from the placement of the test sample inside the oven to the point where the sample reached the test temperature. The soak time was defined as the amount of time the sample was held at the test temperature.

The tests consisted in inserting the cards into an air convection oven. A thermocouple was adhered directly to the card to track its temperature. The cards were then ramped and soaked at the corresponding test temperature. Figure 5 illustrates the test setup. Upon completion of the test, the status of the cards was assessed and recorded.



Figure 5. Low-intensity fire test setup.

Table 10 summarizes the test matrix corresponding to the preliminary tests conducted. Equal matrices were used for both SD card manufacturers.

Table 10. Micro SD card low-intensity fire tests matrix – Preliminary tests.

Test #	Temperature [°C]	Soak Time [s]	Status
1-2	85	180	Readable
3-4	95	180	Readable
5-6	100	180	Readable
7-8	110	180	Readable
9-10	125	180	Readable
11-12	150	180	Readable
13-14	175	180	Readable
15-16	200	180	Readable

The tests, as defined above, did not result in failure for either of the card manufacturers. Therefore, the conditions presented in Table 11 were evaluated.

Table 11. Micro SD card low-intensity fire tests results – Benchmark tests.

Test #	Temperature [°C]	Soak Time [s]	Status
1-4	150	900	Readable
5-8	150	1800	Readable
9-10	200	600	Readable

As seen above, NIAR was unable to obtain a failure of a card in any of the conducted low-intensity fire tests. If the limitations of the SD cards under low-intensity fire conditions are to be further explored, additional research is required. It is recommended to evaluate higher temperatures and longer soak times.

3.2.3 Penetration Resistance

The penetration resistance tests were similar to the static crush tests. The main difference lies in the fact that the SD cards were loaded using a semi-spherical indenter as opposed to a flat platen. Table 12 presents the test matrix for the preliminary penetration resistance tests. Different levels of compression were evaluated. Based on the preliminary tests' results, the benchmark testing parameters were individually set for each of the card manufacturers. Table 13 summarizes the test matrix for the penetration resistance benchmark tests.

Table 12. Micro SD card penetration resistance test matrix – Preliminary tests.

Test #	Test Speed [in/min]	Stopping Criteria	
		Manufacturer 1	Manufacturer 2
1-2	0.005	25 lbf	25 lbf
3-4	0.005	30 lbf	30 lbf
5-6	0.005	50 lbf	30 lbf
7-8	0.005	75 lbf	50 lbf
9-10	0.005	100 lbf	40 lbf
11-12	0.005	125 lbf	40 lbf
13-14	0.005	150 lbf	35 lbf
15-16	0.005	175 lbf	35 lbf

Table 13. Micro SD card penetration resistance test matrix – Benchmark tests.

Test #	Test Speed [in/min]	Stopping Criteria	
		Manufacturer 1	Manufacturer 2
1	0.005	75 lbf	35 lbf
2	0.005	75 lbf	35 lbf
3	0.005	75 lbf	35 lbf
4	0.005	75 lbf	35 lbf
5	0.005	75 lbf	35 lbf
6	0.005	75 lbf	35 lbf
7	0.005	75 lbf	35 lbf
8	0.005	75 lbf	35 lbf
9	0.005	75 lbf	35 lbf
10	0.005	75 lbf	35 lbf

Similar to the compression tests, the penetration resistance tests were conducted at room temperature and ambient relative humidity. A 35kip test frame was used for testing. The frame was equipped with 22kip strain gauge load cells. The system is able to operate as a standard universal test machine. This configuration was used for testing. A 2” cylindrical platen was used to support the SD cards, and a 3/8” semi-spherical indenter was used to load them. Figure 6 illustrates the test setup.

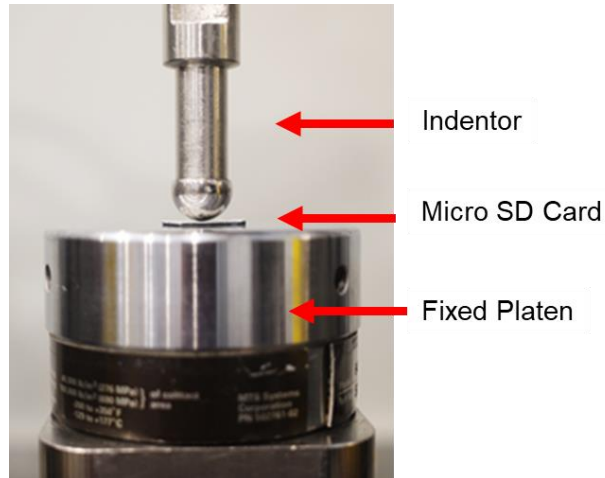


Figure 6. Penetration resistance test setup.

Table 14 summarizes the test results for the preliminary tests conducted on the manufacturer 1 micro SD card. Sixteen tests were conducted; eight different compression levels were evaluated. Failure was obtained for 75, 100, 125, 150, and 175lbf load levels. Based on the results, 75lbf was used as the test-stopping criteria for benchmark testing. This value represents the lowest load level at which failure was recorded.

Table 14. Micro SD card penetration resistance tests results – Preliminary tests manufacturer 1.

Test #	Max. Load [lbf]	Card Status
1	25	Readable
2	25	Readable
3	30	Readable
4	30	Readable
5	50	Readable
6	50	Readable
7	75	Failed
8	75	Readable
9	100	Failed
10	100	Readable
11	125	Failed
12	125	Readable
13	150	Readable
14	150	Failed
15	175	Readable
16	175	Failed

Table 15 summarizes the preliminary test results for the SD card made by manufacturer 2. These cards were tested to five different compression levels. As shown in Table 13 for benchmark testing conditions, 35lbf was used as the test-stopping criteria.

Table 15. Micro SD card penetration resistance tests results – Preliminary tests manufacturer 2.

Test #	Max. Load [lbf]	Card Status
1	25	Readable
2	25	Readable
3	30	Readable
4	30	Readable
5	50	Failed
6	50	Readable
7	40	Failed
8	40	Failed
9	40	Readable
10	40	Failed
11	30	Readable
12	30	Readable
13	35	Failed
14	35	Failed
15	35	Readable
16	35	Readable

For benchmark testing, ten tests were conducted per card manufacturer. Table 16 summarizes the results of these tests. Similar to the static crush tests, none of the tested cards exhibit visible damage.

Table 16. Micro SD card penetration resistance tests results – Benchmark tests.

Manufacturer ID	Benchmark Tests	Failed Samples
1	10	4
2	10	2

As seen above, the benchmark testing resulted in four failures for manufacturer 1 and two failures for manufacturer 2. The minimum penetration load that resulted in failure was 35 lbs. Similar to

the static crush data, this number provides a qualitative baseline to use as a reference in the current research effort.

3.2.4 Physical Tests Key Findings Summary

The two studied SD cards remained readable after static crush testing in the load range between 70 and 2,785 lbs. Failure was obtained at a load of 3,061 lbs. The evaluated low intensity fire conditions did not lead to SD card failure. The maximum temperature at which the cards were tested was 200°C; a broader temperature range along with soak times could be considered in future research. The analyzed SD cards were readable after the application of a penetrating load with a 3/8” semi-spherical indenter up to 30 lbs. The first failure was observed at 35lbs. The correlation between these findings and the results of the numerical simulations are addressed in the subsequent sections of this report.

4. NUMERICAL METHODS FOR SHOCK SURVIVABILITY OF ELECTRONIC DEVICES

This chapter offers a comprehensive review of the existing numerical methods for analyzing impact shock conditions in electronic devices. Additionally, two of the analyzed numerical models were replicated in order to calibrate the methodologies used in Sections 4.3 and 5.4. This section also presents the experimental and numerical results of a low-velocity impact test performed on an electronic board of a representative DJI Phantom III.

4.1 Literature Review

At the time of writing this report, no work was found considering the impact shock properties of flash memory devices. However, it was possible to learn the numerical methodologies used in the open literature of analyses performed using electronic chips attached to electronic boards, similar to the slot socket architectures used for data recording in UAS (see Section 2.1). By analyzing the state of the art in the analysis of impact reliability of electronic devices, similar numerical techniques can be utilized to evaluate the shock performance of FDRs in UAS.

Most shock survivability tests and analyses considering electronic boards are based on the impact conditions specified in JESD22-B104C (1,500g for 0.5ms). The crash-survivability is often evaluated by subjecting the structure to an equivalent shock pulse for a post-impact evaluation of the chip’s connections with the board [25][26][27][28]. Due to the complexity and small size of the chips’ internal structure, these are often simplified using the smeared properties [29]. This method simplifies each one of the internal components by using homogenized properties and a representative geometry. Figure 7 compares a commercially available Chip Scale Package (CSP) to the simplified Finite Element Model (FEM) of a similar component found in some open literature.

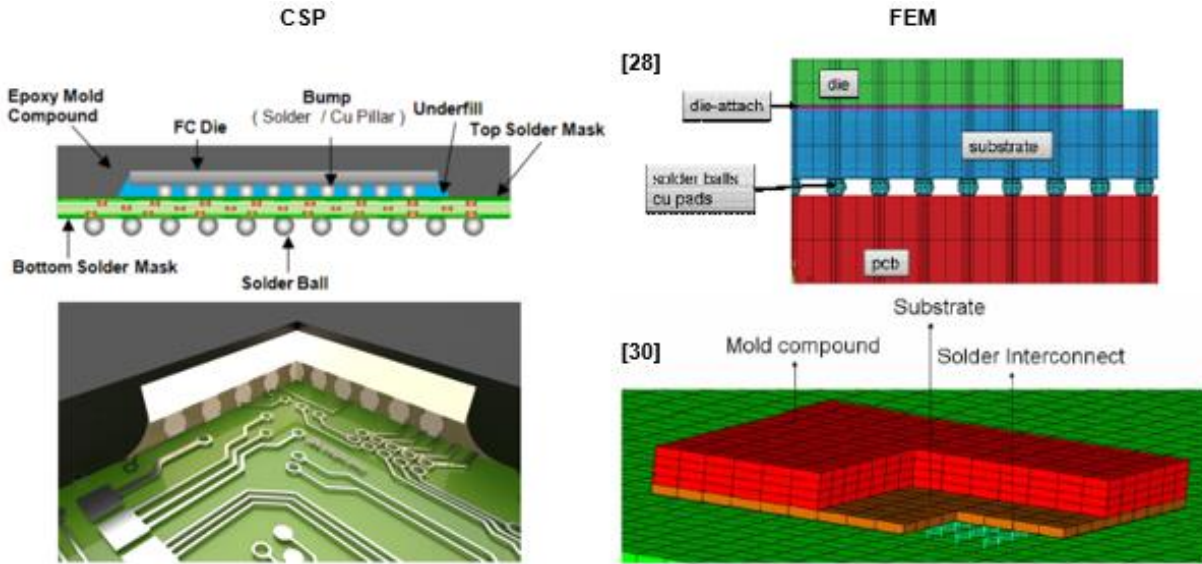


Figure 7. Commercially available CSP [31] and simplification of a similar chip using the FEM [28][30].

Some of the limitations of these types of tests and modeling techniques are associated with obtaining a good repeatability of the impact event. The shock vibrations induced into these structures have a high magnitude and a short duration due to the components' low mass and high stiffness, as well as the surrounding structure. A 1.5m vertical drop test of a phone device can produce accelerations at the board level as high as 10,000g [27]. Secondary impacts can increase the acceleration peaks up to 30,000g. Furthermore, the contact interaction and attachments between the test article and the fixture introduce additional complexity to the numerical simulations.

Yan Tee, T., et al. [31] developed the input-G method, where the test fixture as well as its connections to the test article, are removed from the analysis and replaced by the shock acceleration profile produced by the impact shock. This method eliminates the variability and challenges implicit in the fixture interaction with the test article. The shock acceleration profile is added to the model by means of a prescribed acceleration. It becomes possible to define the actual shock profile collected from the physical test or the idealized shock profile described in the standards. The input-G method is a powerful alternative when the area of interest is far from the simplified connection region.

Another critical aspect to consider when examining the shock response of electronic devices is the structure's modal response. Spectral plots offer valuable information about the main modes of deformation and their frequency characteristics [27]. By analyzing the structure's modal response for certain constrained configurations and loading conditions, it is possible to predict what modes of deformation will have more impact on the transient response.

Overall, successful analysis of the shock impact events in electronic devices depends on the appropriate modeling of the components, impact conditions, and the understanding of the structure's transient response.

Lastly, in an attempt to understand what type of data acquisition systems are used in these specific tests and how to properly define the data outputting in the analyses performed in this work, the type of data acquisition systems and sampling rates used in the reviewed experimental work were documented. Table 17 contains all the information gathered during the review of the experimental techniques in the field of shock impact of electronics devices.

Table 17. Main aspects of the data acquisition procedures in the reviewed experimental work.

Ref.	Test / Device	Data Acquired	Equipment	Sampling Rate
[25]	Board assembly drop test	Strain and displacement	High-speed video and strain gages	40,000 fps for video and 5 MHz for strains and accelerations.
[26]	Board assembly and phone drop test	Acceleration and strain	Accelerometer (0.2g) and strain gages	N/A
[27]	Board assembly drop test	Strain	Strain gage	100,000 Hz
[29]	Board assembly drop test	Strain, continuity, and acceleration	High-speed camera and strain gages	40,000 fps for video and 1 MHz for strains and accelerations.
[30]	Board assembly drop test	Strain	DIC, high-speed video cameras, and strain gages	275,000 fps
[33]	Board assembly drop test	Impact force, acceleration and strain	Load cell, strain gages, and accelerometer	N/A
[34]	Drop test (PBA)	Displacement	DIC	10,000 fps
[35]	Phone drop test	Velocity and acceleration	DIC	8,000 fps
[36]	Board assembly and housing drop test	Velocity, impact pulse, and strain (at the bar)	Hopkinson bar, strain gages, high-speed camera, and laser sensors	N/A
[37]	Board assembly drop test	Strain	Strain gauge and accelerometer	N/A

4.2 Preliminary Analyses

This section presents the model generation and validation of two different board assembly drop tests. Zhu, L. et al. [26] tested and validated different board assembly specimens using the impact shock conditions specified in JEDEC JESD22-B104C-B (1500g, 0.5ms). For this, the specimens were placed in a drop tower, dropped from a certain height (depending on the specified shock pulse limit), and impacted with a base-plate. A break was used after the impact to avoid a secondary impact and ensure good test repeatability. The work performed in [26] was focused on developing robust models able to capture the transient response of the CSPs as well as the failure mechanisms of the chip's welded connections. However, capturing the failure mechanisms of the soldered balls requires a very small element size ($<0.1\text{mm}$), which significantly increases the computational cost. The goal of these preliminary analyses was to define a methodology for modeling the board assembly structures that could later be applied in the full-scale models defined in this work. Some of these full-scale models consider entire aircraft structures ($>1,000,000$ elements), and hence it is not possible to model small components such as electronic chips with a high level of detail.

The preliminary analyses shown in this section only consider the drop test of the specimen with a single CSP at the center. The specimen's measurements were reverse-engineered, and the geometry was discretized using 4,894 shells (2-dimensional) elements for the Printed Circuit Board (PCB) and 108 solids (3-dimensional) elements for the CSP. The CSP was discretized using three elements in the thickness direction, which leads to a minimum element size of 0.47mm . Table 18 specifies the element criteria used during the discretization process. Figure 8 presents the mesh and main dimensions of the board assembly.

Table 18. Mesh quality criteria.

Quality Parameter	Allowable	
	Shell Elements	Solid Elements
Min. Side Length	1.5 mm	0.47 mm
Max. Aspect Ratio	5	
Min. Quad Angle	45°	-
Max. Quad Angle	140°	-
Min. Tria Angle	30°	-
Max. Tria Angle	120°	-
Max. Warp Angle	5°	15°
Min. Jacobian	0.7	0.5

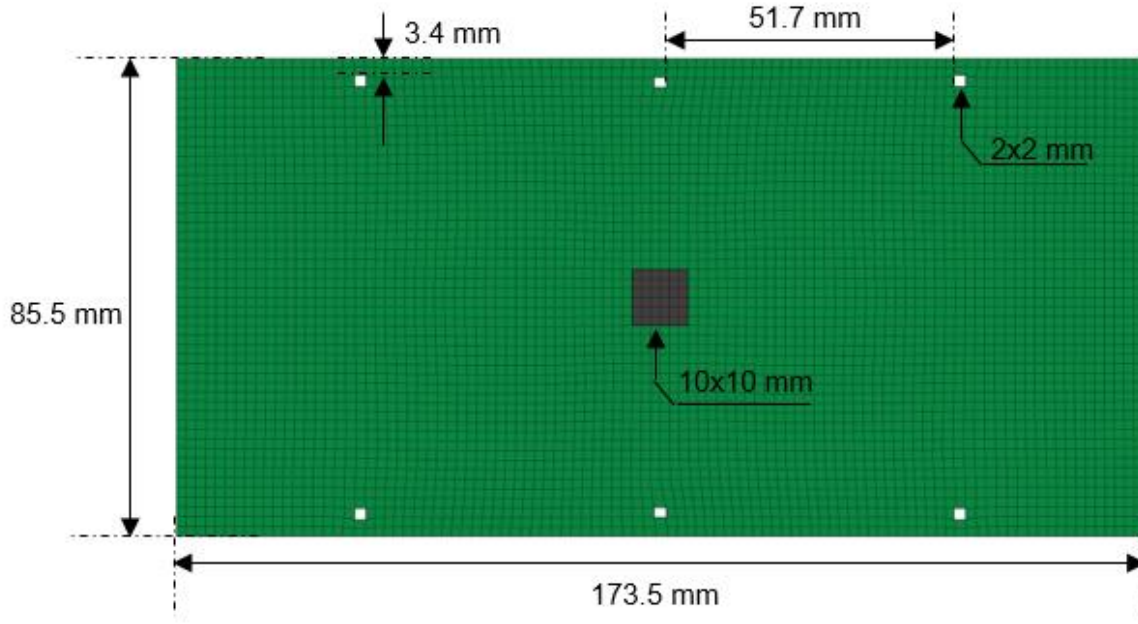


Figure 8. Discretization of the board assembly with a single CSP at the center.

The material properties were not reported in [26]. However, Wang, Y. et al. [38] proved that an orthotropic elastic material model is a fair approximation for glass-fiber reinforced PCBs. Table 19 summarizes the material properties used for the PCB, which are similar to the ones reported in [38].

Table 19. PCB material properties used in the FEM.

Density (kg/m^3)	Young's Modulus (GPa)	Shear Modulus (GPa)	Poisson's Ratio
1900	$E_x = 22$	$G_{xy} = 3.5$	$V_{xy} = 0.28$
	$E_y = 9.8$	$G_{yz} = 3.5$	$V_{yz} = 0.28$
	$E_z = 22$	$G_{xz} = 2.5$	$V_{xz} = 0.11$

The CSP was simplified as a continuum solid body with elastic-smeared properties. Table 20 presents the properties used for each individual component extracted from [29]. Equations (1) through (3) [29] were used to compute these properties. Additionally, the dimensions of each internal component were approximated by observing typical CSP architectures reported in [39] and [40]. Figure 9 compares the cross-section of the assumed detailed CSP's structure to the cross-section of the simplified FEM. Note that the solder balls were not considered for the computation of the smeared Young's modulus and Poisson's ratio. Nevertheless, the density equation accounts for the mass of these components.

Table 20. Material properties of the CSP components.

Component	h_k [mm]	E_k [GPa]	ρ_k [Ton/mm ³]	ν_k	V_k [mm ³]
Solder ball (172)	-	32	8.4e-9	0.35	3.44
BT Substrate	0.1	17.4	1.8e-9	0.28	10
Die Attach	0.1	2.76	7.8e-9	0.35	3.6
Die	0.35	162	2.33e-9	0.28	12.6
Mold Compound	0.55	23.5	1.65e-9	0.25	83.8

$$\nu_c = \frac{\sum_{k=1}^5 \nu_k h_k}{\sum_{k=1}^5 h_k} = 0.271 \quad (1)$$

$$\rho_c = \frac{\sum_{k=1}^5 \rho_k V_k}{\sum_{k=1}^5 V_k} = 2.1 \times 10^{-9} \text{ Ton/mm}^3 \quad (2)$$

$$E_c = \frac{12(1-\nu_c)}{h_c^3} \frac{\sum_{k=1}^4 E_k h_k^3}{\sum_{k=1}^4 12(1-\nu_k)} = 8.137 \text{ GPa} \quad (3)$$

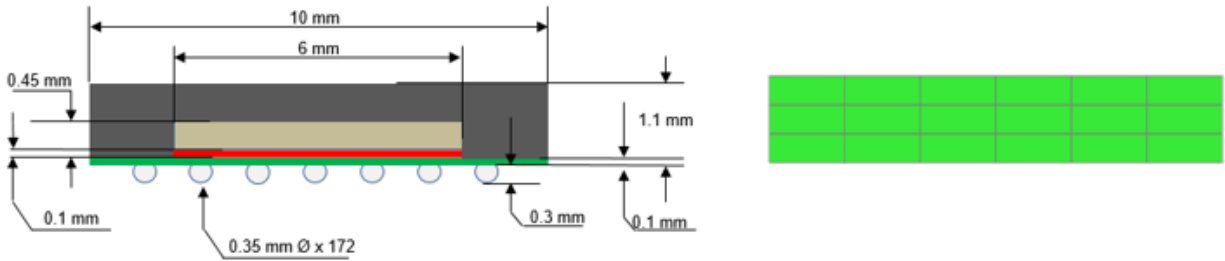


Figure 9. Cross-sections of the detailed CSP architecture (left) and simplified FEM (right).

Two different tests were replicated using the LS-Dyna explicit finite element code.

- Drop test of board assembly using JEDEC JESD22-B104C-B (1500g, 0.5ms) test conditions with a 6-support fixture
- Drop test of board assembly using JEDEC JESD22-B104C-B (1500g, 0.5ms) test conditions with a 4-support fixture.

6-SUPPORT ASSEMBLY DROP TEST

The boundary conditions were applied using the input-G method. A prescribed acceleration with a 1,500g peak and 0.5ms half-sine shape was applied to the simplified rigid fixture in the Z-direction. Equation **Error! Reference source not found.**) describes the acceleration pulse applied to the model. Figure 10 presents the isometric, top, and side view of the final FEM with the simplified 6-support fixture. The fixture was discretized using 3D elements, and it was modeled using a rigid type material.

$$Az(t) = 1500\sin\left(\frac{2\pi}{0.001}t\right) \quad (4)$$

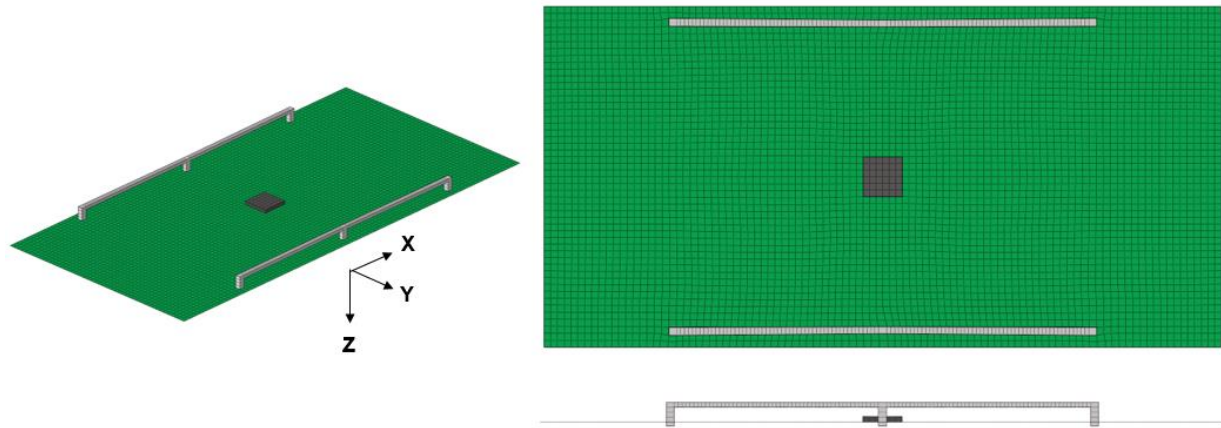


Figure 10. Finite element model of the 6-support board level assembly drop test.

Prior to computing the solution of the analysis, the damping factor for the structure was estimated. The open literature recommends using Rayleigh damping with values of $\alpha=0.7$ and $\beta=0.4$ for this type of analysis [26]. However, this type of damping is only available in implicit solvers. To capture the representative damping of the structure, the damping coefficient was estimated by applying Equations

(5) and (6) - logarithmic decrement - to the experimental data reported in [26] for the 6-support test. In these expressions, a is the acceleration, n is the period number, T is the period duration, δ

is the logarithmic decrement, and ζ the damping coefficient. Figure 11 shows the acceleration data used to compute this value.

$$\delta = \frac{1}{n} \ln\left(\frac{a(t)}{a(t+nT)}\right) = \frac{1}{7} \ln\left(\frac{4000}{775}\right) = 0.235 \quad (5)$$

$$\zeta = \frac{1}{\sqrt{1 + \left(\frac{2\pi}{\delta}\right)^2}} = 0.037 \quad (6)$$

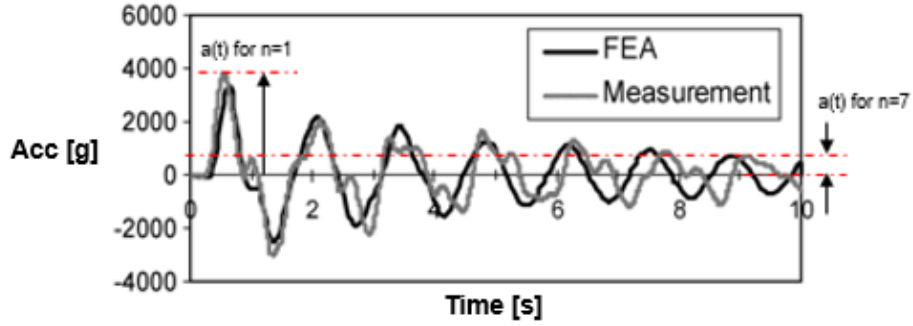


Figure 11. 6-support drop acceleration test data for damping coefficient calibration (plot from [26]).

The drop test transient response of board assembly specimens is dominated by bending and twisting modes [42]. A modal analysis was performed to extract the frequencies of interest, which were later used in the drop-test analysis to apply the damping ratio. Figure 12 illustrates the 10 first modes of the structure constrained by the 6-support fixture. The displacement contour shows the shape of the vibration for each frequency. The magnitude of the displacement is not meaningful since there are no loads applied in the analysis. Note that the rigid body modes are not shown. A damping factor of 3.7% of the critical damping was applied to the 277.44-970Hz frequency interval.

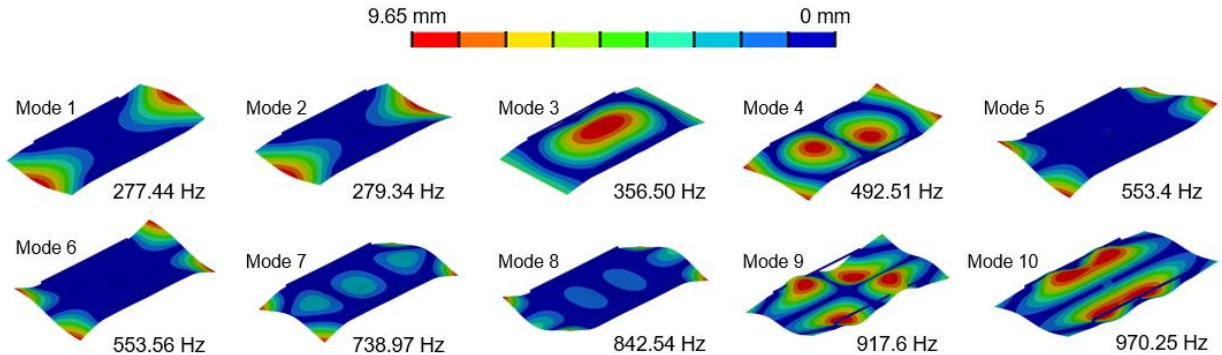


Figure 12. Ten first modes for the 6-support drop test.

Figure 13 compares the experimental and numerical accelerations reported in [26] to the acceleration obtained from the analysis. It can be observed that although the frequency of the second and subsequent oscillations is slightly lower than for the reported curves, a satisfactory correlation of the magnitude and shape for the most significant oscillation was achieved. This proves the input-G method combined with the simplification of the CSP using smeared properties to be a simple but powerful method to model board assemblies and predict acceleration values for this type of loading condition.

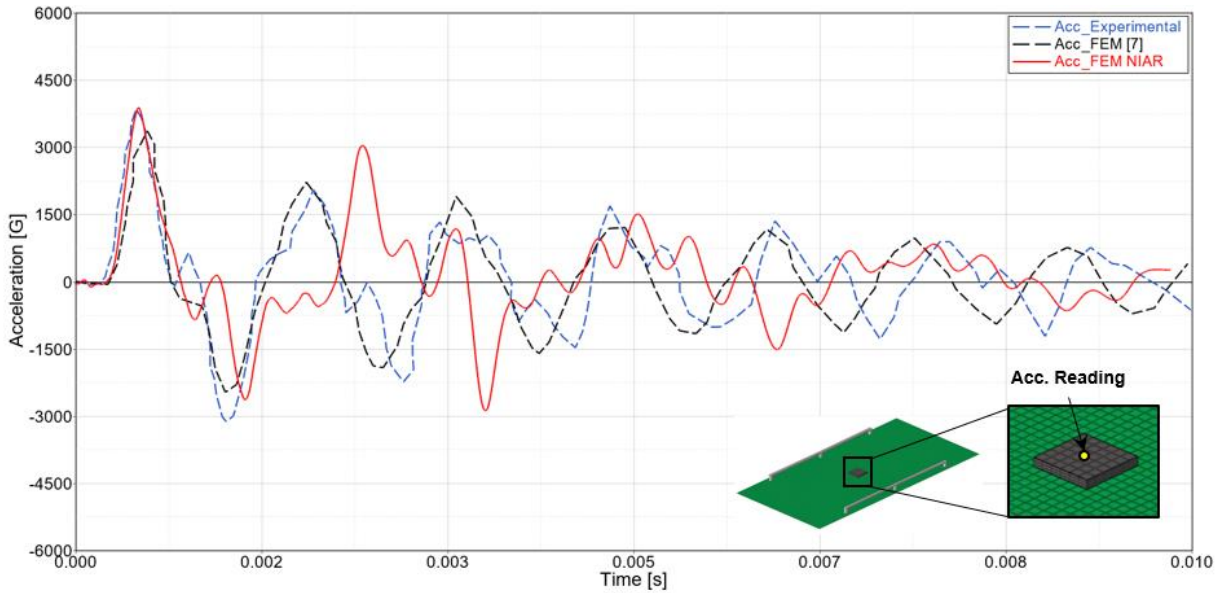


Figure 13. Acceleration comparison for the 6-support drop test validation exercise.

4-SUPPORT ASSEMBLY DROP TEST

The 4-support model was built by removing the center support arms from the simplified fixture of the 6-support FEM. Figure 14 presents the isometric, top, and side views of the 4-support drop FEM.

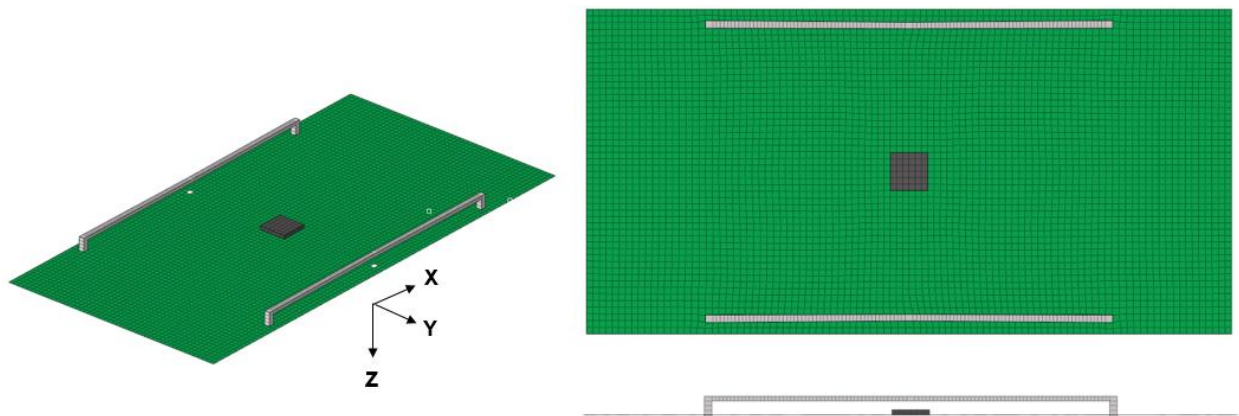


Figure 14. Finite element model of the 4-support board level assembly drop test.

The boundary conditions were identical to those for the 6-support FEM. A prescribed acceleration was applied in the Z-direction using Equation **Error! Reference source not found.**). Using the same method described for the 6-support drop analysis, a damping ratio of 4.5% the critical damping was applied to the 205-840Hz frequency interval. For this case, the model validation was performed by comparing the experimental data reported in [26] to the strain in the X-direction at the corner of the CSP. Note that the strain reading was performed at the lower face of the PCB. Figure 15 presents the strain comparison to the experimental data. Again, a successful correlation to the experimental data was achieved using the input-G method. Additionally, this proves that simplifying the CSP using the smeared properties does not significantly affect the PCB's response.

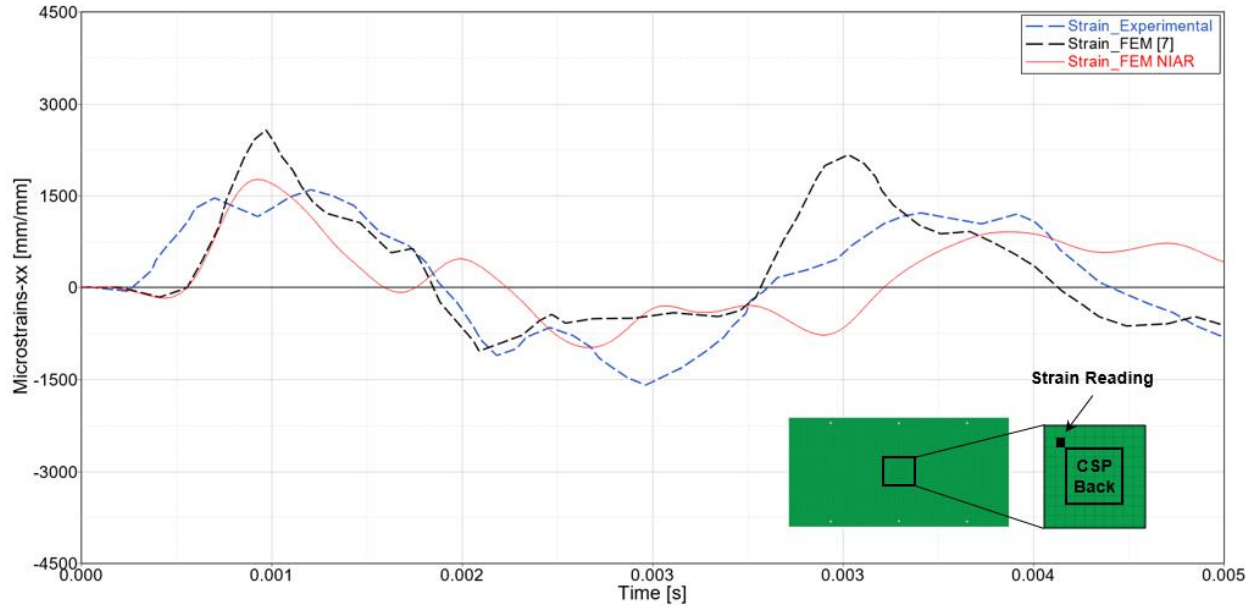


Figure 15. Strain ϵ_{xx} comparison for the 4-support drop test validation exercise.

4.3 Low-Velocity Impact of a sUAS Electronic Board

This section presents the validation of a representative DJI Phantom III board FEM performed by replicating a Low-Velocity Impact (LVI) test. The test was designed to apply the methodologies learned from the preliminary analyses and the literature review. Furthermore, this validation exercise included contact interactions in the analysis, which were not present in the preliminary analyses. Hence, it was possible to calibrate other components of the simulation, such as the contact parameters, output frequencies, and post-processing filters. Figure 16 shows the top and bottom view of the board assembly specimen.

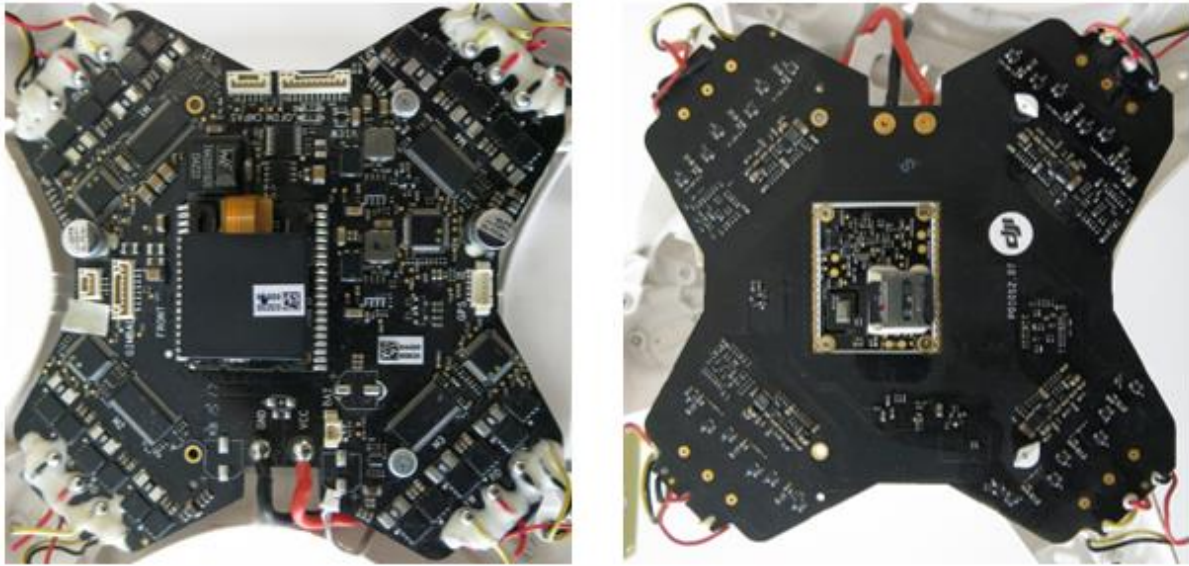


Figure 16. Representative DJI Phantom III board assembly specimen.

The board was disassembled from the UAS, and the motor and battery wires were removed from it to avoid noise in the acceleration reading. The specimen was inspected and reverse-engineered to be accurately modeled. Some of the electronics, such as resistors, transistors, or connectors, were not captured in the FEM due to their small size. However, the mass of these components was accounted for by means of non-structural mass elements. Note that the battery cables were modeled to include them in the full-scale analyses presented in Chapter 5, but these were removed for the component level validation, replicating the test specimen. Figure 17 illustrates the main components captured in the FEM. Table 21 gathers the geometry and mesh details of the reverse-engineered electronic components.

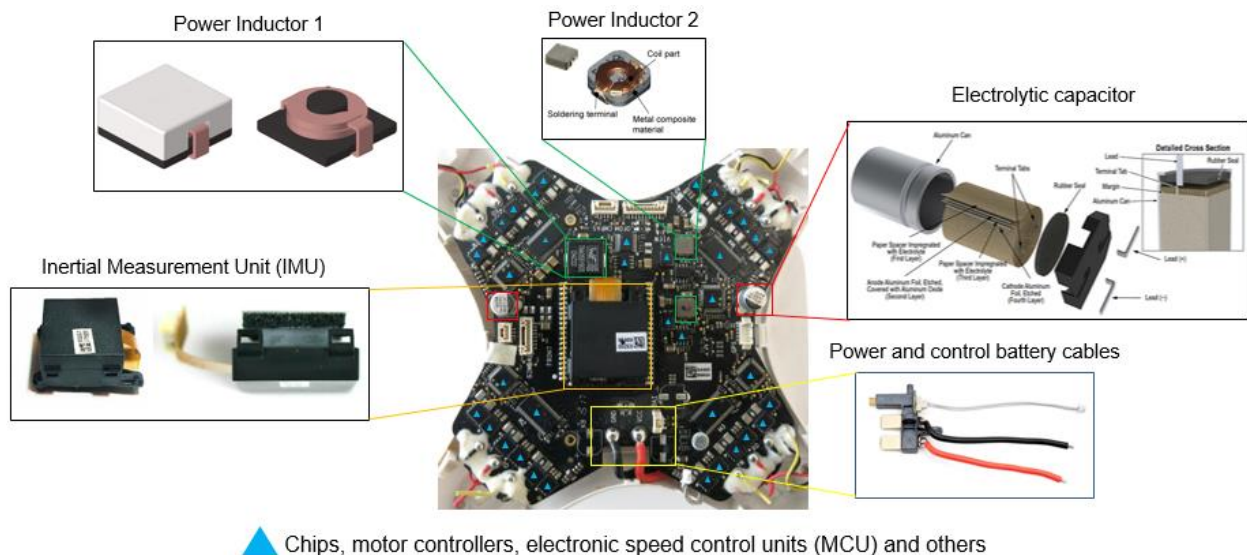
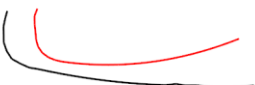


Figure 17. Electronic components captured in the FEM.

Table 21. Geometry and mesh details of the modeled electronic components.

Component	Mesh	Details
<p>Inertial Measurement Unit (IMU)</p> 		<ul style="list-style-type: none"> • Foam captured in the FEM. • 3D mesh with 2,198 solid elements.
<p>Power Inductor 1</p> 		<ul style="list-style-type: none"> • Housing meshed with 3D elements and coil meshed with shell elements. • 544 solid elements and 80 shell elements.
<p>Power Inductor 2</p> 		<ul style="list-style-type: none"> • Simplified as a single continuum body meshed with 75 solid elements due to the small size of the internal components.
<p>Electrolytic capacitor</p> 		<ul style="list-style-type: none"> • Housing and internal layers are simplified as a continuum. • Base-plate meshed with 3D elements with shared-nodes. • 3D mesh with 310 solid elements.
<p>Power and control battery cables</p> 		<ul style="list-style-type: none"> • Power cables are modeled as discrete beams (large length/diameter ratio). • Battery control cable not included.
<p>Micro SD card and socket</p> 		<ul style="list-style-type: none"> • SD card and housing meshed with 3D elements. Upper shell meshed with 2D elements. • Micro SD (Virtual Sensor) geometry is simplified with a rectangular shape.

The mesh quality criteria parameters were the same as presented in Table 18 except for the minimum element size, which was lowered to 0.3mm for 3D elements and 0.7mm for 2D elements to represent the small chips accurately. The final mesh has 56 1D elements, 7,654 2D elements, and 7,510 3D elements. Figure 18 compares the specimen's top, bottom, and isometric views to

the final mesh. The representative materials of each one of the components were identified and extracted from NIAR's material database. Figure 19 presents the representative materials of the board FEM components. Note that the same smeared properties defined for the CSPs in Section 4.2 were assumed for the chips.

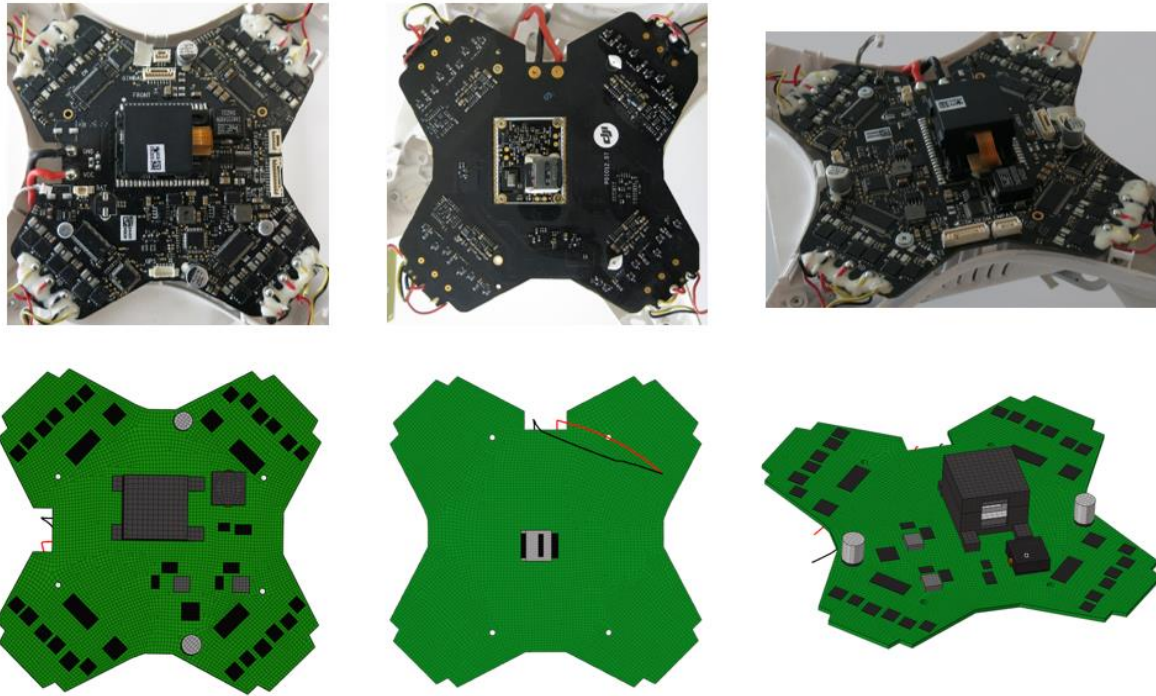


Figure 18. Top, bottom, and isometric view comparisons of the board test specimen and FEM mesh.

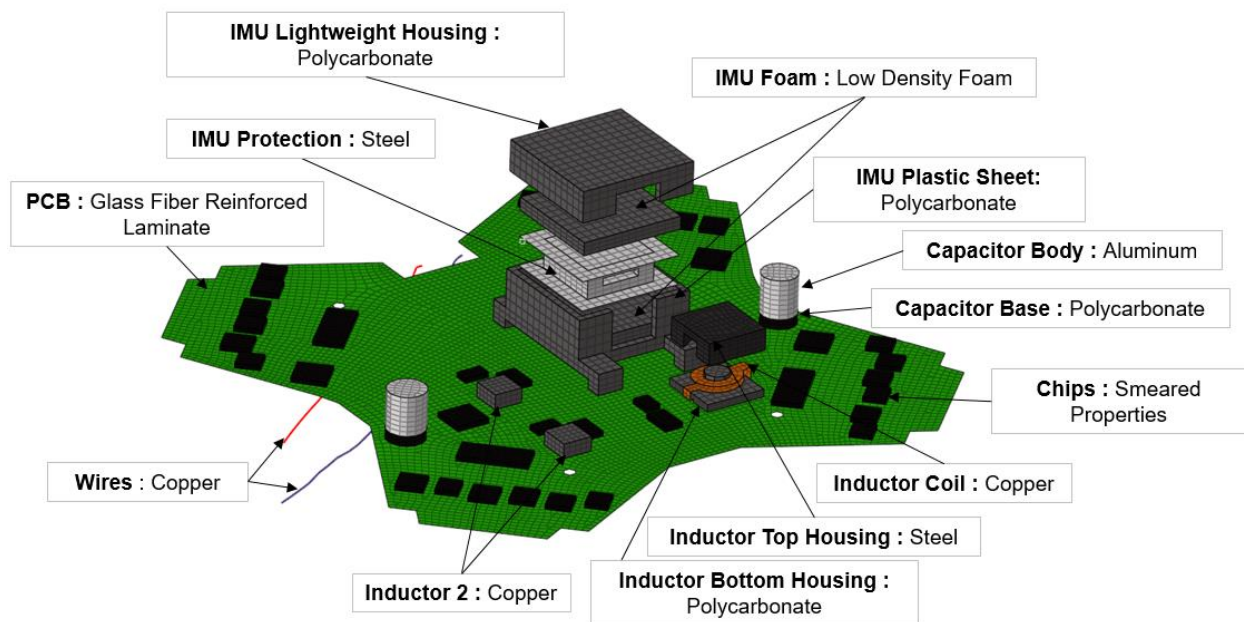


Figure 19. Board assembly FEM - Materials.

The test was carried out by impacting the board assembly with a 5/8in. semi-spherical tup. Table 22 presents the test conditions. To achieve this, a fixture was designed and manufactured to attach the board assembly at the four available fastener holes while keeping it centered with the impactor. The test instrumentation included a 5kHz high-speed camera, a 20kHz accelerometer (located at the FDR), and a load cell (located at the impactor). Figure 20 shows the test setup schematic and the actual test setup.

Table 22. Board assembly LVI - Impact conditions.

Tup Diameter [mm]	Drop Height [mm]	Drop Weight [kg]	Impact Velocity [mm/s]
15.875	106.35	2.708	1,457

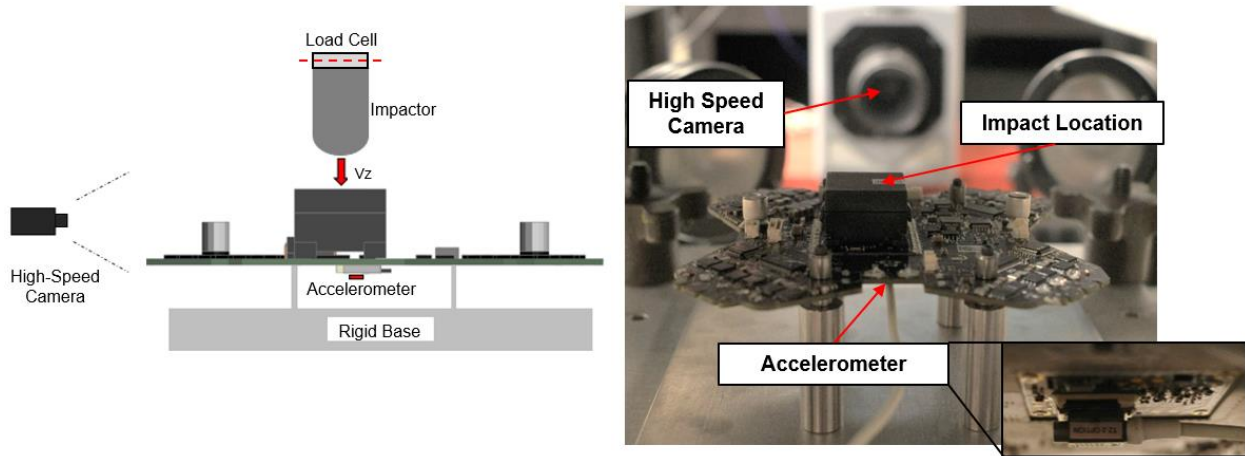


Figure 20. Board assembly LVI - Test schematic (left) and test setup (right).

The test fixture and the impact were discretized using 3D elements. Table 23 contains the element count for the entire model. As previously explained, the battery cables were removed for this test. Therefore, the discrete beams were removed from the FEM.

Table 23. LVI FEM - Element count.

1D Elements	2D Elements	3D Elements
0	8,456	19,524

The PCB was connected to the fixture using **NODAL_RIGID_BODY* [41] constraints at the fastener locations. The interaction between the PCB components was defined using an **AUTOMATIC_SINGLE_SURFACE* contact, and the contact between the impactor and the Inertial Measurement Unit (IMU) was defined using an **AUTOMATIC_SURFACE_TO_SURFACE* type of contact. A cross-section reading was defined to capture the impact load profile. The impactor velocity was defined using the **INITIAL_VELOCITY* card, applying the velocity recorded at the test prior to the impact. The

accelerometer was modeled with an **ELEMENT_ACCELEROMETER* with the same mass properties and sampling rate as the one used for the test. The boundary conditions were replicated by constraining all the degrees of freedom at the base-plate. The top displacement was also tracked during the analysis by defining a nodal output in the model. Figure 21 presents the FEM details and a comparison of the test setup to the FEM.

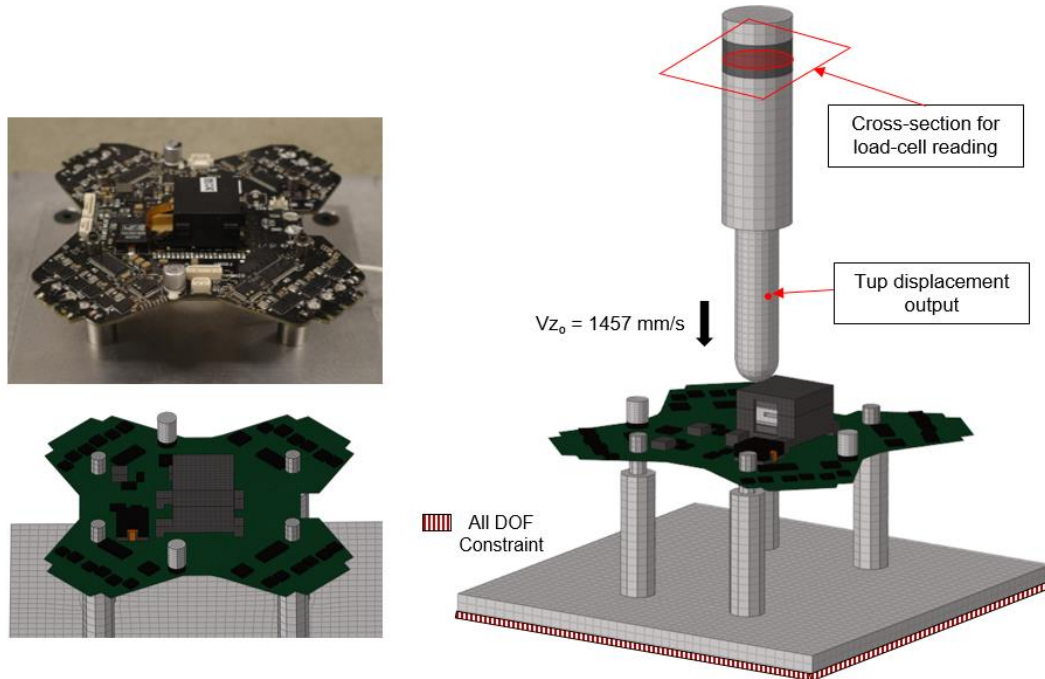


Figure 21. Board assembly LVI – FEM details and comparison to test setup.

Leveraging the work presented in Section 4.2, the structure's damping coefficient was estimated using the accelerometer data. The modal analysis solution was used to apply the damping ratio to the ten first modes without considering the rigid body modes (the constraints in the modal analysis were identical to the test). A damping of 4% of the critical damping was applied to the 488-1453Hz frequency range. Figure 22 depicts the ten first modes extracted from the modal analysis. The displacement contour shows the shape of the vibration for each frequency. The magnitude of the displacement is not meaningful since there are no loads applied in the analysis

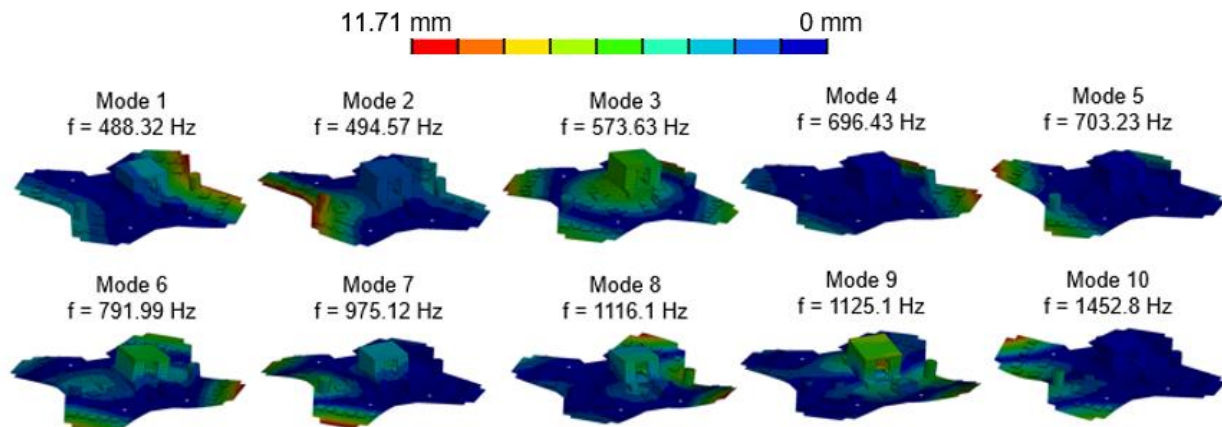


Figure 22. LVI FEM - Ten first modes of the modal analysis.

The validation of the PCB FEM was carried out by comparing the structure's transient response after the impact, the accelerometer data, the impactor's load profile, and the top's displacement. The mounting brackets of the IMU's lightweight housing failed during the test. Since the FEM simplifies this component as a single part with no connections, all the comparisons consider only the time up to the failure event. Figure 23 shows the failed brackets after the test.

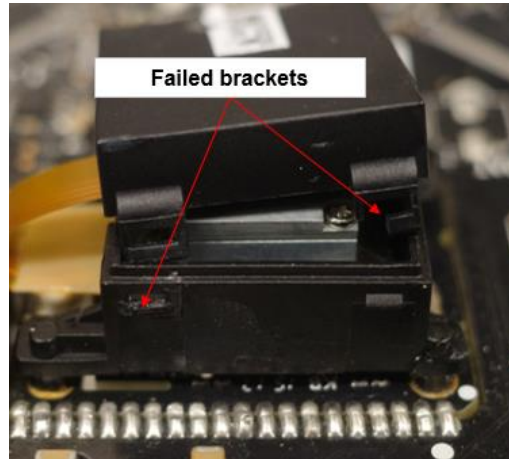


Figure 23. Board assembly LVI test - IMU's failed brackets.

Figure 24 compares the kinematics between the test and simulation at three different instances of the impact event. The simulation is able to predict the bending shape of both the PCB and the IMU's lightweight housing.

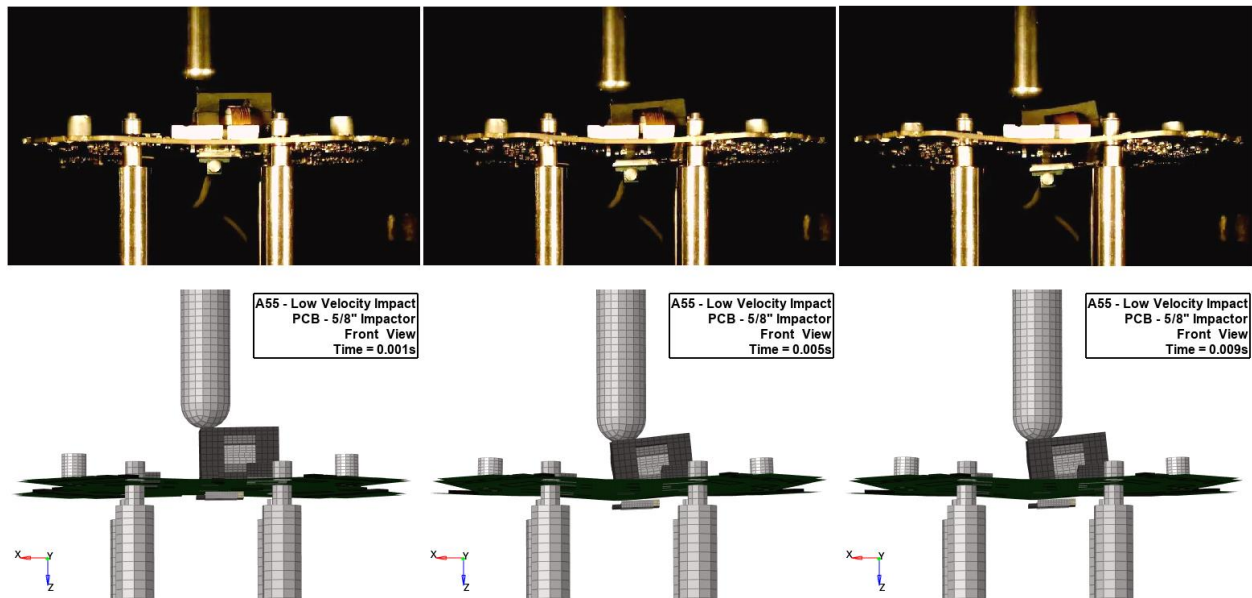


Figure 24. Board assembly LVI - Front view comparison of the test and simulation kinematics.

Figure 25 compares the load cell reading to the cross-section load extracted from the simulation. Both signals were filtered with a low-pass 9kHz Butterworth filter. The simulation overpredicts the first peak by 15% and the maximum load by 13%. During the simulation, it was observed that the impactor started to slide across the IMU's top face close to the failure event, generating side

loads. This sliding behavior was not observed in the simulation. The FEM does not consider the drop tower mechanism and the impactor's arm. Hence the moment generated by the impact force is not transferred in the simulation, and all the load is transferred vertically. Also, the materials used in the simulation are representative of the ones found in the specifications of the PCB components. Furthermore, the PCB has a cutout at the center, where solder joints connect a smaller board. The FEM simplifies this cutout and models the PCB as a single board. Figure 26 illustrates the discrepancies between the test article and the FEM.

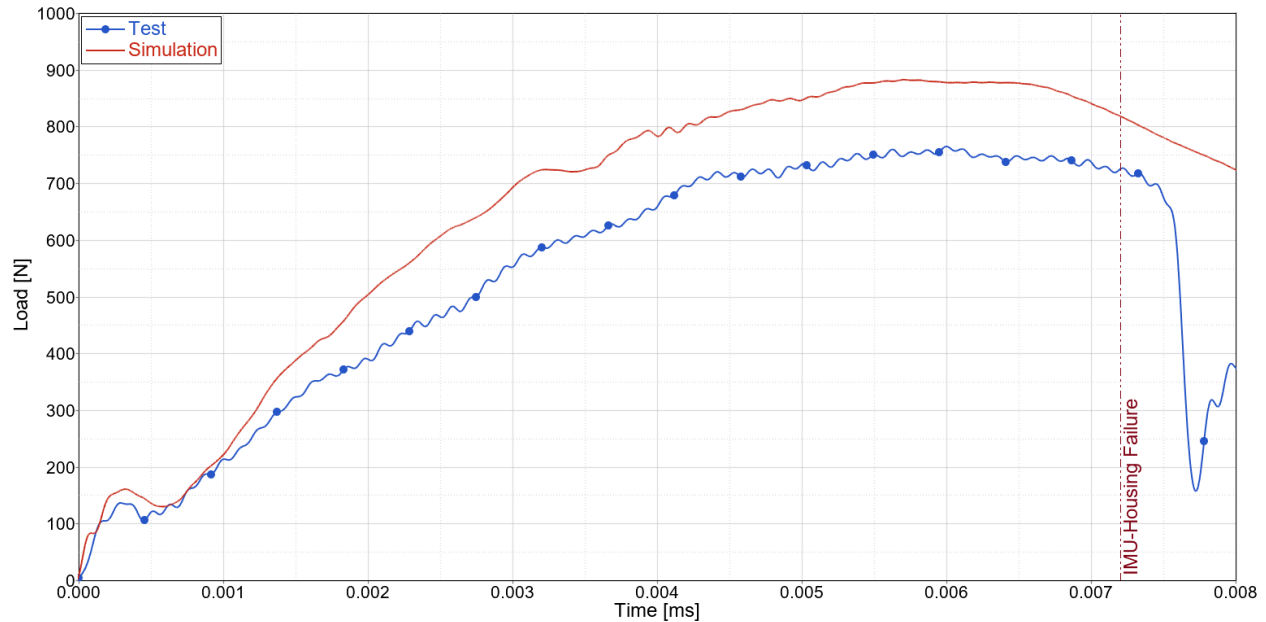


Figure 25. Board assembly LVI – Load cell data validation.

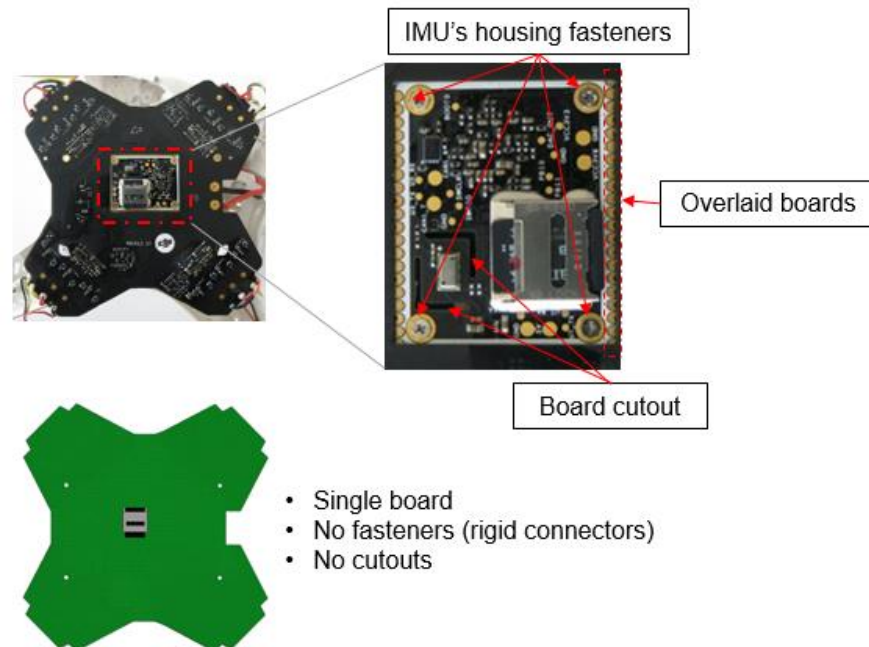


Figure 26. Board assembly LVI – Discrepancies between test specimen and FEM.

Considering all the simplifications and the discrepancies between the FEM and the test specimen, the load correlation was fairly accurate, capturing the overall shape and the peak load with a deviation of 13%. Therefore, the load data validation was considered successful.

Figure 27 compares the tup's displacement with the predicted displacement by the simulation. In this case, the correlation is excellent, with a small deviation (less than 2%) when the IMU's housing failure initiates.

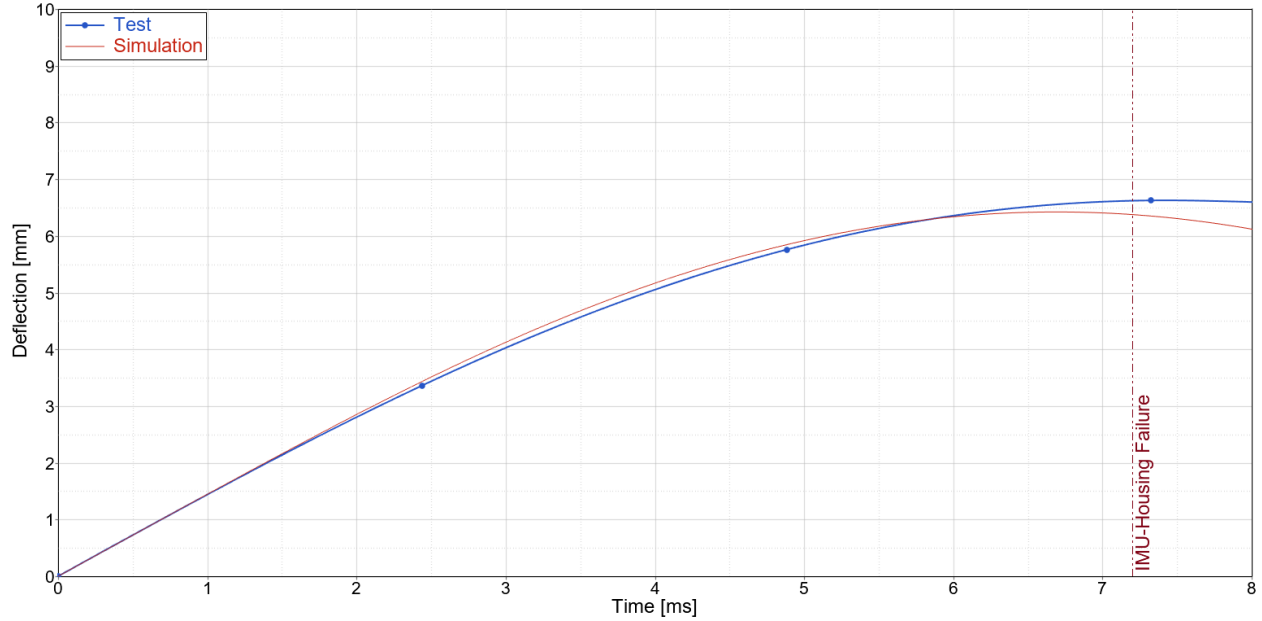


Figure 27. Board assembly LVI – Tup displacement data validation.

To conclude the validation exercise, the accelerometer data was compared to the acceleration predicted by the FEM. During the acceleration data validation process, it was observed that the results were highly influenced by the location of the **ELEMENT_ACCELEROMETER* and the output frequency. This is associated with the high-frequency oscillations of this type of impact event and the numerical noise in explicit solutions. This numerical noise mainly affects accelerations and contact forces. It is less critical in strains, stresses, and velocities, and it rarely affects displacements because these have a lower amplitude [43]. To avoid the solution dependency on the requested location and the contact noise, it was decided to compare the acceleration data to the rigid body acceleration of the FDR. By doing so, high oscillations coming from noisy nodes are averaged with the accelerations computed at the remaining nodes. Although the noise is not completely removed, it is significantly reduced.

Figure 28 compares the experimental data to the acceleration predicted by the simulation. Note that both experimental and simulation data sets are unfiltered. The comparison shows a higher frequency content in the numerical solution, affected by the numerical noise. Nevertheless, the simulation is able to predict similar magnitudes during the entire impact event. The maximum acceleration is overpredicted by 24%. Considering all the simplifications introduced in the FEM, the challenges associated with the numerical noise present in this type of analysis, and the repeatability issues associated to this type of test, the deviation was considered acceptable.

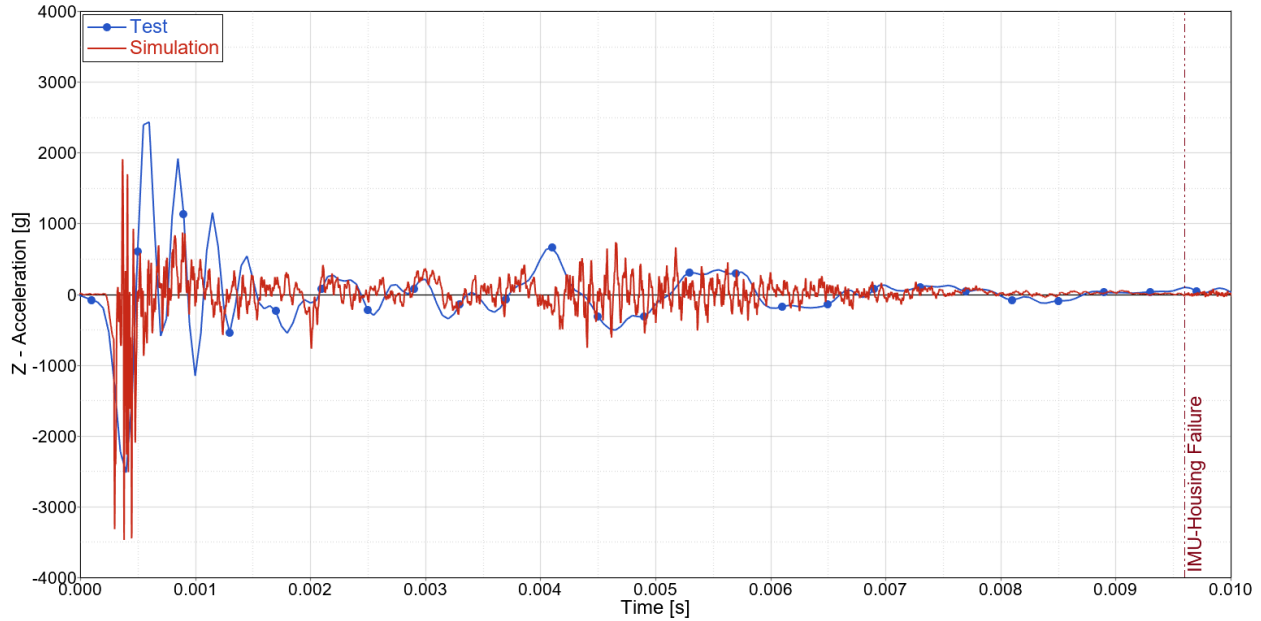


Figure 28. Board assembly LVI – Accelerometer data validation.

Considering all the challenges faced during the acceleration data validation and the low repeatability of this type of impact event, it is highly unlikely to obtain a similar response for two consecutive tests. Thus, it is not recommended to use this type of data for a comparison to the values specified in the standards. Furthermore, the peak acceleration has a duration of less than 0.25ms for the test and less than 0.1ms for the simulation. Designing a mechanical test able to subject the structure to such a shock profile in a controlled manner is practically impossible. In fact, Kordowski, P., et al. [44] already tried to design an impact shock test for a miniaturized FDR using the shock profile specified in ED-112F. Figure 29 illustrates the shock profile specified in ED-112.

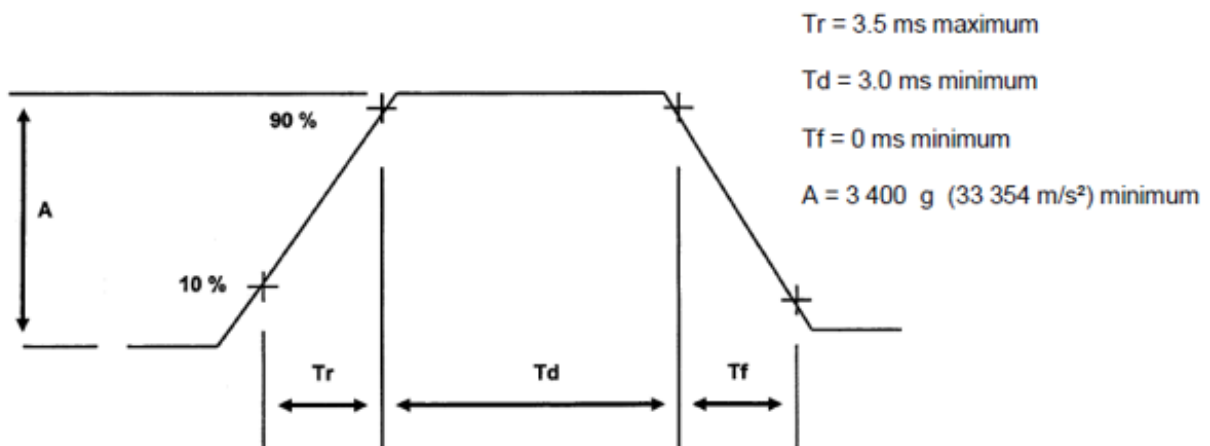


Figure 29. Shock profile specified in ED-112 [6].

The test consisted of a pneumatic gun launching a measuring probe towards a braking stand, where the test specimen was attached to a rigid base. Although the energy requirements were met (the area under the curve was greater than the specified in ED-112), the shock acceleration profile obtained during the test was significantly different from the one defined in the standard. Figure 30 compares the experimental profile to the profile specified in the normative.

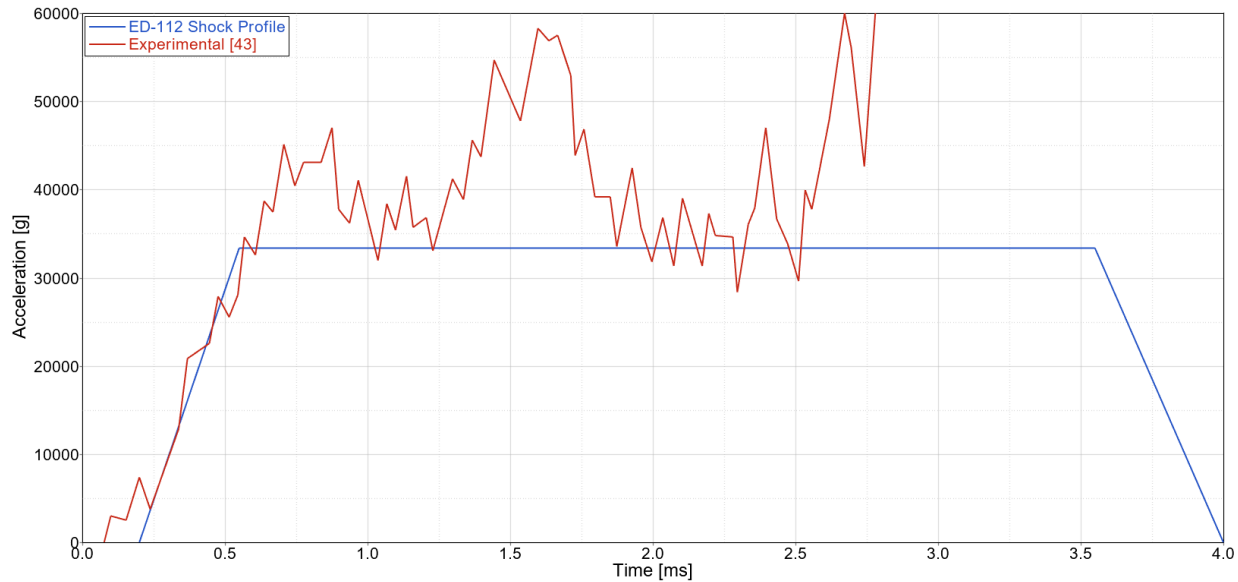


Figure 30. ED-112 shock profile and shock profile obtained by Kordowski, P., et al. [44].

Note that ED-112 specifies that significant ringing of the shock pulse can be observed during the test [6]. The document also suggests using an averaging method to establish an effective pulse shape. The forecast study in Section 2.1 showed that most sUAS use micro SD cards as FDRs. Therefore, the standard shock profile described in JESD22-B104C Condition B (1,500g - 0.5ms) was taken as a reference to compare the effective average acceleration obtained from the numerical analysis.

An averaging function was applied to the LVI experimental and numerical acceleration responses. The averaging function computes the maximum average acceleration for a defined time interval. According to the JESD22-B104C Condition B, a window of 0.5ms was defined. Figure 31 compares the maximum average accelerations computed using the test and simulation resultant acceleration profiles. Note how the acceleration peaks affected by the noise do not significantly affect the effective acceleration since the duration of these peaks is very short. The simulation underpredicts the effective acceleration by 18%, which is acceptable considering the simplifications introduced in the FEM.

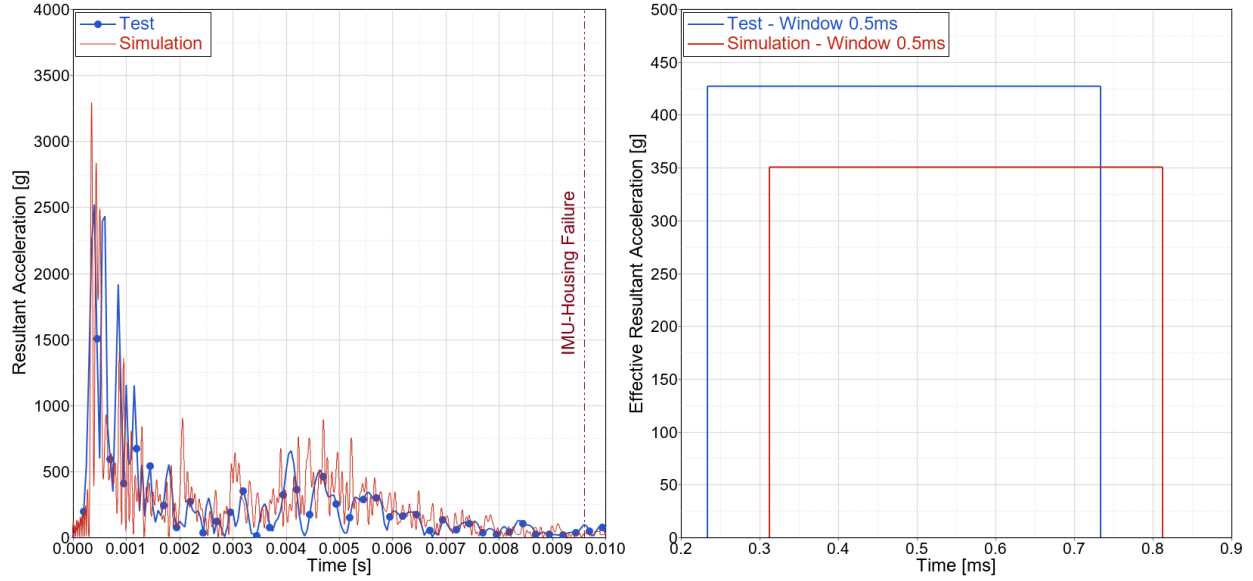


Figure 31. Board assembly LVI – Maximum effective acceleration validation.

4.4 Conclusions

Based on the results obtained from this study, it was concluded that the FEM methodologies learned from the literature review and the preliminary analyses are applicable to UAS onboard assemblies. The LVI test data was valuable for validating these methodologies, which proved to be effective in predicting the displacements, loads, and accelerations of the structure during the impact event, even when the small components are simplified.

By observing the test and simulation data, it was possible to evaluate other important factors, such as the test repeatability and the challenges associated with the acceleration data. To facilitate the comparison between the acceleration values obtained from the numerical analyses and the “effective acceleration” defined in the standards such as JESD22-B104C, it was decided to apply an averaging function that computes the maximum average acceleration during a defined time interval. This methodology is consistent with previous work done in this field [44] and recommendations found in mechanical standards for FDRs, such as ED-112.

The time interval specified in JESD22-B104C Condition B (0.5ms) was selected, which is the most common for micro SD cards, the preferred solution for recording data in UAS. By applying this post-processing methodology, it was possible to compare the experimental and numerical effective acceleration values. The effective shock profile is more suitable for comparison with the profiles specified in the shock mechanical standards and hence can be taken as a reference to design new test procedures or to evaluate the possibility of adjusting the existing ones to suit the expected levels in a UAS crash scenario.

5. CRASH ANALYSES OF SMALL AND MEDIUM-SIZED UAS WITH FDR

This chapter presents the full-scale collision studies for three different small and medium-sized UAS. The small and medium-sized UAS considered for these studies are NIAR's Fixed-Wing 2.55lb., Quadcopter 2.7lb., and Fixed-Wing 55lb. FEMs. The targets were selected to encompass a range of realistic scenarios, such as airborne collisions, operations over people, operations near moving vehicles, and different ground surfaces.

5.1 UAS Finite Element Models

The UAS FEMs presented in this chapter were developed in previous ASSURE research tasks. Therefore, the reader is encouraged to refer to the published ASSURE's reports for a detailed explanation of the FEM development process. Table 24 presents the projects for which each UAS FEM was developed, along with the corresponding references.

Table 24. UAS FEMs and development project.

UAS FEM	Report
Fixed-Wing 2.55lb.	A14 – Annex B [45]
Quadcopter 2.7lb.	A3 [46], A14 – Annex B [45] and A16 [47]
Fixed-Wing 55lb.	NIAR Internal Report UAS-0001 [48]

All the models were developed following a physics-based modeling approach. This methodology, developed by NIAR, takes advantage of the latest advances in computational tools, years of research in understanding the fundamental physics of the crashworthiness event, generated test-to-test variability data, and verification and validation modeling methods. Figure 32 combines all these methodologies and modeling concepts into the well-established Building Block Approach.

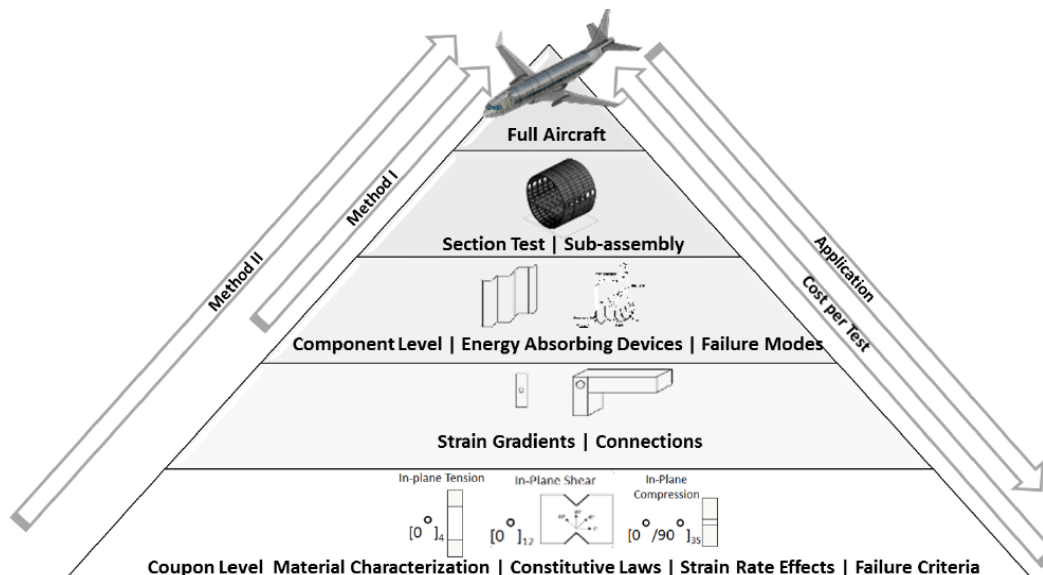


Figure 32. NIAR Building Block Approach.

Additional changes were made to the latest UAS versions to include an FDR. Note that the FDR FEM is referred to as “Virtual Sensor” (VS) in this work.

5.1.1 UAS 2.55 lb. Fixed-Wing

This fixed-wing UAS, representative of the EbeePlus, has a particular foam construction that acts as a protection to the internal components, such as the battery or the camera. The selection of this UAS was driven by the objective of investigating the impact of foam-based structures on the loads and accelerations transferred to the FDR during a crash scenario. Table 25 summarizes relevant specifications of this UAS. Figure 33 presents the isometric, top, side, and front views of the FEM.

Table 25. UAS 2.55lb. Fixed-Wing specifications.

MTOW	2.55 lb. (1.16 kg)
Wingspan	3 ft. 7.3 in. (1099.8 mm)
Length	1 ft. 7 in. (482.6 mm)
Cruise Speed	50 knots (97.19 m/s)

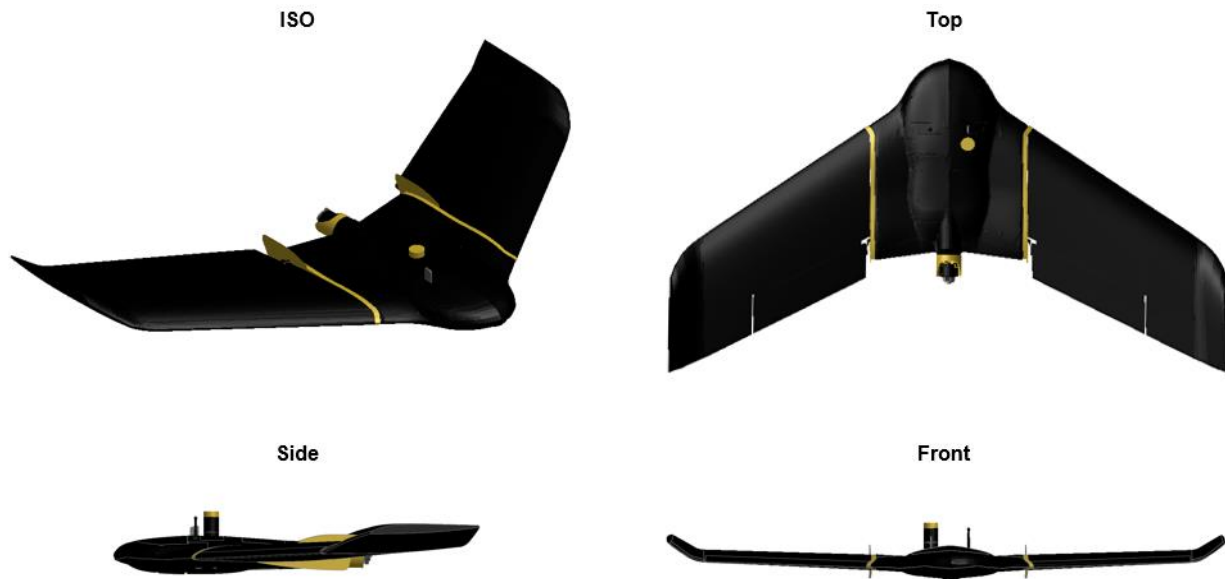


Figure 33. UAS 2.55 lb. Fixed-Wing (EbeePlus) FEM.

The UAS 2.55 lb. Fixed-Wing FEM (F2.55) was developed in Task A14 [45]. Several coupon, component, and full-scale test and validation exercises were developed to calibrate and validate this FEM. Figure 34 depicts some details of the geometry and FEM development processes.

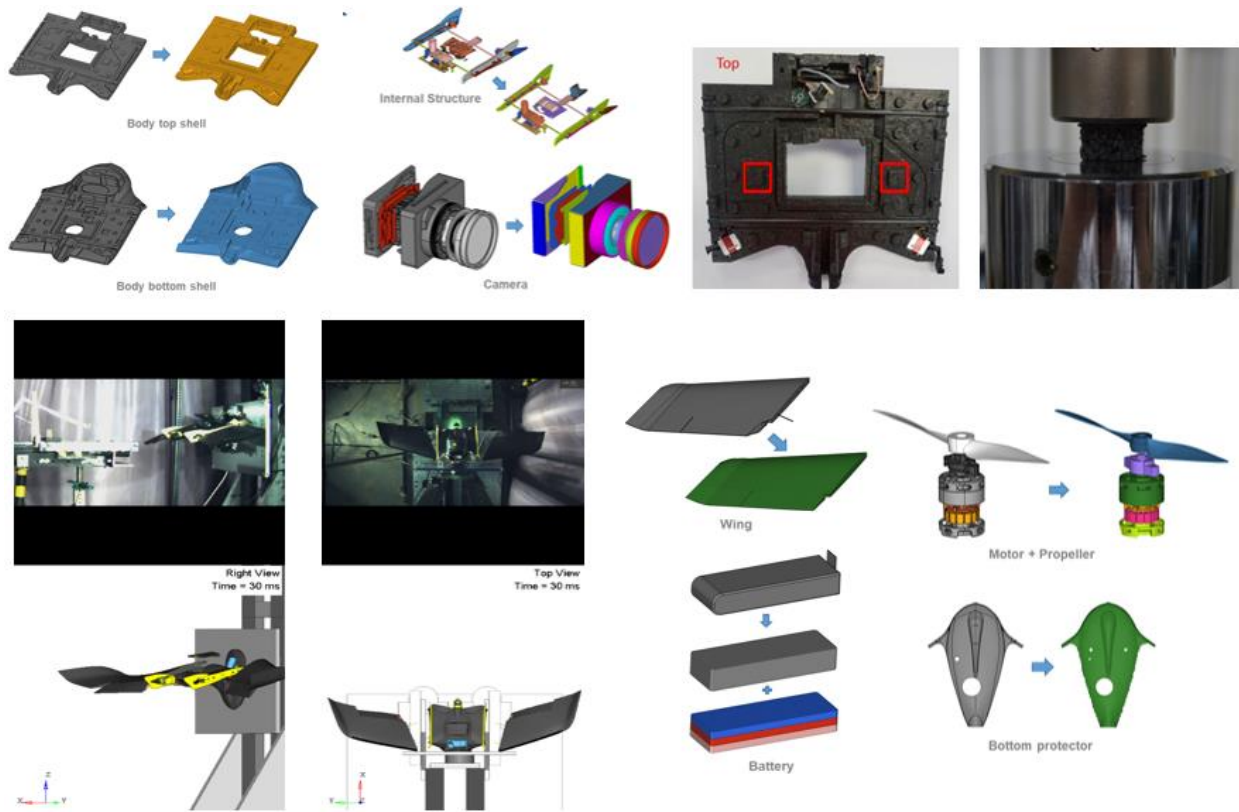


Figure 34. F2.55 FEM development process [45].

The F2.55 FEM was modified to include the VS. According to the EbeePlus user's manual; the UAS stores the flight data in a memory card located at the camera. The camera FEM was modified to include the card slot that allows the connection with the VS. The VS was taken from the LVI analysis presented in Section 4.3. However, the card socket and the metallic shell were removed to represent the actual connection for this UAS. Additionally, three cross-section readings were defined in the VS FEM to collect the impact loads during the simulation. Figure 35 presents the VS for the 2.55 lb. fixed-wing UAS and the defined cross-sections. The VS was connected to the camera using **NODAL_RIGID_BODY* constraints. Figure 36 shows the details of the FEM modification.

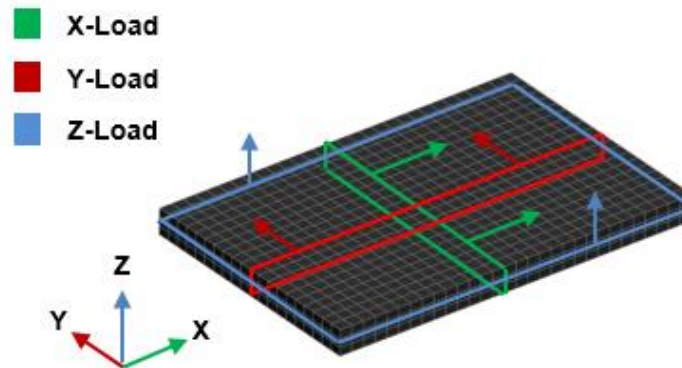


Figure 35. Virtual Sensor FEM and cross-section definitions.

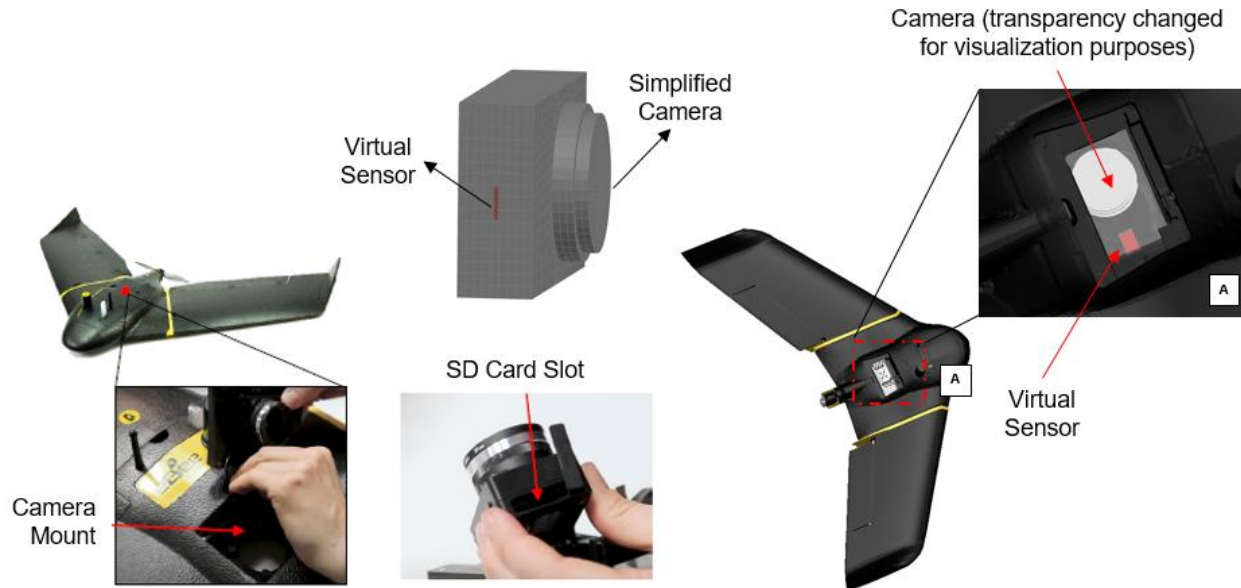


Figure 36. F2.55 FEM modification – Virtual Sensor.

5.1.2 UAS 2.7 lb. Quadcopter

The forecast study presented in Appendix A shows that DJI produces 76% of the UAS global market. Additionally, the DJI Phantom 3 was identified as the most common quadcopter in the sUAS market during Task A3 [46]. The UAS 2.7 lb. Quadcopter FEM (Q2.7), which is a representative model of the DJI Phantom 3, was developed in Task A3 [46]. Therefore, it was decided to take advantage of this available model to study the loads and accelerations at the VS during a crash scenario for a sUAS with a quadcopter architecture.

Table 26 summarizes the relevant specifications of this UAS. Note that during the literature review phase of A3, it was found that some newer UAS models of similar type had enhanced these specifications, with maximums speeds of up to 20m/s (38.8). Therefore, the analyses presented in this work use a maximum velocity of 38.8 knots for the Q2.7 FEM. Figure 37 illustrates the top and front views of the FEM.

Table 26. Relevant specifications of the DJI Phantom 3 [47].

Mass	1,216 g	2.68 lb.
Diagonal	350 mm	13.8 in
Max. Horizontal Speed	16 m/s	31 knots
Max. Service Ceiling	6,000 m	19,685 ft.
Electronic limit above ground	120 m	394 ft.
Max. Motor Speed	1,240 rad/s	11,840 rpm
Motors	4x brushless DC motors; mass: 54 g	
Battery	4x LiPo cells; capacity: 4480 mAh; mass: 363 g	

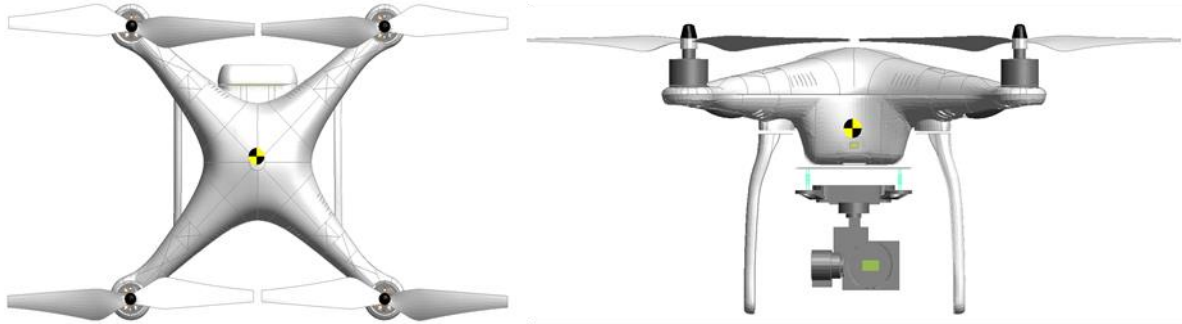


Figure 37. UAS 2.7 lb. quadcopter FE model center of gravity [47].

This FEM has been extensively evaluated and validated for multiple impact conditions, from Anthropomorphic Test Devices (ATD) [45] to aircraft metallic [46] and composite structures [47]. Furthermore, this FEM has been validated for impact velocities up to 500 knots. The work presented in [45], [46], [47], and [49] details all the coupon, component, and full-assembly tests and validation exercises for this UAS. Figure 38 depicts some details of the geometry and FEM development processes.

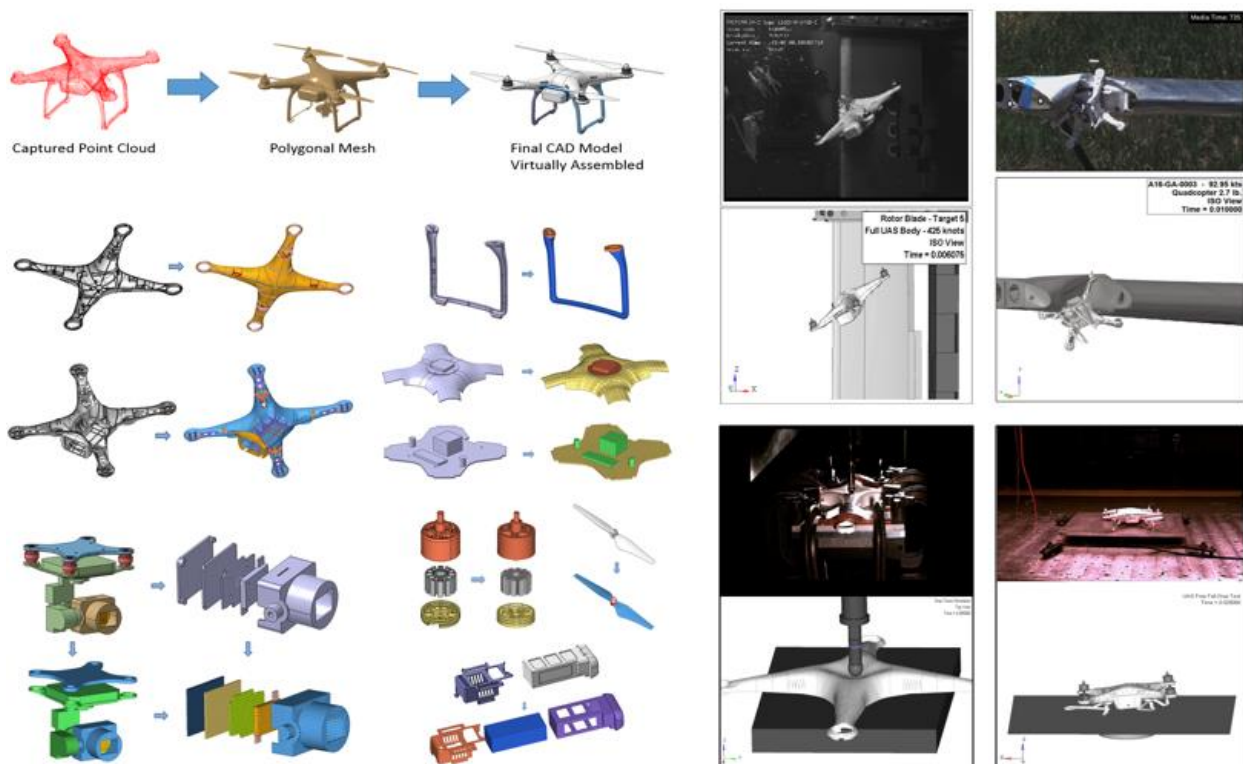


Figure 38. UAS 2.7 lb. Quadcopter FEM development process [45][46][47][49].

The Q2.7 FEM was modified by including the detailed PCB FEM developed during the LVI validation exercise, presented in Section 4.3. The same fastener definition used in the old model was selected for the four connections to the battery carcass. The power battery cables, modeled in the detailed PCB, were connected to the PCB and the battery port by means of

**NODAL_RIGID_BODY* connectors (NRBs). The VS architecture is the same as presented for the LVI test, with the VS connected to the socket and metallic shell through NRBs. The VS was modified to include the cross-section readings presented in Figure 35. Note that the card socket is glued to the PCB in the actual test specimen. This connection was also simplified with an NRB. Figure 39 shows the connections created in the FEM. Figure 40 compares the PCB of the modified FEM to the actual DJI Phantom 3 electronics board. Note that some of the internal components were hidden for illustration purposes.

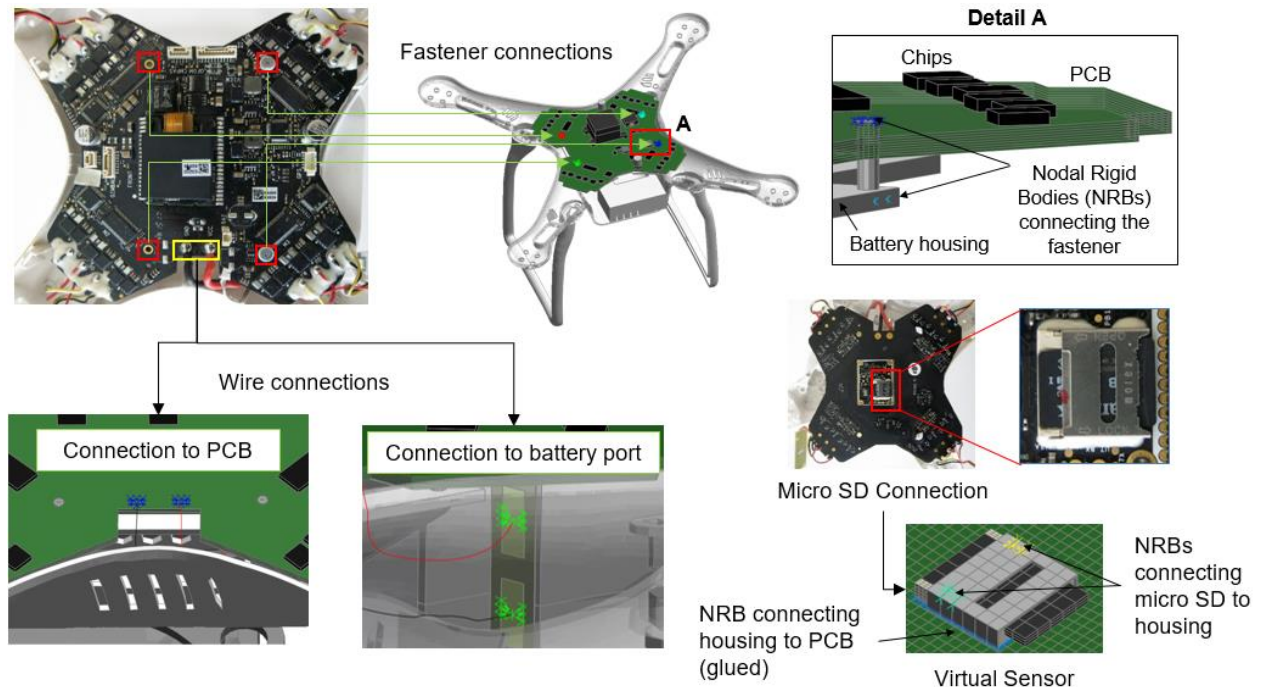


Figure 39. A55 Q2.7lb. FEM – PCB and Virtual Sensor connections.

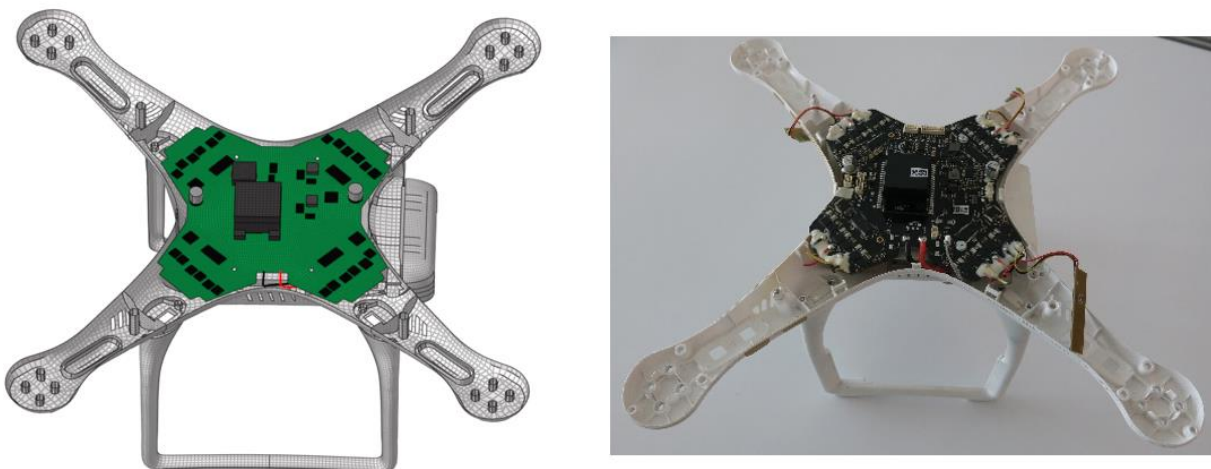


Figure 40. Comparison of the Q2.7 FEM board assembly to the actual DJI Phantom 3.

The critical time step of the model was checked to ensure that the applied changes did not incur additional computational costs. The critical time step was kept, and the mass deviation between

the old model and the updated model was 0.38%. Figure 41 compares the A16 Q2.7 FM to the updated A55 Q2.7 FEM.

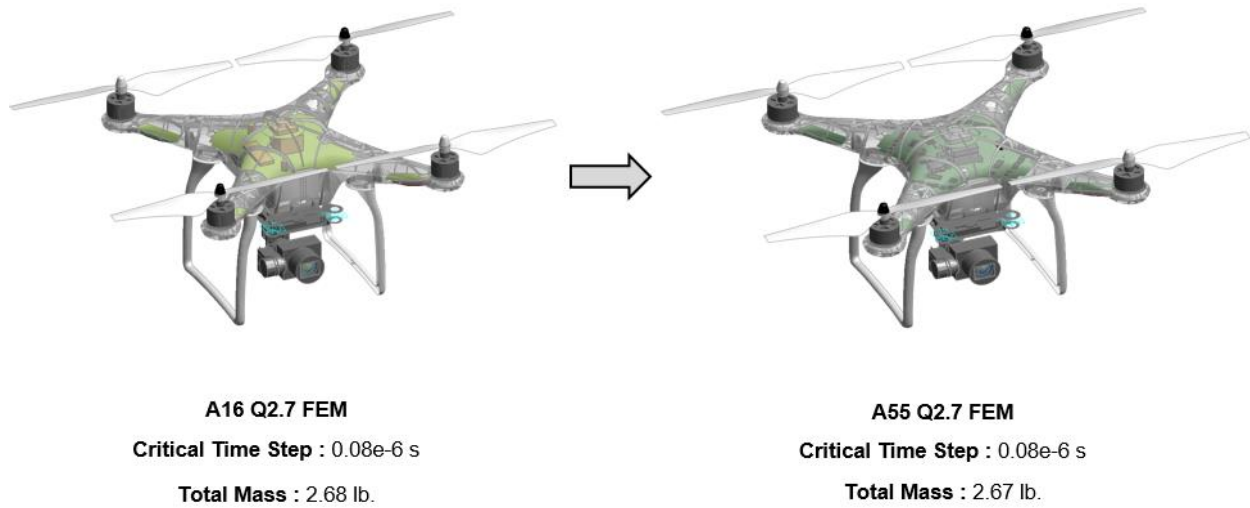


Figure 41. A16 Q2.7 FEM vs. A55 Q2.7 FEM.

5.1.3 UAS 55 lb. Fixed-Wing

The UAS 55 lb. Fixed-Wing FEM (F55) is a scaled version of a full-scale search and rescue UAS built during a collaboration with an industry partner [48]. Figure 42 depicts some stages of the UAS development and manufacturing process. Note that this UAS is a hybrid Vertical Take-off and Landing (VTOL)/Conventional Take-off and Landing (CTOL) configuration prototype. However, this work considers only the CTOL configuration. Table 27 contains the relevant specifications of the 55lb. NIAR UAS fixed-wing configuration.



Figure 42. Development of the NIAR-UAS hybrid VTOL/CTOL prototype [51].

Table 27. Relevant specifications of the 55lb. NIAR UAS fixed-wing configuration.

UAS Configuration	F55 (metric)	F55 (US)
Mass	25.0 kg	55.0 lb.
Length	1867.1 mm	73.5 in.
Wingspan	4200 mm	165.3 in.
Height	546.2 mm	21.5 in.
Cruise Speed	97.19 m/s	50 knots

The airframe of the UAS is composed almost entirely of laminated carbon fiber-reinforced polymer sheets, plates, and skins. The material properties of the composite components were extensively tested and documented in the NCAMP Qualification Report [50]. Additional drop tower testing was performed to characterize the impact performance of the material [51]. Figure 43 illustrates some stages of the FEM development process. Note that for this UAS, component and full-scale level testing were not performed. However, full-scale rigid wall impact analyses were developed to prove the model's good numerical stability for impact velocities up to 350 knots. Figure 44 presents the top, bottom, side, and front views of the FEM with the representative dimensions.

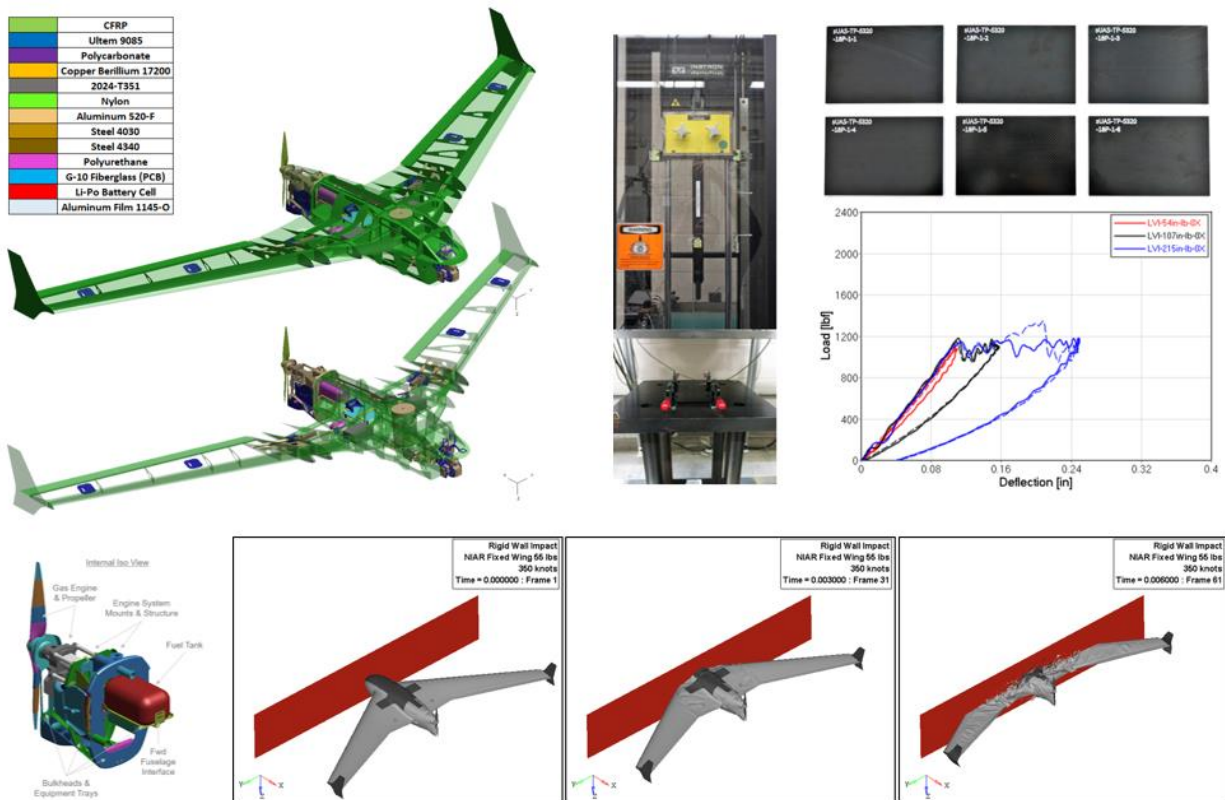


Figure 43. F55 FEM development process [51].

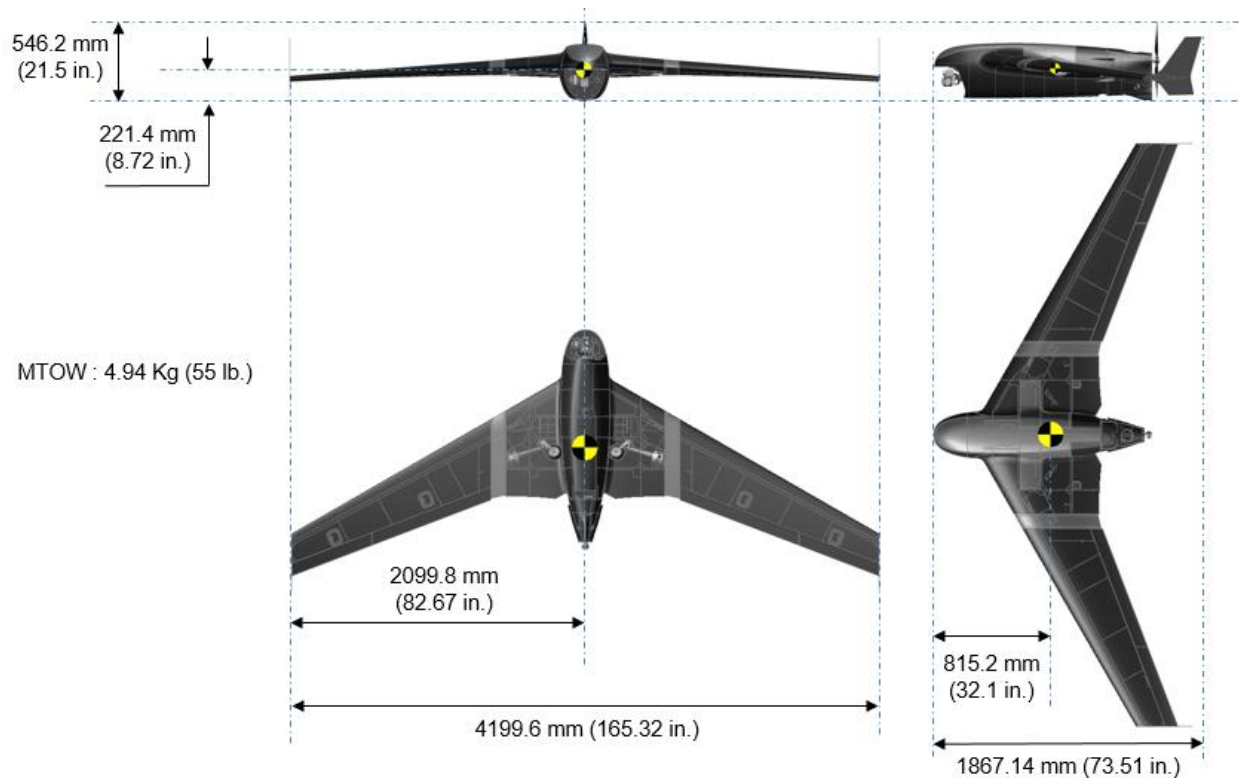


Figure 44. F55 FEM dimensions and MTOW.

The F55 FEM was modified to include the VS. The virtual FDR was located at the center of the electronics board, with the same architecture used for the Q2.7 FEM (card slot and metallic shell). The cross-section readings follow the same nomenclature and definition presented in Figure 35. Figure 45 shows the VS location in the FEM. The same connections used for the Q2.7 were assumed for the F55's VS (see Figure 39). Note that some internal components were hidden for illustration purposes.

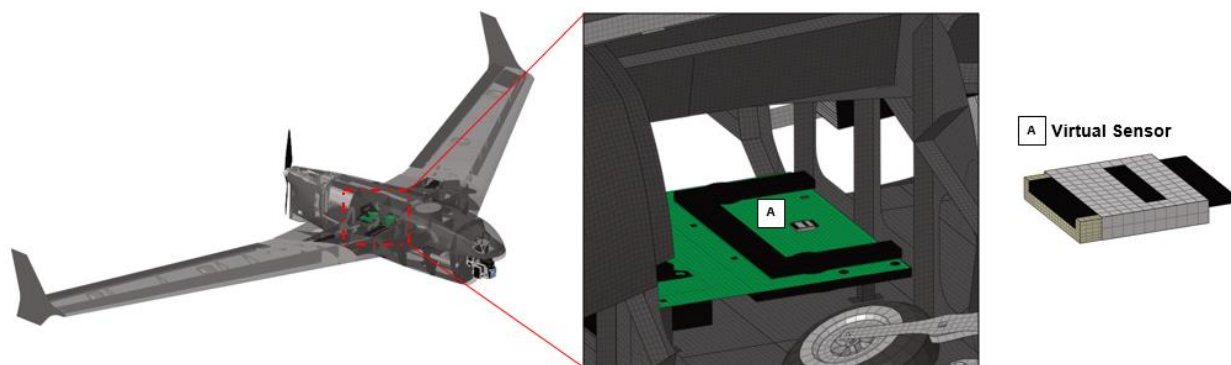


Figure 45. Location of the F55's VS.

5.2 Target Definition and Impact Location

The selection of targets aimed to encompass all the possible crash scenarios for the type of sUAS studied in this work. Taking advantage of the advanced computational models developed in previous ASSURE programs [46][47][49], a variety of metallic, acrylic, and composite aircraft structures were selected to perform impact analyses. The crash scenarios also consider operations around people [45], buildings, and moving vehicles. Additional critical impact conditions were developed to consider a sudden failure or UAS shutoff, which would lead to a freefall towards different surface types, such as water, wet soil, or concrete.

5.2.1 Aircraft Structures

Leveraging previous airborne collision studies, the following aircraft structures were selected as a target for the current work:

- General Aviation (G) – Windshield and wing [49]
- Business Jet (B) – Vertical stabilizer and wing [46]
- Commercial Transport (C) – Horizontal stabilizer and wing [46]
- Rotorcraft (R) – Front cowling and blade [47]

For a detailed description of the geometry and FEM development process (mesh, materials, connections, etc.), the reader is recommended to visit the reports published for each individual research task.

Note that these aircraft targets have not been previously analyzed for all the UAS considered in this work. The general aviation, business jet, and commercial transport structures have been analyzed for collision studies involving the Q2.7 and F55 FEMs. The rotorcraft structures have been analyzed for collision studies involving the Q2.7 FEM. The F2.55 was not involved in any of the airborne collision studies. Therefore, the criteria for selecting the worst case considers the highest damage severity level observed for any UAS collision studies. For a detailed description of the damage severity levels, refer to [47].

Table 28 documents the cases taken as a reference for the current work and the observed damage severity level. Figure 46 through Figure 53 illustrate the representative dimensions and the impact location for each target.

Table 28. Reference airborne collision studies, impact location, velocity, and severity level.

Target	Critical Impact Condition	Damage Severity Level
G – Windshield	Location 1 – Cruise Velocity	4
G – Wing	Location 1 – Cruise Velocity	4
B – Vertical Stabilizer	Location 3 – Cruise Velocity	4
B – Wing	Location 1 – Cruise Velocity	4
C – Horizontal Stabilizer	Location 1 – Cruise Velocity	4
C – Wing	Location 1 – Cruise Velocity	3
R – Front Cowling	Location 1 – Cruise Velocity	3
R – Blade	Location 1 – Cruise Velocity	2

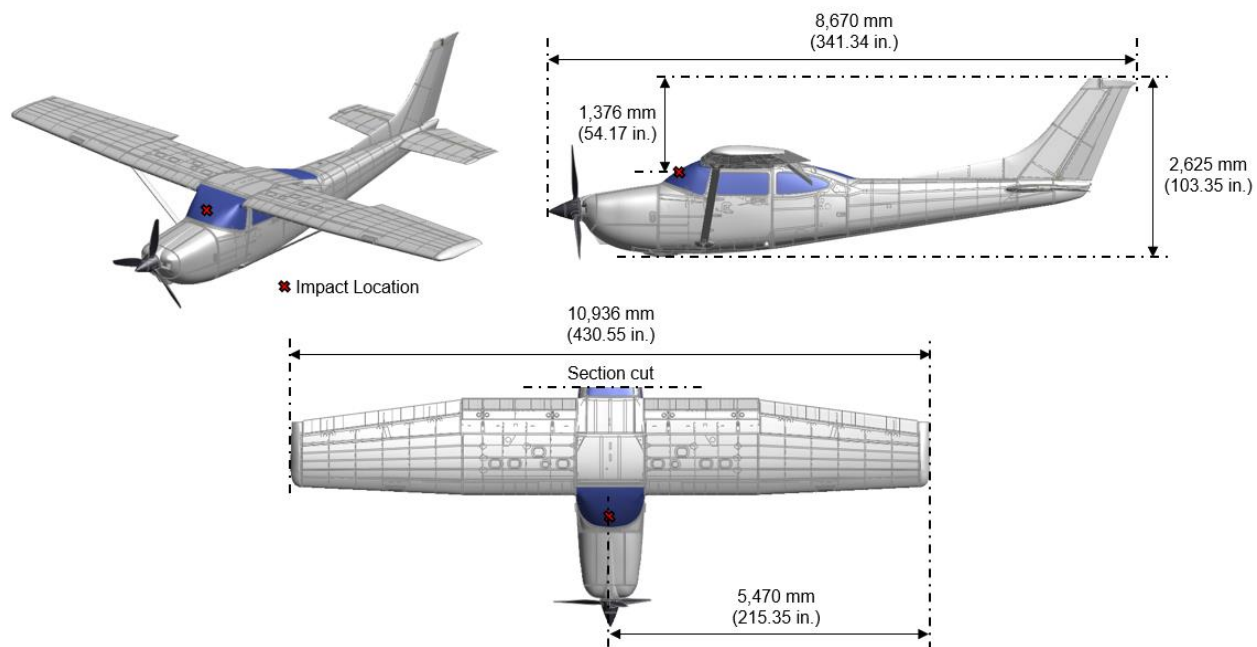


Figure 46. General Aviation FEM – Windshield impact location.

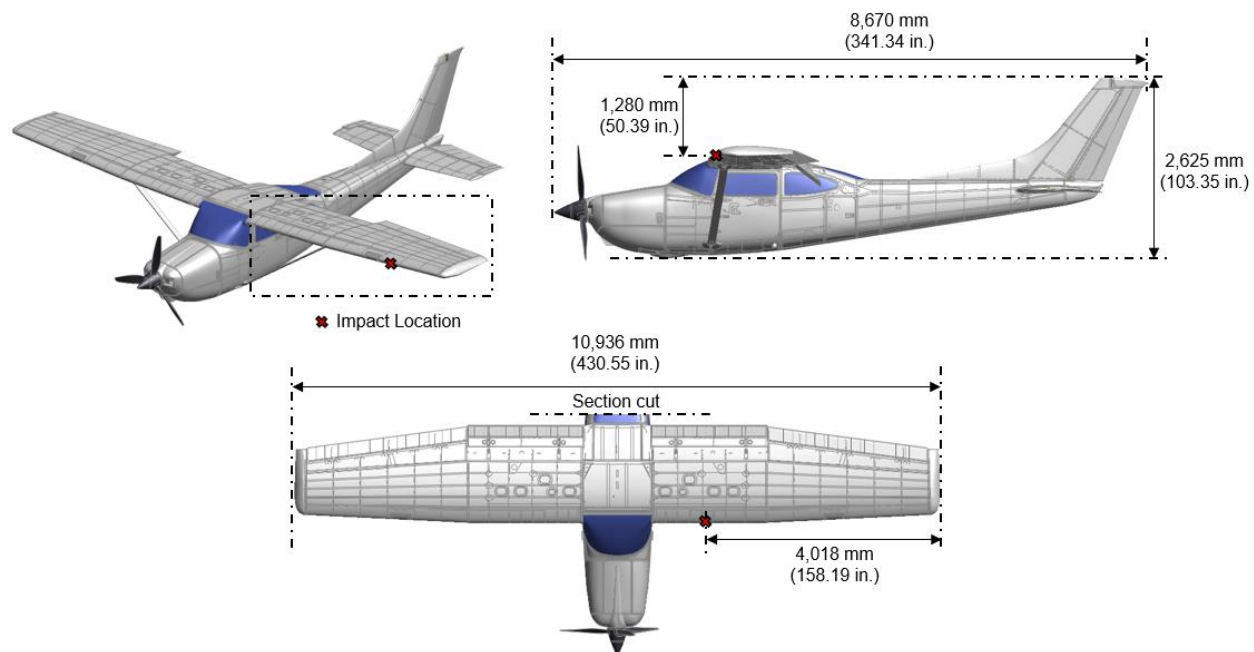


Figure 47. General Aviation FEM – Wing impact location.

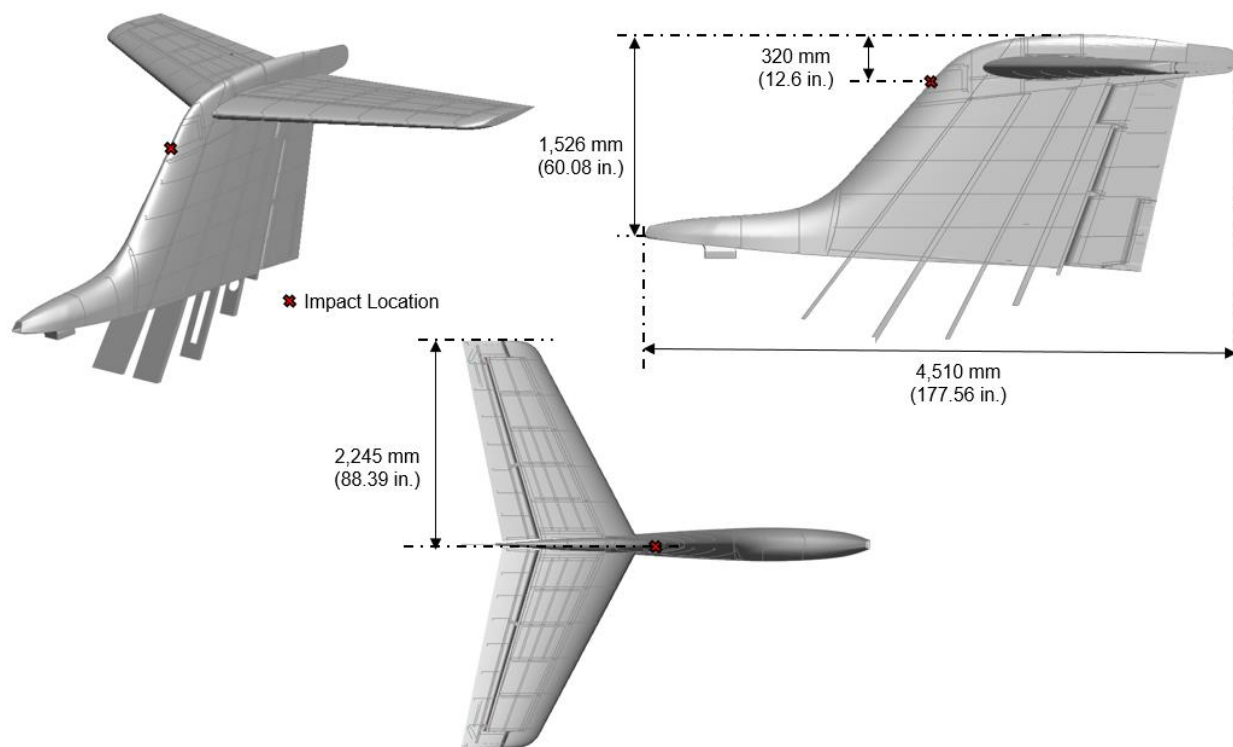


Figure 48. Business Jet FEM – Vertical stabilizer impact location.

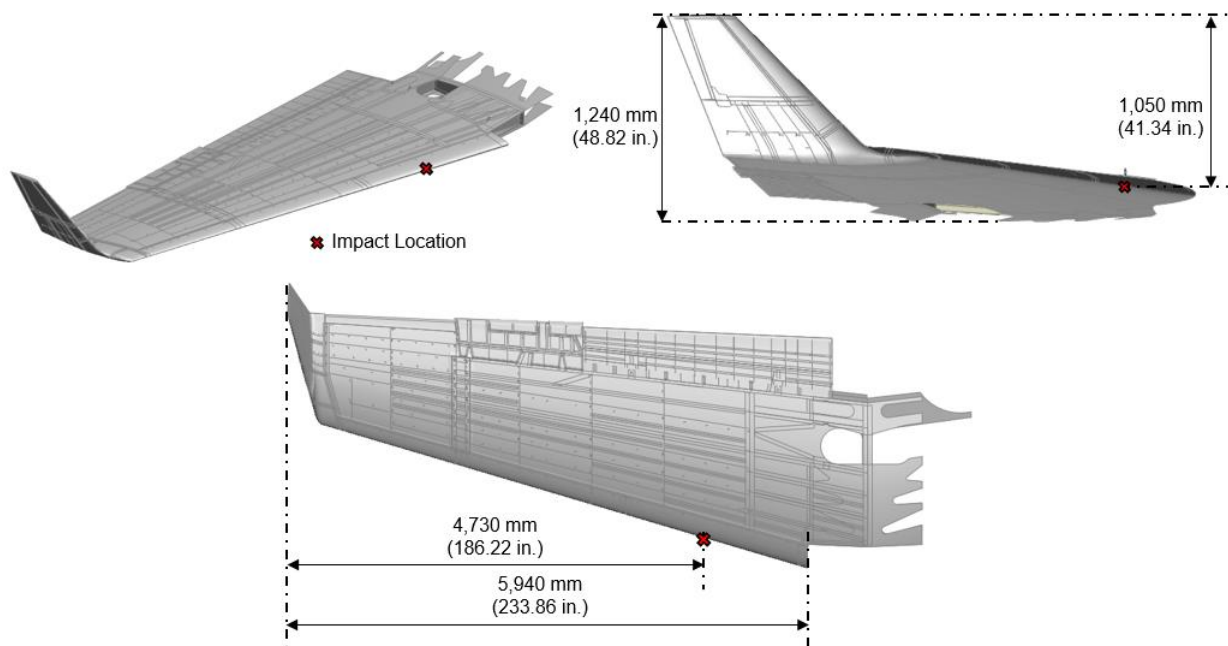


Figure 49. Business Jet FEM – Wing impact location.

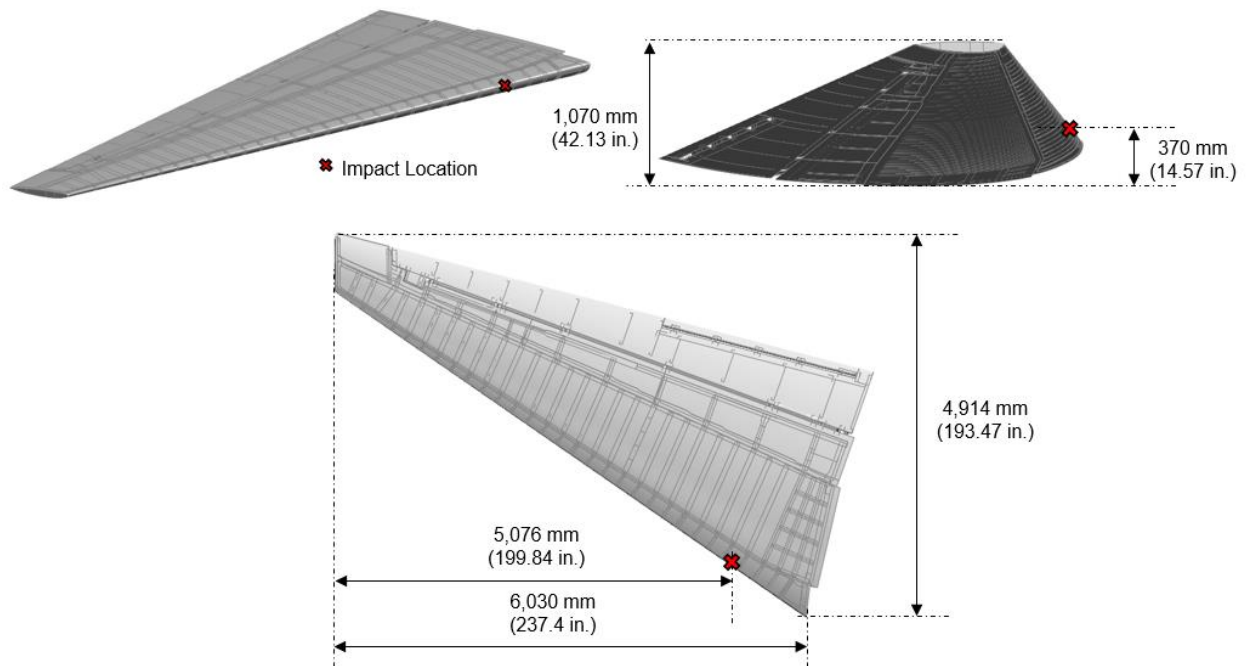


Figure 50. Commercial Transport FEM – Horizontal stabilizer impact location.

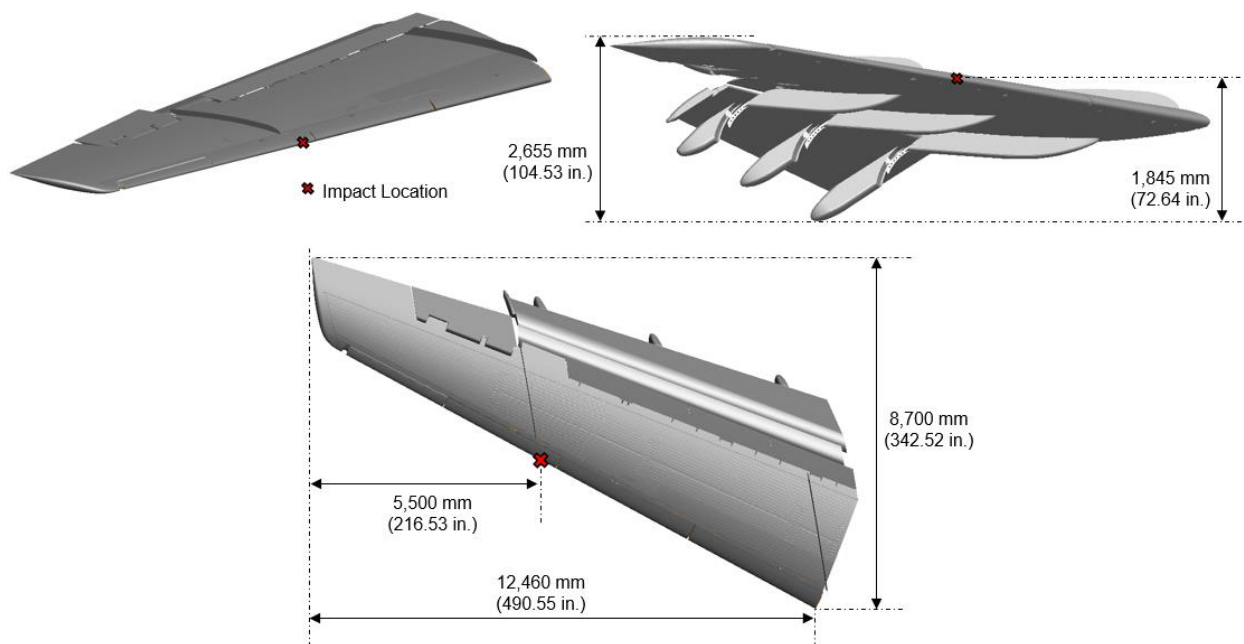


Figure 51. Commercial Transport FEM – Wing impact location.

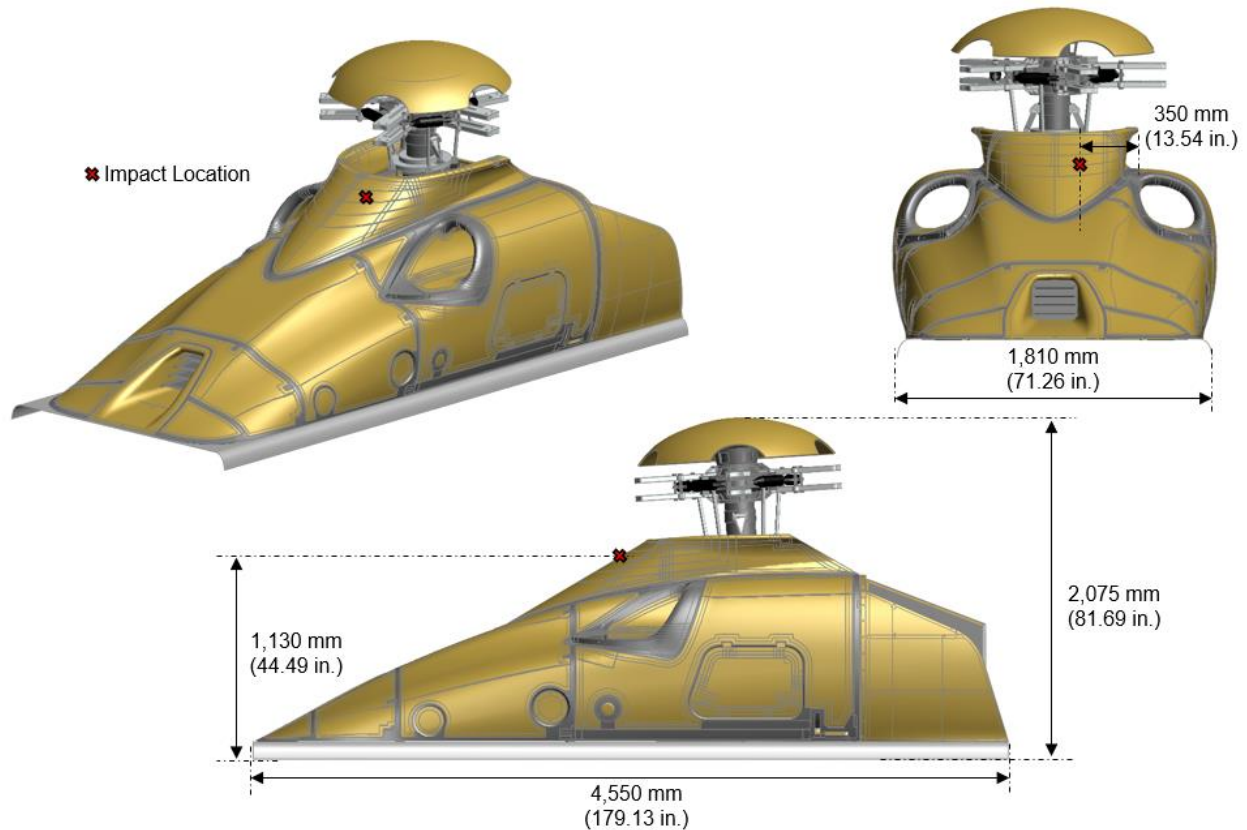


Figure 52. Rotorcraft FEM – Front cowling impact location.

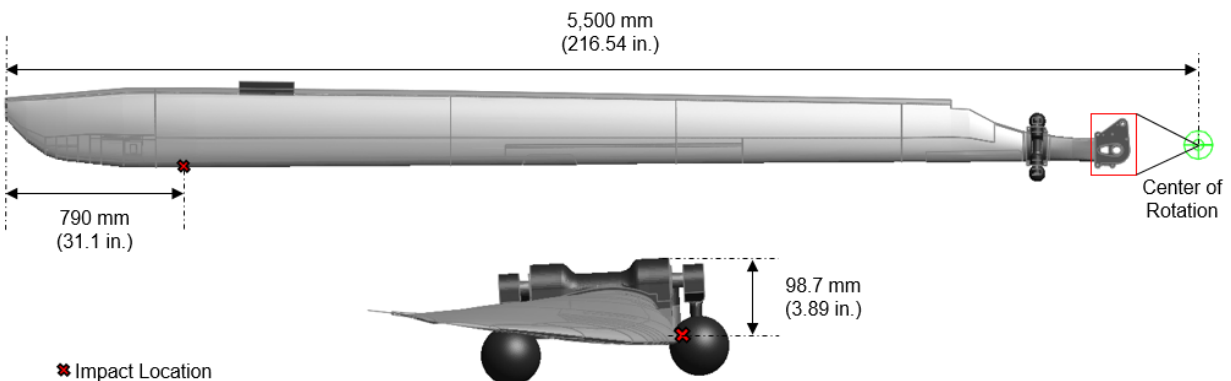


Figure 53. Rotorcraft FEM – Blade impact location.

5.2.2 Operation Over People

Leveraging previous work performed during the ground collision severity evaluation task [45], the front-angled impact condition described by Test 15 was selected as a reference for this work. This test is representative of a possible crash scenario involving a sUAS and a pedestrian. Test 15 was carried out by impacting the A14 ATD at the front of the head with the DJI Phantom 3 UAS. The impact velocity was 17.07m/s (33.18 knots), which is slightly above the maximum velocity for this UAS (16m/s – 31.1 knots). Figure 54 shows the test vs. simulation kinematics comparison reported in Task A14.

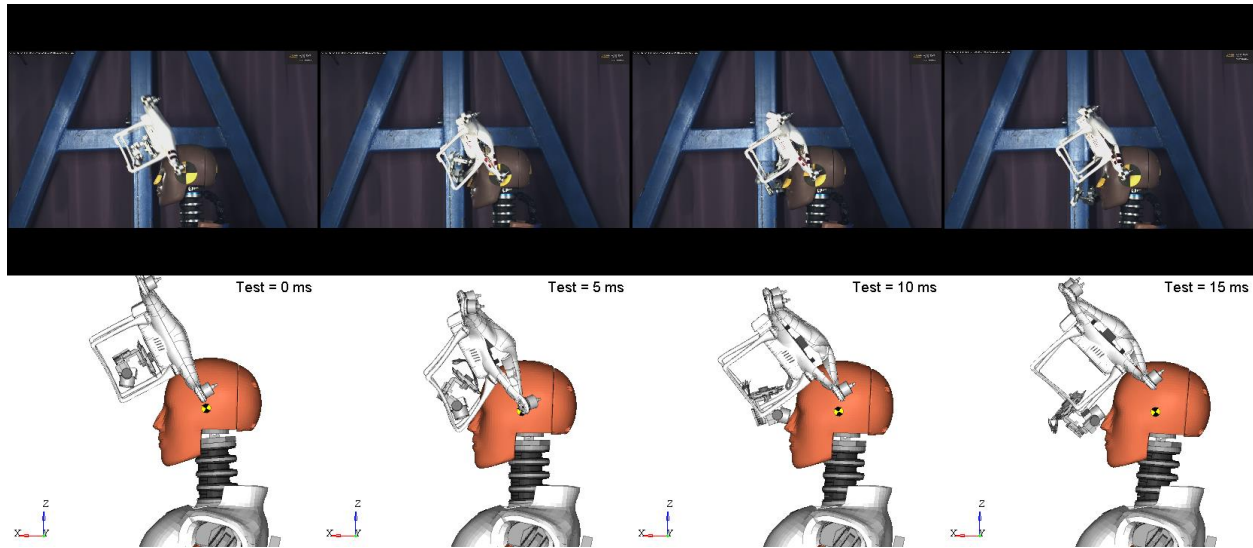


Figure 54. Test vs. simulation comparison of the reference Test 15 from Task A14 [45].

To replicate this impact condition, a similar ATD FEM available during this work was positioned in the same configuration and seated using the same rigid seat FEM. Figure 55 presents the final FEM with the ATD positioned on the rigid seat. Note that because it is highly unlikely that the 55lb. fixed-wing UAV operates around individuals, this sUAS was not considered for the impact analysis involving this target.

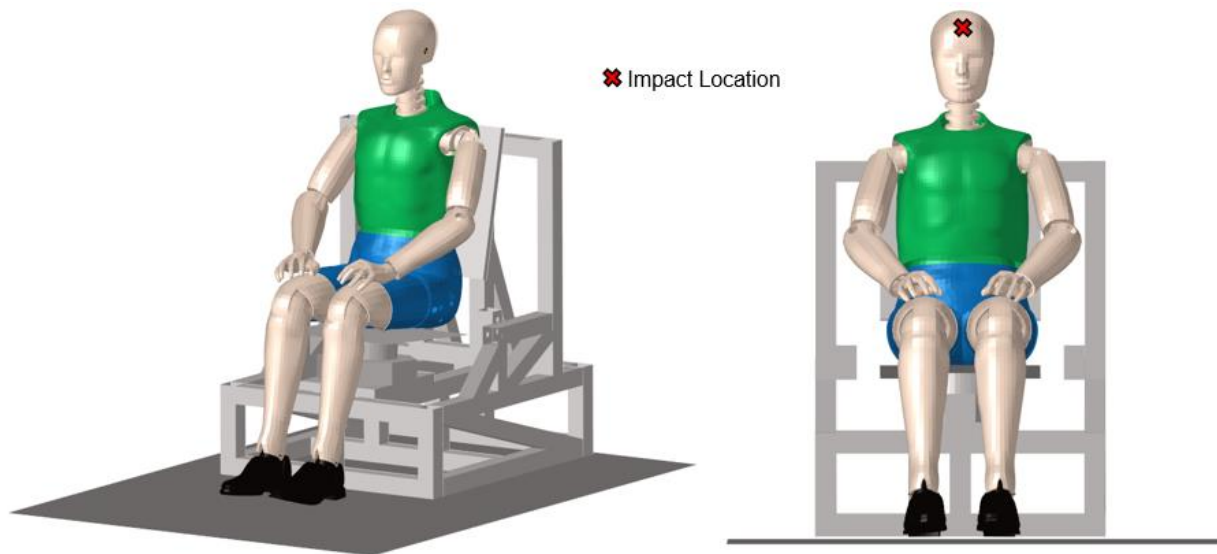


Figure 55. Operation over people – FEM and impact location.

5.2.3 Moving Vehicle

The moving vehicle impact scenario considers the collision of a sUAS with a representative sedan vehicle. NIAR had already internally developed a FEM of a vehicle with this architecture, which was selected as a target for the collision study defined in this work. The impact location is centered with a horizontal flight trajectory headed toward the driver's position. The study considers only the first impact with the multi-layer windshield. Therefore, the model simplifies several

components, such as lights, seats, and others. The target velocity was defined as 60mph, which is representative of the speed of a vehicle on a state highway in the United States. Figure 56 illustrates the isometric, front, and side view of the FEM.

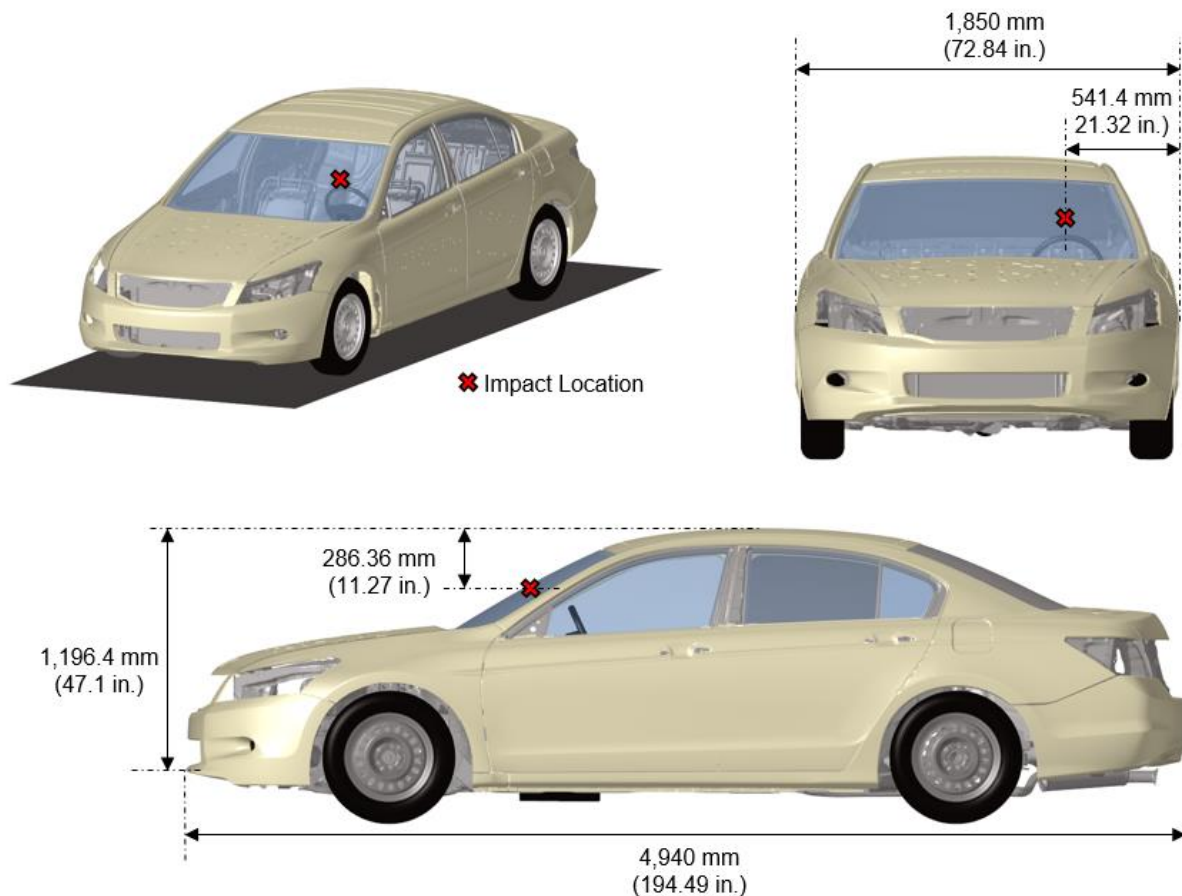


Figure 56. Moving Vehicle – FEM and impact location.

5.2.4 Other Critical Conditions

Wall Impact

The wall impact case considers the impact of a UAS on a building. A FEM was developed with the representative properties of a masonry wall to achieve the appropriate impact conditions. D’Altri, A. M., et al. [52] developed a detailed masonry panel FEM that considers the in-plane and out-of-plane mortar and brick properties. Additionally, they considered the failure mechanisms of the mortar-brick interface. In this work, the model does not consider the failure mechanisms of the panel. Therefore, the constituents were modeled using only the elastic properties. Table 29 presents the material properties used for each constituent.

Table 29. Brick and mortar material properties.

	Density [kg/m ³]	Young's Modulus [MPa]	Poisson's Ratio
Brick	2,000	16,700	0.15
Mortar	2,160	2,300	0.15

The dimensions of each brick are 204mm x 98mm x 50mm, replicating the size used in [52]. The mortar layer is 12.5 mm thick. Both components were modeled with 3D elements, using the criteria presented in Table 18 but changing the minimum and maximum allowed element size to 9mm and 15mm, respectively. Figure 57 illustrates the wall FEM. Note that the size of the model was adjusted to the dimensions of each UAS to reduce the computational cost.

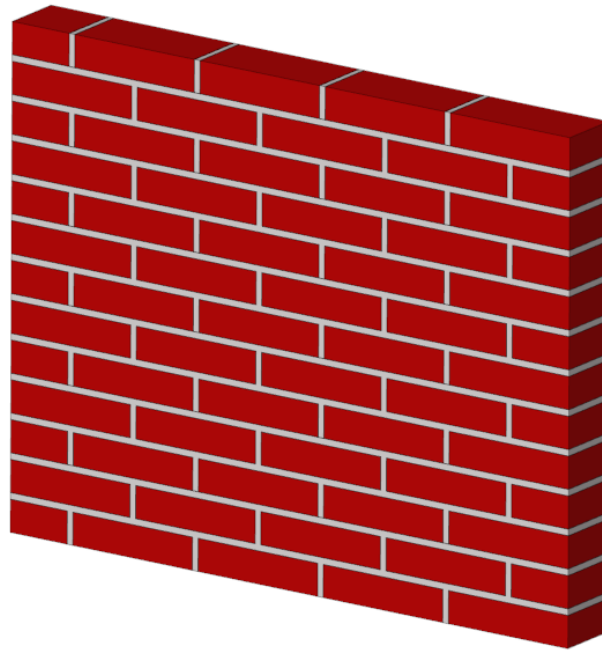


Figure 57. Masonry wall FEM.

Surface Impact

The surface impact analyses consider the crash scenario of a UAS with a representative ground surface due to a sudden shutoff or UAS malfunction. NIAR considered three different types of surfaces depending on the environment in which the UAS operates. These surfaces are water (representative of lakes and the sea), wet soil (representative of forests, mountains, or fields), and concrete (representative of urban environments).

Surface 1 – Water

The water volume was modeled with 3D elements, with an average element size of 30mm. To optimize computational efficiency, the option **DEFINE_ADAPTIVE_SOLID_TO_SPH* was activated. By using this option, the 3D Lagrangian elements are replaced by Smoothed Particle

Hydrodynamics (*SPH) elements during the analysis. This reduces the computational costs compared to utilizing SPH elements from the beginning of the analysis. A layer comprising multiple elements was maintained along the sides and bottom of the domain to ensure that the boundary constraints remained active during the analysis. The domain was modeled large enough to minimize edge effects (wave reflections) caused by having rigid boundaries.

The water was modeled using *MAT_NULL with a Murnaghan Equation of State (*EOS_MURNAGHAN). Table 30 contains the properties applied to the material card.

Table 30. *MAT_NULL water properties.

Density [kg/m ³]	Pressure Cutoff [MPa]	Dynamic Viscosity
1,000	-1x10 ⁻⁴	1x10 ⁻⁹

Equation (7) describes the Murnaghan equation of state. The constant γ was set to 7, following the recommendations in the LS-Dyna user's manual [41]. The constant k_0 was computed using the maximum expected fluid flow velocity for each analysis. The initial relative volume was set to 1. The hourglass control was also defined following the recommendations from the LS-Dyna user's manual [41].

$$p = k_0 \left[\left(\frac{\rho}{\rho_0} \right)^\gamma - 1 \right] \quad (7)$$

Figure 58 shows the Surface Water FEM. Note that the model's dimensions were modified for each analysis depending on the UAS FEM size to optimize the computational efficiency.

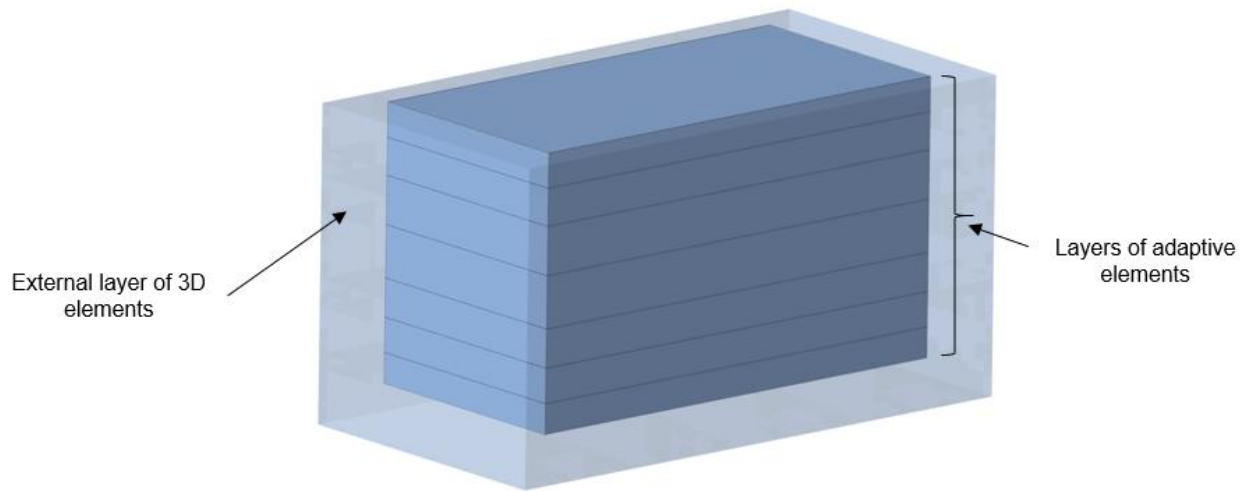


Figure 58. Surface Water FEM.

Surface 2 – Wet Soil

The soil domain was modeled using 3D elements with an average size of 30mm. Thomas, M. A., et al. [53] developed a constitutive model for Carson Sink soil during the wet season. The published report contains the input parameters to define the constitutive model in the LS-Dyna **MAT_005: SOIL_AND_FOAM*. Figure 59 presents the inputs defined in the material model 5. Additionally, an **ADD_EROSION* card was defined to erode elements with compressive strains greater than the last pressure-volume point defined in the material model (EPS10) to avoid numerical instabilities due to element distortion. Figure 60 illustrates the wet soil FEM. Note that the FEM dimensions were modified for each analysis depending on the UAS FEM size to optimize the computational efficiency.

	<u>Input</u>	<u>Value</u>	<u>Units</u>
Mass density	RO	0.000135	lb s ² /in ⁴
Shear modulus	G	500	psi
Bulk unloading modulus	K	12600	psi
Yield surface coefficient	A0	1.968	psi ²
Yield surface coefficient	A1	1.858	psi
Yield surface coefficient	A2	0.439	-
Pressure cutoff	PC	-1.0	psi

	<u>Input</u>	<u>Value</u>	<u>Input</u>	<u>Value</u>	<u>Units</u>
Pressure-volume point	EPS1	0	P1	0	psi
Pressure-volume point	EPS2	-0.007	P2	4.5	psi
Pressure-volume point	EPS3	-0.0102	P3	5.36	psi
Pressure-volume point	EPS4	-0.013	P4	6	psi
Pressure-volume point	EPS5	-0.019	P5	7	psi
Pressure-volume point	EPS6	-0.063	P6	12	psi
Pressure-volume point	EPS7	-0.125	P7	19.6	psi
Pressure-volume point	EPS8	-0.185	P8	32	psi
Pressure-volume point	EPS9	-0.22	P9	47	psi
Pressure-volume point	EPS10	-0.259	P10	67	psi

Figure 59. Material inputs for material model 5 [53].

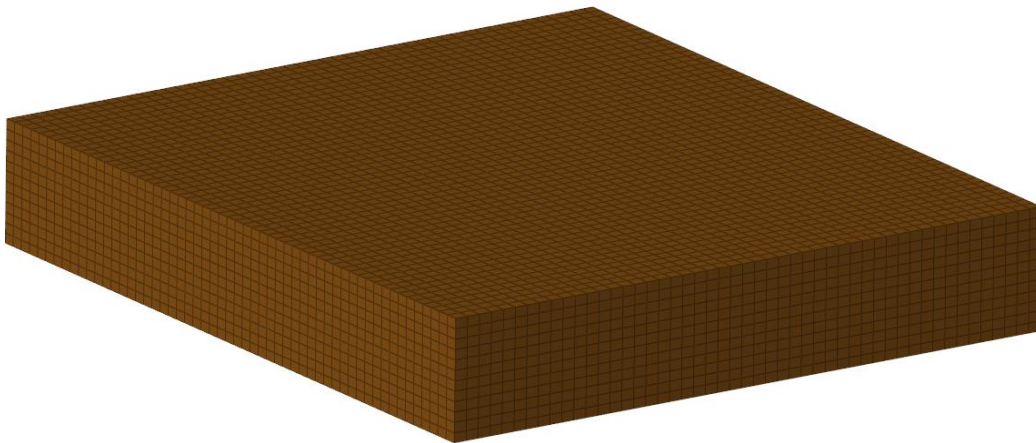


Figure 60. Surface Wet Soil FEM.

Surface 3 – Concrete

The concrete domain was modeled using 3D elements with an average size of 30mm and an elastic material with representative properties. Table 31 gathers the input properties for the elastic material model. Figure 61 presents the surface concrete FEM. Note that the model's dimensions were modified for each analysis depending on the UAS FEM size to optimize the computational efficiency.

Table 31. Concrete properties defined for the elastic material.

Density [kg/m³]	Young's Modulus [MPa]	Poisson's Ratio
2,400	35,000	0.24

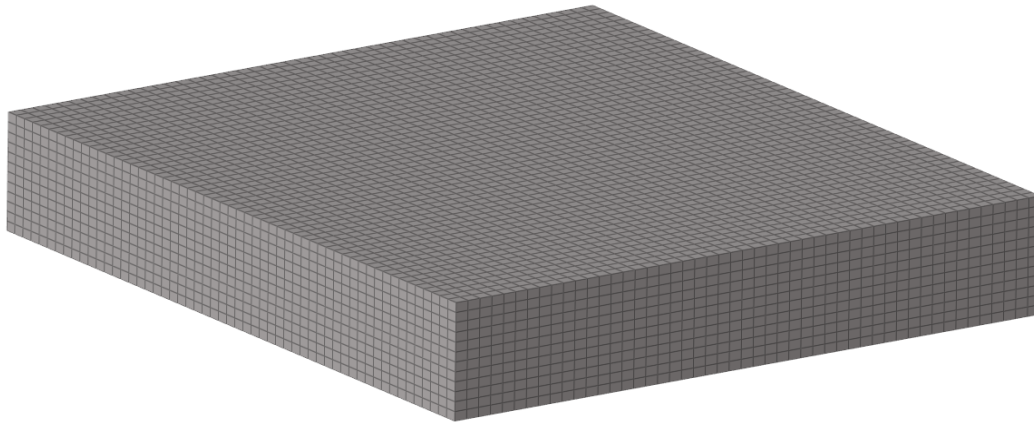


Figure 61. Surface Concrete FEM.

5.3 Impact Condition Definition

Section 5.1 presented the FEMs of the sUAS subjected to impact analysis. Section 5.2 defined the targets and the impact location for the analyses. To fully define the impact conditions, this section provides an explanation of the impact velocity and the criteria used to determine the initial orientation of the sUAS.

5.3.1 Impact Velocity

For all the cases involving aircraft structures, the cruise velocity was identified as the most critical condition based on the damage severity levels reported in previous research tasks. The General Aviation cruise velocity is 140knots [49]. The Rotorcraft cruise velocity is 150knots [47]. Note that the impact velocity was defined as the sum of the aircraft and sUAS cruise velocities. For the Business Jet and Commercial Transport cases, the Q2.7 and F55 were previously analyzed for impact velocities up to 350knots [51]. Therefore, for these cases, this work uses the same impact velocity (350knots) for the three sUAS. For the ATD impact analysis, the impact velocity from Test 15 [45] was used as a reference. The impact velocity for the Moving Vehicle analysis was determined by adding the sUAS cruise velocity to the vehicle's velocity (60mph).

For the building impact scenario, the sUAS were subjected to impact with the masonry wall at cruise velocity. For the surface impact analyses, the impact velocity was determined by computing the terminal velocity for each sUAS. Appendix B describes the process for determining the terminal velocity. Table 32 presents the impact velocity for all the analyses defined in this work.

Table 32. A55 crash analyses – Impact velocity.

Impact Case	F2.55 Impact Velocity [knots]	Q2.7 Impact Velocity [knots]	F55 Impact Velocity [knots]
G – Windshield	190	178.8	190
G – Wing	190	178.8	190
B – Vertical Stabilizer	350	350	350
B – Wing	350	350	350
C – Horizontal Stabilizer	350	350	350
C – Wing	350	350	350
R – Blade	200 + Blade Rotational Velocity	188.8 + Blade Rotational Velocity	200 + Blade Rotational Velocity
R – Front Cowling	200	188.8	200
ATD	31.1	31.1	31.1
Moving Vehicle	102.14	90.94	102.14
Wall	50	38.8	50
Surface Water	210.2	59.25	210.2
Surface Soil	210.2	59.25	210.2
Surface Concrete	210.2	59.25	210.2

5.3.2 Impact Conditions

As a result of several impact location and orientation sensitivity studies, the following impact conditions recommendations were developed during Task A3 [46]:

- To cause the most damage to the target, the UAS center of gravity should be aligned with the first point of contact at impact.
- The quadcopter model should be oriented to impact with one motor first.
- If impacting on leading-edge structures, the UAS should impact in between rib stations, facilitating the possibility of skin perforation and penetration inside the airframe.

These impact conditions were developed to predict the worst outcome during a crash scenario between a UAS and an aircraft. Since this work uses as a reference the crash scenarios developed during A3, A14, and A16, which already consider the previous recommendations, the analyses performed in this work also take advantage of these.

For the rest of the targets, the following impact conditions were assumed:

- The ATD impact analysis replicates the test conditions reported in Test 15 [45] for the UAS velocity and orientation.
- A horizontal flight trajectory was considered for the moving vehicle and wall impact cases.
- For the surface impact cases, the UAS orientation was chosen to minimize the drag coefficient, therefore maximizing the impact velocity (see Appendix B).

5.3.3 Load Case Name Convention

The broad spectrum of FE model combinations and parameters used in this work requires a code to identify the simulated impact conditions based on the UAS, aircraft type, target component, and

local impact positions. The impact conditions were coded using the following characters (A55-Bcij-DEF):

- B – Distinguishes target.
 - G → General Aviation
 - B → Business Jet
 - C → Commercial Transport
 - R → Rotorcraft
 - GC → Ground Collision (ATD Impact)
 - MV → Moving Vehicle
 - W → Wall
 - SW → Surface Water
 - SS → Surface Water
 - SC → Surface Concrete
- Cij – Distinguishes between UAS type and size:
 - Fixed-wing 2.55 lb. (F2.55)
 - Quadcopter 2.7 lb. (Q2.7)
 - Fixed-wing 55 lb. (F55)
- D – Distinguishes impact areas:
 - Wing (W)
 - Windshield – Cockpit I
 - Vertical stabilizer (V)
 - Horizontal stabilizer (H)
 - Blade (B)
 - Front CowliI(C)
 - ATD – Head (H)
 - Wall, Surface Water, Surface Soil and Surface Concrete do not have a specific impact area (x)
- E – Distinguishes impact location (1,2 or 3)
 - Wall, Surface Water, Surface Soil, and Surface Concrete do not have a specific impact location (x)
- F – Distinguishes between velocity categories associated with the aircraft.
 - The cruise velocity was selected for the General Aviation, Business Jet, Commercial Transport, and Rotorcraft cases.
 - The Wall, Surface Water, Surface Soil, and Surface Concrete are static targets (S)

Note that the A55 prefix was used to differentiate the code from the analysis using the same projectile, target, and impact conditions in previous research programs.

5.3.4 Simulation Matrix

Table 33 through

Table 35 present the simulation matrix for the sUAS FEMs considered in this study.

Table 33. F2.55 FEM simulation matrix.

Target	Impact Location	Impact Velocity	Analysis Code
G – Windshield	1	Cruise	A55-GF2.55-C1C
G – Wing	1	Cruise	A55-GF2.55-W1C
B – Vertical Stabilizer	3	Cruise	A55-BF2.55-V3C
B – Wing	1	Cruise	A55-BF2.55-W1C
C – Horizontal Stabilizer	1	Cruise	A55-CF2.55-H1C
C – Wing	1	Cruise	A55-CF2.55-W1C
R – Front Cowling	1	Cruise	A55-RF2.55-C1C
R – Blade	1	Cruise	A55-RF2.55-B1C
Operation Over People - Head	1	Static	A55-GCF2.55-H1S
Wall	N/A	Static	A55-WF2.55-xxS
Moving Vehicle - Windshield	1	Cruise	A55-MVF2.55-C1C
Surface Water	N/A	Static	A55-SWF2.55-xxS
Surface Soil	N/A	Static	A55-SSF2.55-xxS
Surface Concrete	N/A	Static	A55-SCF2.55-xxS

Table 34. Q2.7 FEM simulation matrix.

Target	Impact Location	Impact Velocity	Analysis Code
G – Windshield	1	Cruise	A55-GQ2.7-C1C
G – Wing	1	Cruise	A55-GQ2.7-W1C
B – Vertical Stabilizer	3	Cruise	A55-BQ2.7-V3C
B – Wing	1	Cruise	A55-BQ2.7-W1C
C – Horizontal Stabilizer	1	Cruise	A55-CQ2.7-H1C
C – Wing	1	Cruise	A55-CQ2.7-W1C
R – Front Cowling	1	Cruise	A55-RQ2.7-C1C
R – Blade	1	Cruise	A55-RQ2.7-B1C
Operation Over People - Head	1	Static	A55-GCQ2.7-H1S
Wall	N/A	Static	A55-WQ2.7-xxS
Moving Vehicle - Windshield	1	Cruise	A55-MVQ2.7-C1C
Surface Water	N/A	Static	A55-SWQ2.7-xxS
Surface Soil	N/A	Static	A55-SSQ2.7-xxS
Surface Concrete	N/A	Static	A55-SCQ2.7-xxS

Table 35. F55 FEM simulation matrix.

Target	Impact Location	Impact Velocity	Analysis Code
G – Windshield	1	Cruise	A55-GF55-C1C
G – Wing	1	Cruise	A55-GF55-W1C
B – Vertical Stabilizer	3	Cruise	A55-BF55-V3C
B – Wing	1	Cruise	A55-BF55-W1C
C – Horizontal Stabilizer	1	Cruise	A55-CF55-H1C
C – Wing	1	Cruise	A55-CF55-W1C
R – Front Cowling	1	Cruise	A55-RF55-C1C
R – Blade	1	Cruise	A55-RF55-B1C
Wall	N/A	Static	A55-WF55-xxS
Moving Vehicle - Windshield	1	Cruise	A55-MVF55-C1C
Surface Water	N/A	Static	A55-SWF55-xxS
Surface Soil	N/A	Static	A55-SSF55-xxS
Surface Concrete	N/A	Static	A55-SCF55-xxS

5.4 Analysis Results

This section presents the FEM details and the analysis results for the full-scale impact simulations. To enhance clarity and conciseness, a representative case for each sUAS was selected to introduce the numerical aspects used in these analyses as well as the type of data extracted and analyzed. Appendix C contains the FEM details and results for the remaining analyses.

5.4.1 A55-RF2.55-C1C

The front cowling was impacted with the 2.55lb. fixed-wing model at the chimney. The location was selected based on the most severe impact condition from [47] for the 2.7lb. quadcopter model. The 2.55lb. fixed-wing was oriented so that the center of mass was aligned with the impact location. A fixed boundary condition on the lower skin of the cowling assembly was defined to constrain the complete model. Therefore, the resultant relative velocity of the aircraft and the sUAS was applied to the sUAS body through an **INITIAL_VELOCITY* card. Note that the rotor assembly spun at an angular velocity of 298.5rpm to model the representative conditions in the case of secondary impacts with this structure. A gravity load was prescribed during the simulation to act on the UAS and the cowling. The contact and control parameters were defined using NIAR's experience for an impact with this type of composite structure. Table 36 presents the element count for this analysis, which indicates the total number of individual finite elements used to discretize the model. Figure 62 depicts the FEM setup.

Table 36. A55-RF2.55-C1C element count.

Type of Element	1D	2D	3D
Element Count	4,240	827,205	865,170

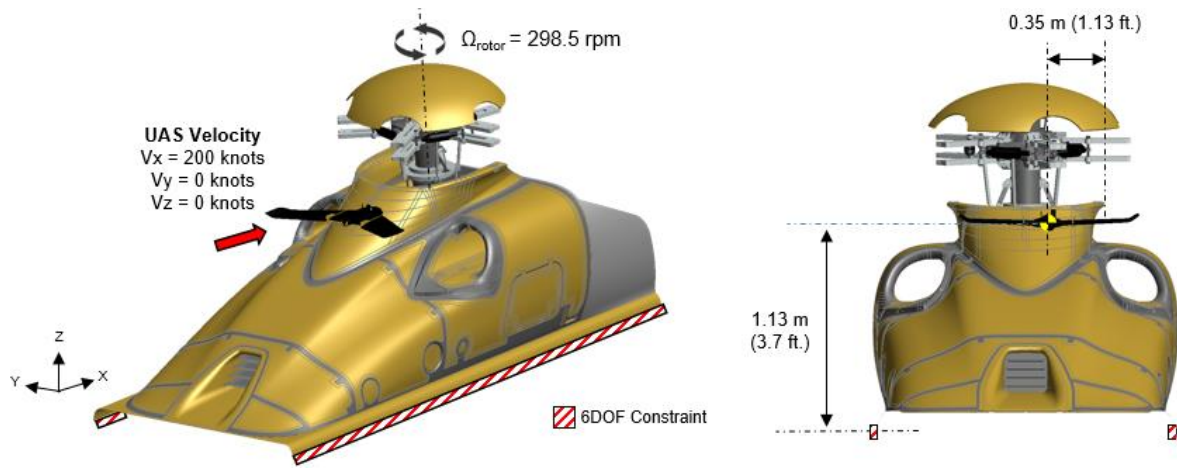


Figure 62. A55-RF2.55-C1C FEM setup.

Figure 63 shows the evolution of the simulation through the isometric and close-up views of three instances of the simulation. The sUAS was deflected towards the rotor shaft assembly after colliding with the cowling surface. The UAS foam and camera served as protection for the VS.

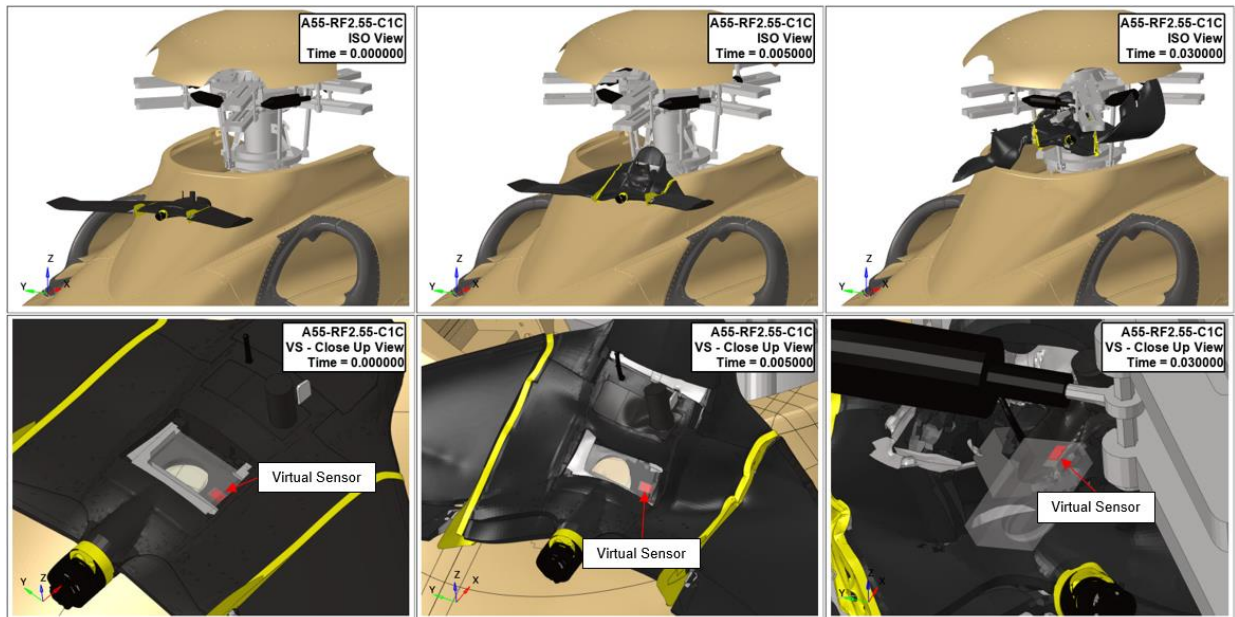


Figure 63. Isometric (top) and close-up (bottom) views of the A55-RF2.55-C1C impact event at $t=0s$ (left), $t=0.005s$ (middle) and $t=0.03s$ (right).

The loads and accelerations at the Virtual Sensor were collected during the simulation using the methodology presented in Section 4. Figure 64 presents the loads in the X, Y, and Z directions at the cross-sections defined in the VS FEM. These results are representative of the expected values at the VS location on this particular sUAS. A filter was applied to the loads using the same parameters defined during the LVI validation exercise (see Section 4.3). However, the low mass and small size of the VS as well as the impact velocity, intensify the high-frequency vibrations

caused by the contact interaction with the camera. Figure 65 shows the impulse computed using the resultant force.

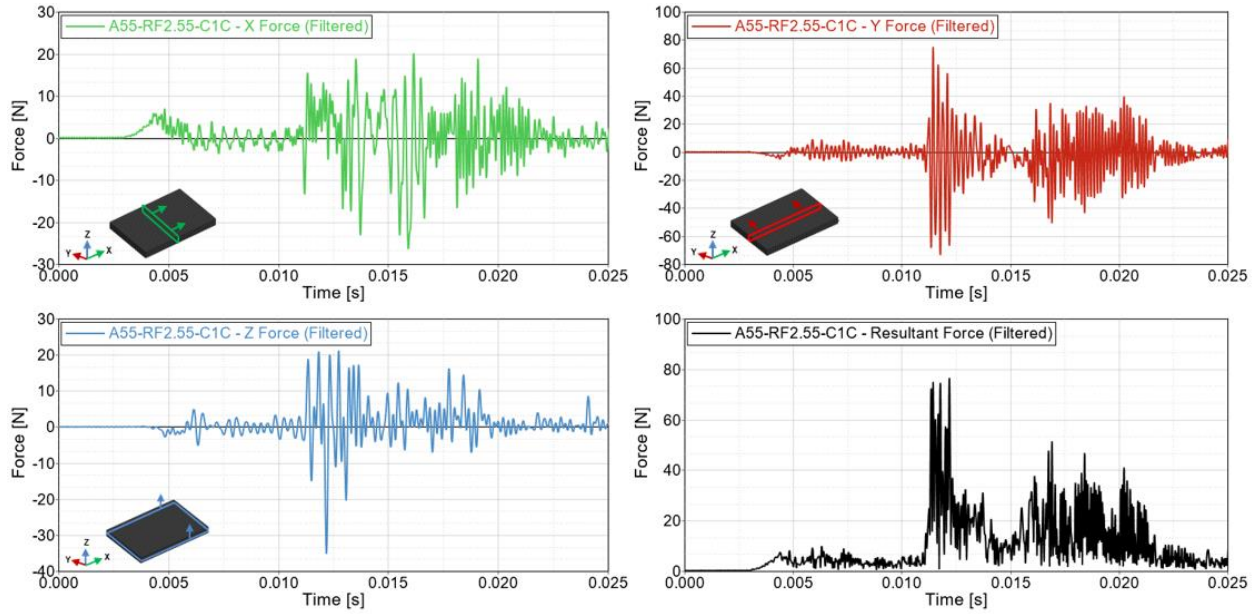


Figure 64. A55-RF2.55-C1C – Virtual Sensor loads.

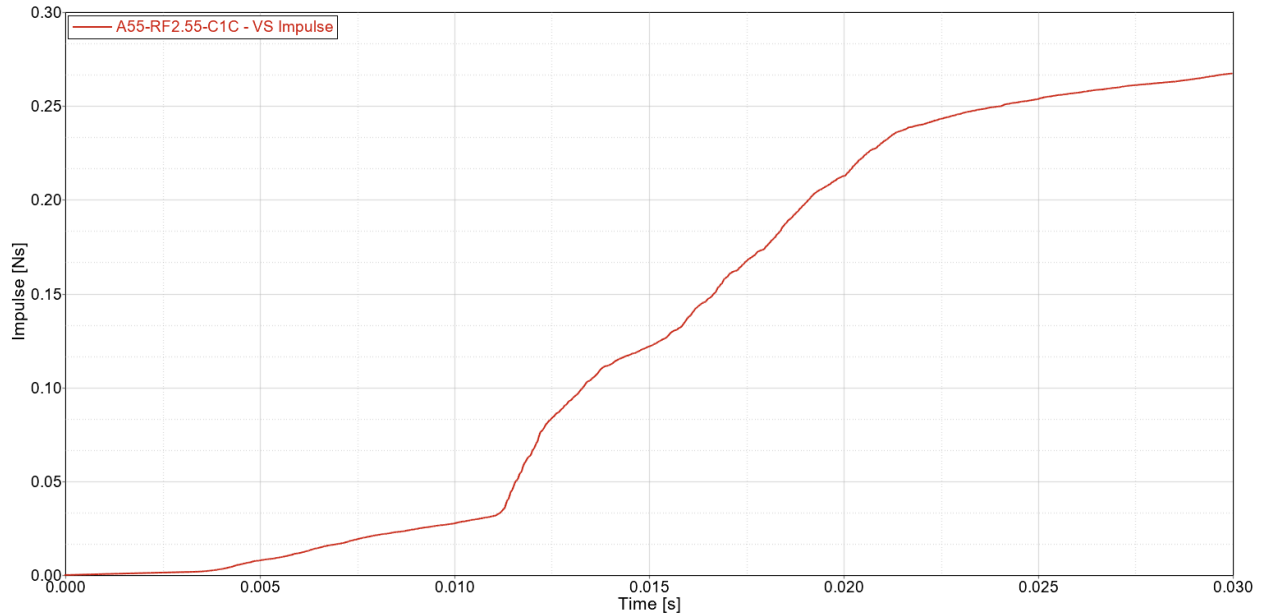


Figure 65. A55-RF2.55-C1C – Impulse transferred to the VS.

Figure 66 illustrates the non-filtered rigid body acceleration (left) and the maximum effective acceleration with its corresponding time window (right). It should be noted that two different time windows were analyzed. The 0.5ms time window corresponds to the pulse duration specified in JESD22-B104C Condition B. The second time window was defined based on the most severe secondary impact observed during the analysis. Note the effect of the averaging function on the high-magnitude and high-frequency oscillations caused by the numerical instabilities.

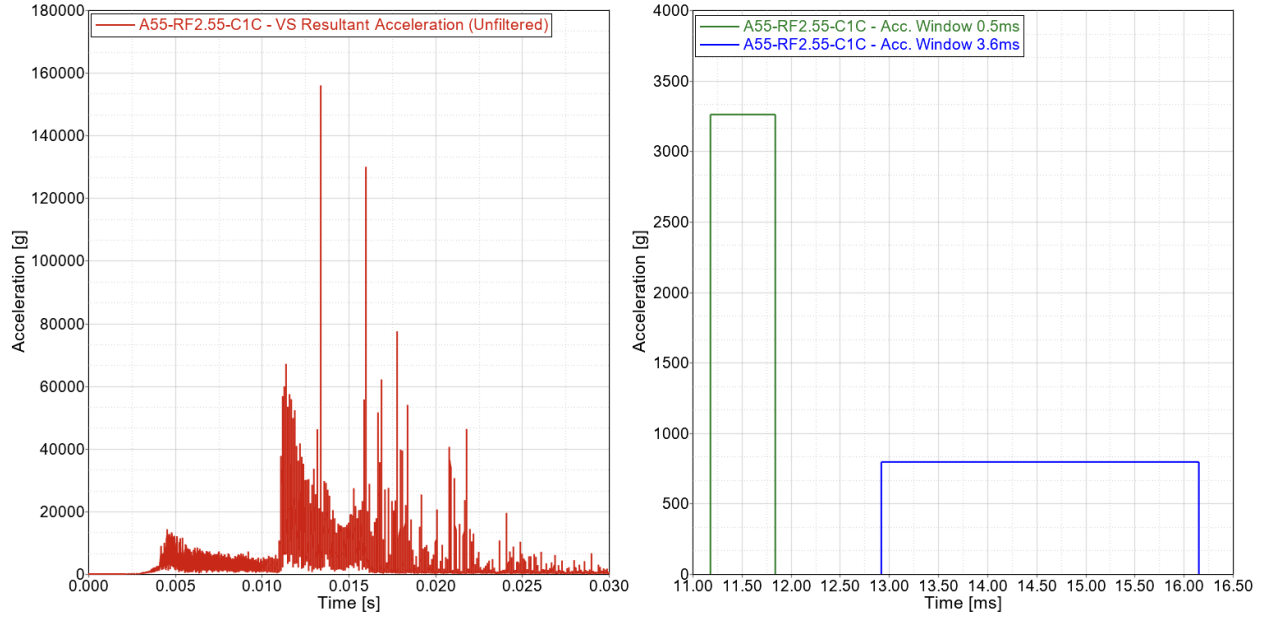


Figure 66. A55-RF2.55-C1C – Unfiltered Virtual Sensor rigid body acceleration (left) and maximum average acceleration for a 0.5ms and 3.6ms time window (right).

5.4.2 A55-MVQ2.7-C1C

The Moving Vehicle FEM was subjected to impact with the 2.7lb. quadcopter model at the front windshield. The impact location was found by aligning the gravity center of the sUAS with the driver's position for a horizontal flight condition. A fixed boundary condition constrains the bottom rigid plane and the wheels. Therefore, the resultant relative velocity of the vehicle and the sUAS was applied to the sUAS body through an **INITIAL_VELOCITY* card. Additionally, a gravity load was prescribed during the simulation to act on the sUAS and the vehicle.

Note that the analysis only considers the first impact with the windshield, and hence the interior of the car was simplified to reduce the computational cost. The contact and control parameters were defined using NIAR's experience for an impact with this type of multilayer structure. Table 37 presents the element count for this analysis, which indicates the total number of individual finite elements used to discretize the model. Figure 67 depicts the FEM setup.

Table 37. A55-MVQ2.7-C1C element count.

Type of Element	1D	2D	3D
Element Count	753	2,500,441	248,816

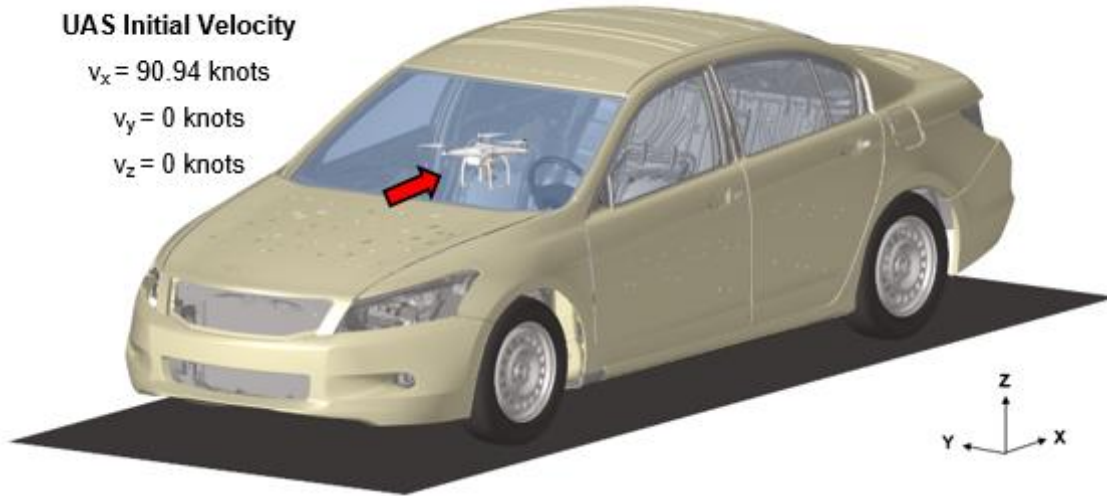


Figure 67. A55-MVQ2.7-C1C FEM setup.

Figure 68 shows the evolution of the simulation through the isometric and close-up views of three instances of the simulation. The sUAS penetrated through the windshield and entered the cockpit space. However, most of the energy was absorbed by the windshield, the UAS carcass, and the PCB, protecting the VS, which remained attached to the board without being damaged.

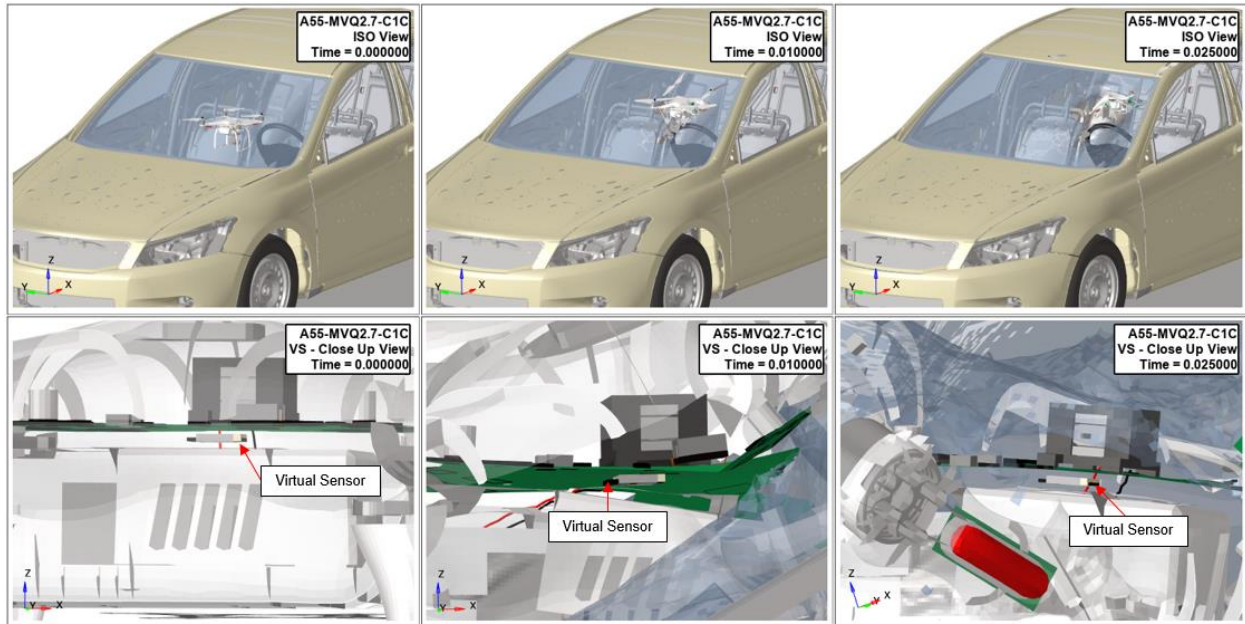


Figure 68. Isometric (top) and close-up (bottom) views of the A55-MVQ2.7-C1C impact event at $t=0s$ (left), $t=0.01s$ (middle) and $t=0.025s$ (right).

Figure 69 presents the loads in the X, Y, and Z directions at the cross-sections defined in the VS FEM. These loads are representative of the expected values at the FDR for this sUAS. A filter was applied to the loads using the same parameters defined during the LVI validation exercise (see Section 4.3). Figure 70 shows the impulse computed using the resultant force.

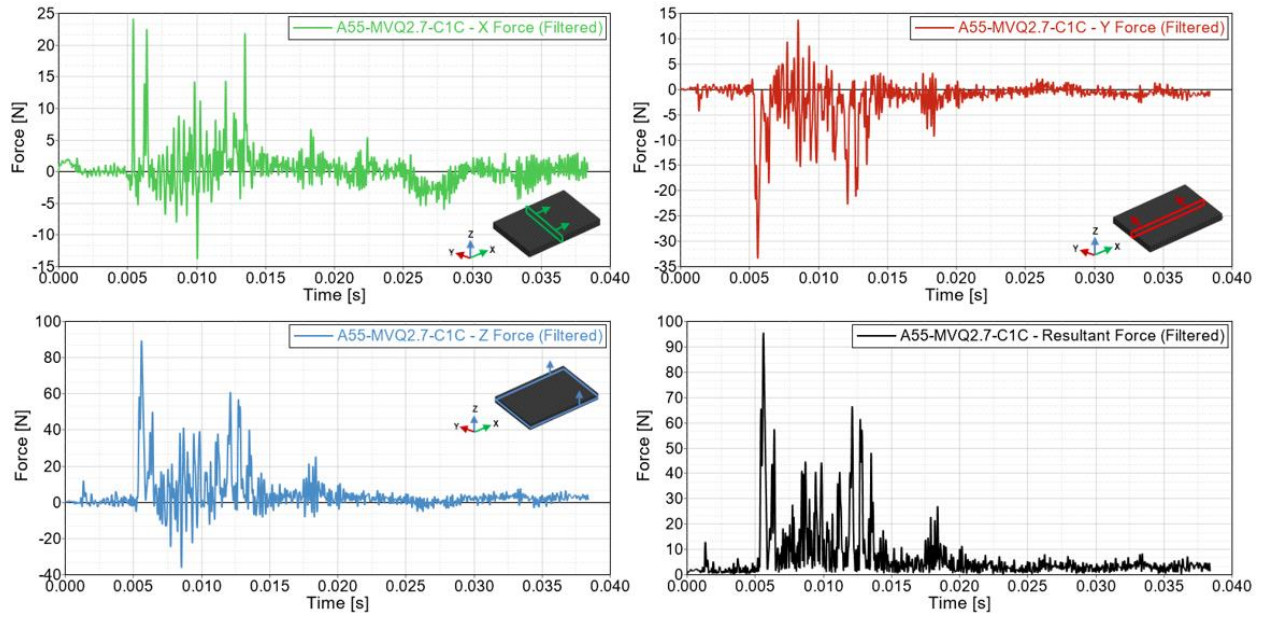


Figure 69. A55-MVQ2.7-C1C – Virtual Sensor loads.

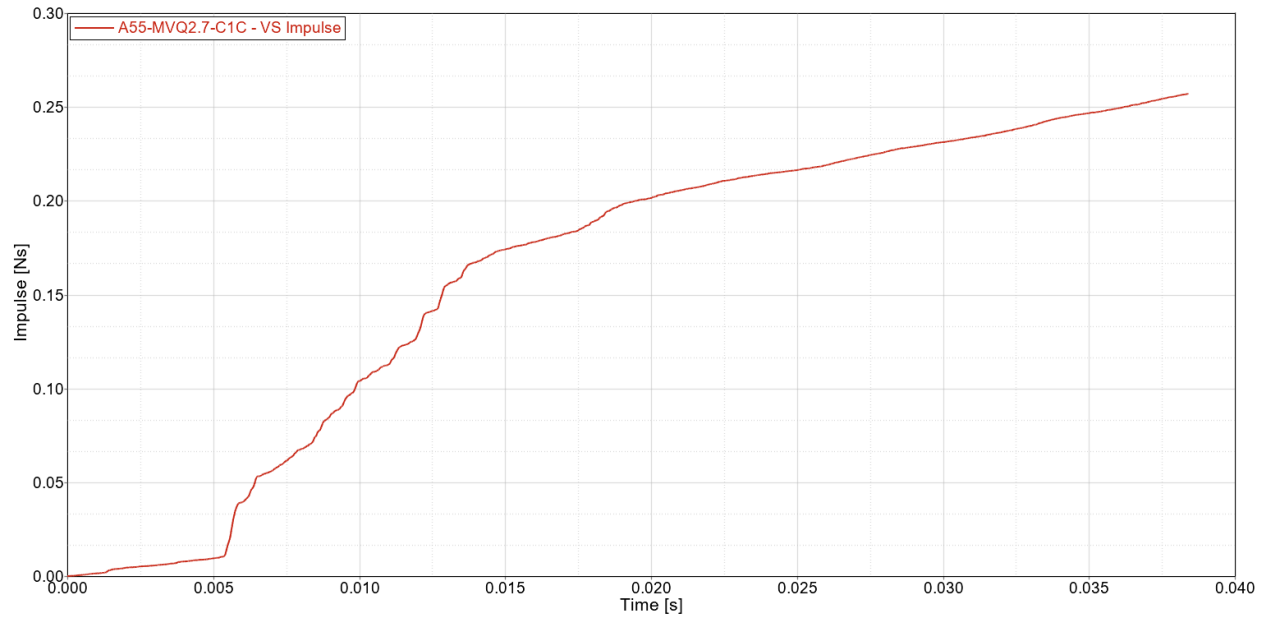


Figure 70. A55-MVQ2.7-C1C – Impulse transferred to the VS.

Figure 71 illustrates the non-filtered rigid body acceleration (left) and the maximum effective acceleration with its corresponding time window (right). Again, two different time windows were analyzed. The 0.5ms time window corresponds to the pulse duration specified in JESD22-B104C Condition B. The second time window was defined based on the most severe secondary impact observed during the analysis. Note the effect of the averaging function on the high-magnitude and high-frequency oscillations caused by the numerical instabilities.

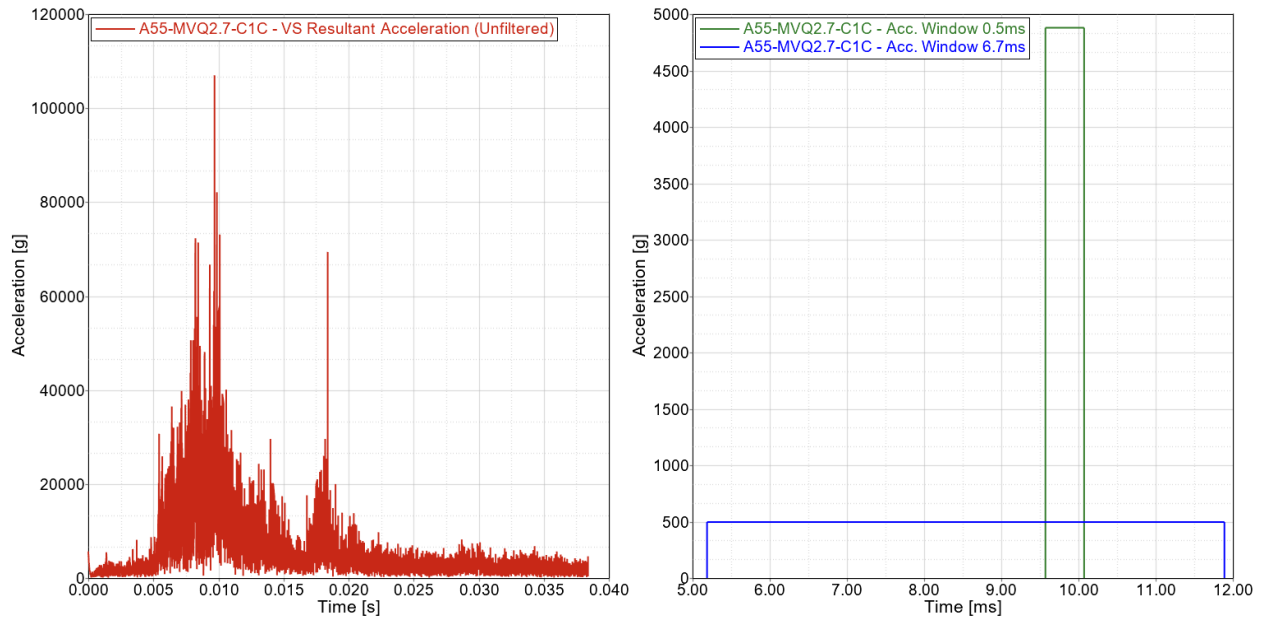


Figure 71. A55-MVQ2.7-C1C – Unfiltered Virtual Sensor rigid body acceleration (left) and maximum average acceleration for a 0.5ms and 6.7ms time window (right).

5.4.3 A55-GF55-C1C

The General Aviation FEM was subjected to impact with the 55lb. fixed-wing model at the windshield. The UAS was positioned in front of the propeller to study the possibility of going through it without being deflected. The CG of the UAS was aligned with the windshield impact location. There were no constraints applied to the aircraft and the UAS. Additionally, a gravity load was prescribed during the simulation to act on the sUAS and the aircraft.

Note that the analysis only considers the first impact with the windshield, and hence the interior of the aircraft was simplified to reduce the computational cost. The contact and control parameters were defined using NIAR’s experience for an impact with this type of metallic and acrylic structure. Table 38 presents the total number of individual finite elements used to discretize the model for this analysis. Figure 72 depicts the FEM setup.

Table 38. A55-GF55-C1C element count.

Type of Element	1D	2D	3D
Element Count	29,418	4,473,193	2,247,796

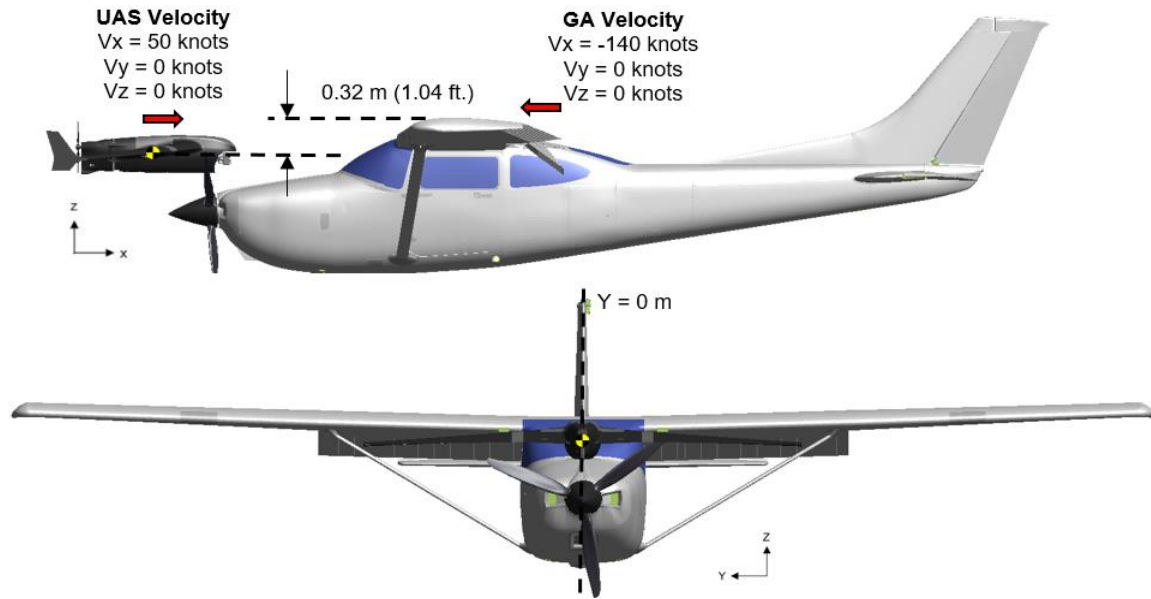


Figure 72. A55-GF55-C1C FEM setup.

Figure 73 shows the evolution of the simulation through the isometric and close-up views of three instances of the simulation. The propeller sliced the UAS without deflecting it. Therefore, all the UAS mass went through the propeller and impacted the windshield, which failed after the secondary impact. The windshield, the UAS composite skin, and the internal components absorbed most of the energy. However, a secondary impact caused some permanent deformation to the socket metallic shell, and a few elements of the VS eroded. The VS's eroding mechanism was defined to represent similar plastic housings. Note that the VS was considered not valid if more than 10% of the mass was eroded or if the secondary impacts caused the VS to split into several parts. However, in this case, none of these conditions were observed; hence, the loads and accelerations were still representative. Figure 74 presents the damage observed to the VS assembly after the impact event.

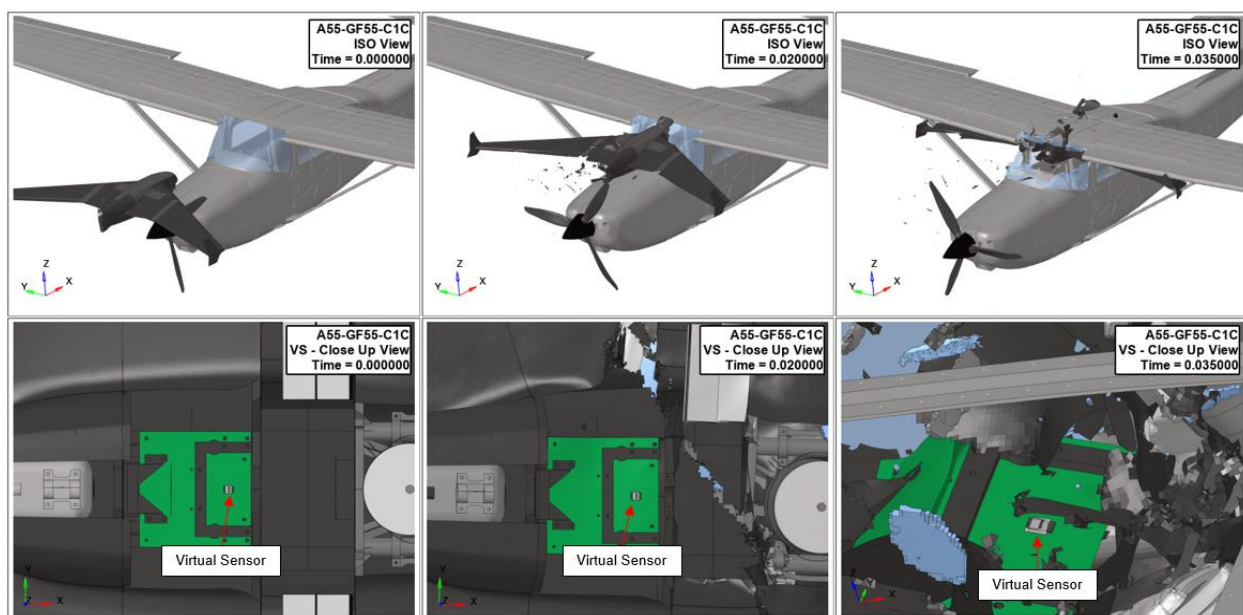


Figure 73. Isometric (top) and close-up (bottom) views of the A55-GF55-C1C impact event at $t=0s$ (left), $t=0.02s$ (middle) and $t=0.035s$ (right).

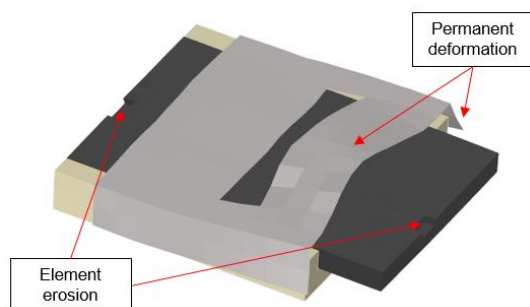


Figure 74. A55-GF55-C1C – VS damage at the end of the analysis.

Figure 75 presents the loads in the X, Y, and Z directions at the cross-sections defined in the VS FEM. These loads are representative of the expected values at the FDR for this sUAS. A filter was applied to the loads using the same parameters defined during the LVI validation exercise (see Section 4.3). Again, the most significant loads are caused by secondary impacts and indentations to the VS. Figure 76 shows the impulse computed using the resultant force.

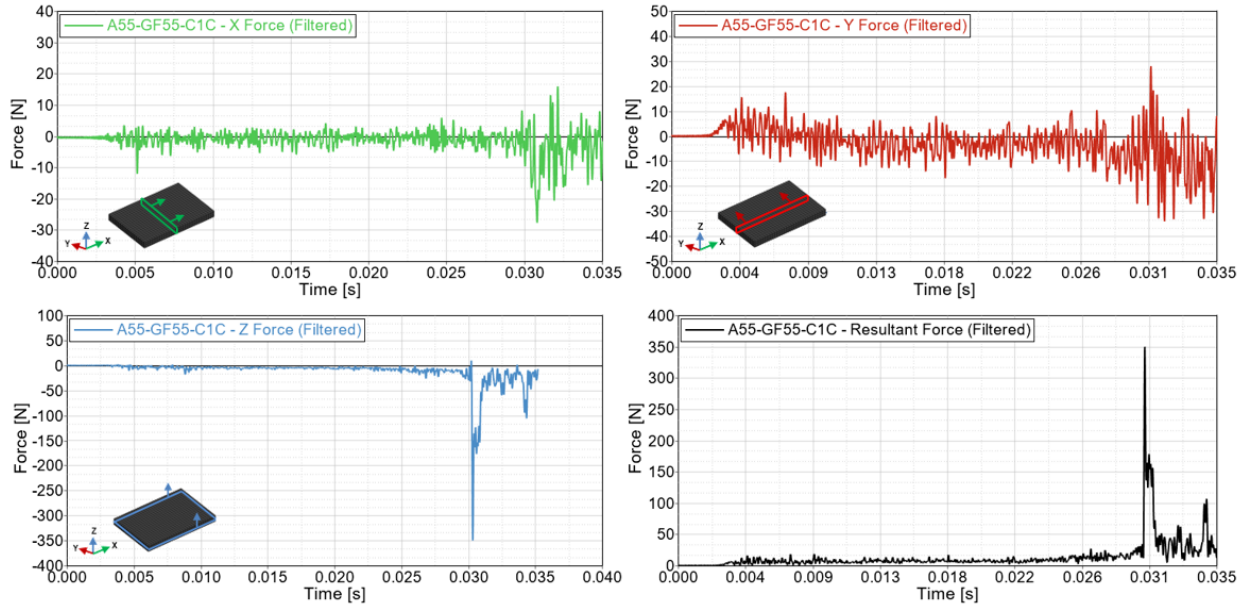


Figure 75. A55-GF55-C1C – Virtual Sensor loads.

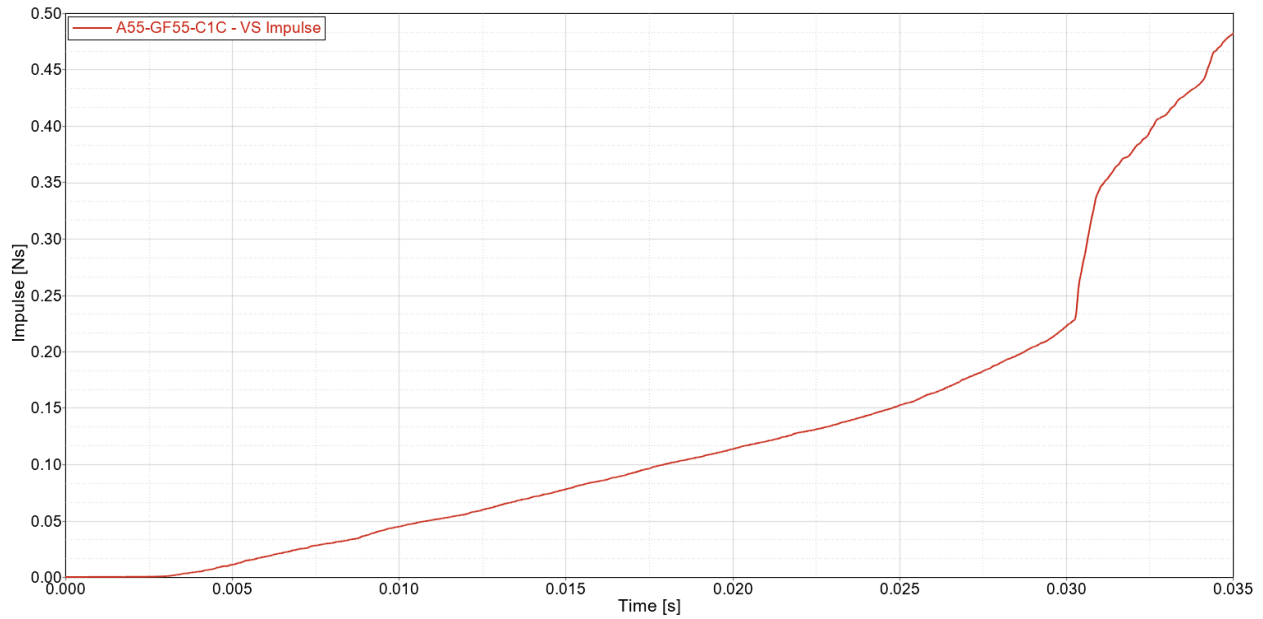


Figure 76. A55-GF55-C1C – Impulse transferred to the VS.

Figure 77 illustrates the non-filtered rigid body acceleration (left) and the maximum effective acceleration with its corresponding time window (right). Two different time windows were analyzed. The 0.5ms time window corresponds to the pulse duration specified in JESD22-B104C Condition B. The second time window was defined based on the most severe secondary impact observed during the analysis. Note the effect of the averaging function on the high-magnitude and high-frequency oscillations caused by the numerical instabilities.

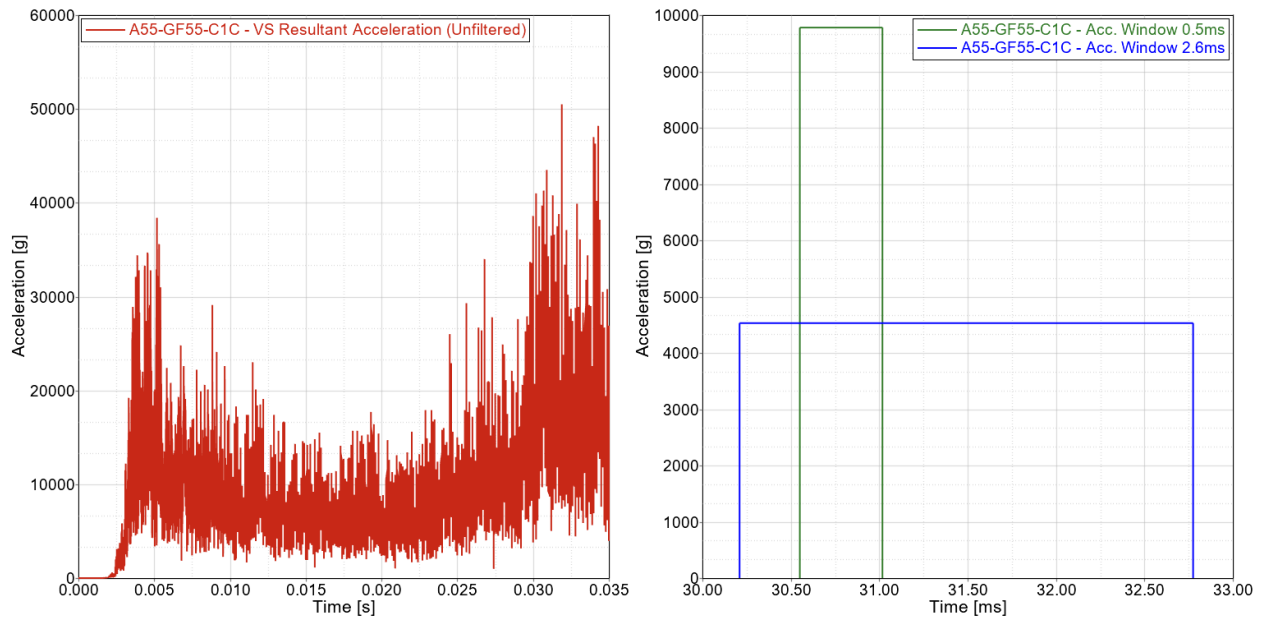


Figure 77. A55-GF55-C1C – Unfiltered Virtual Sensor rigid body acceleration (left) and maximum average acceleration for a 0.5ms and 2.6ms time window (right).

5.5 Results Summary

This section provides a comprehensive summary of the load and acceleration results derived from the analyses conducted in this study. The results are categorized based on the UAS type, and for each UAS, the corresponding range of loads and accelerations is presented. Table 39 through Table 41 present the results for the F2.55, Q2.7, and F55 impact analyses. For the F2.55 UAS, the maximum observed load was 500.2N for the rotorcraft blade impact, and the minimum load was 0.75N for the ground collision impact. The maximum acceleration was 4,850g for the commercial transport wing impact, and the lowest acceleration was 154g for the ground collision impact. For the Q2.7 UAS, the maximum observed load was 910.43N for the rotorcraft blade impact, and the minimum load was 20.65N for the wet soil surface impact. The maximum acceleration was 9,800g for the commercial transport wing impact, and the lowest acceleration was 2,010g for the wall impact. For the F55 UAS, the maximum observed load was 559.6N for the commercial transport horizontal stabilizer impact, and the minimum load was 37.7N for the wall impact. The maximum acceleration was 17,500g for the rotorcraft front cowling impact, and the lowest acceleration was 3,880g for the business jet vertical stabilizer impact.

Table 39. Virtual Sensor load and acceleration results for the F2.55 impact analyses.

Case ID	Max. Acceleration [g]	Window Time [ms]	Max. Force in VS [N]
A55-RF2.55-C1C	3,260 (0.5ms) / 795 (3.3ms)	13.3-13.8 / 12.9-16.2	76.53
A55-RF2.55-B1C	543 (0.5ms) / 5,260 (0.2ms)	0.5-1 / 0.85-1.05	500.2
A55-GF2.55-C1C	1,540 (0.5ms) / 356 (8.3ms)	19.8-20.3 / 19-27.3	30.4
A55-GF2.55-W1C	3,200 (0.5ms) / 1,260 (1ms)	4.7-5.2 / 5.6-6.6	135.7
A55-BF2.55-V3C	777 (0.5ms) / 321.5 (1.2ms)	1.5-2.0 / 3.4-4.6	102.8
A55-BF2.55-W1C	1,270 (0.5ms) / 755 (1.2ms)	3.9-4.4 / 3.8-5	211.1
A55-CF2.55-W1C	4,850 (0.5ms) / 1,140 (1ms)	1.4-1.9 / 1.4-2.4	216.8
A55-CF2.55-H1C	1,079 (0.5ms) / 622.8 (1.7ms)	4.3-4.8 / 1.4-3.1	278
A55-GCF2.55-H1S	154 (0.5ms) / 65.5 (10.4ms)	10.1-10.6 / 4.7-15.1	0.75
A55-WF2.55-xxS	664 (0.5ms) / 149 (5.3ms)	9.3-9.8 / 8.1-13.3	11.5
A55-SWF2.55-xxS	4,650 (0.5ms) / 3,060 (1ms)	3.4-3.9 / 2.7-3.7	89.2
A55-SSF2.55-xxS	3,440 (0.5ms) / 1,610 (1.3ms)	2.5-3 / 2.2-3.5	69.33
A55-SCF2.55-xxS	237 (0.5ms) / 13.8 (1ms)	1.5-1.9 / 0.9-1.9	92.2
A55-MVF2.55-W1C	809 (0.5ms) / 470 (2.1ms)	19.19.5 / 18.5-20.6	34.8

Table 40. Virtual Sensor load and acceleration results for the Q2.7 impact analyses.

Case ID	Max. Acceleration [g]	Window Time [ms]	Max. Force in VS [N]
A55-RQ2.7-C2C	3,310 (0.5ms) / 1,590 (2.2ms)	5.1-5.6 / 3.6-5.8	697.42
A55-RQ2.7-B1C	3,070 (0.5ms) / 16,600 (0.2ms)	0.7-1.2 / 0.7-0.9	910.43
A55-GQ2.7-C1C	3,870 (0.5ms) / 863 (4ms)	4.5-5 / 10.3-14.3	63.49
A55-GQ2.7-W1C	5,870 (0.5ms) / 2,020 (2ms)	5.15-5.65 / 3.85-5.85	154.15
A55-BQ2.7-V3C	9,090 (0.5ms) / 1,590 (2.1ms)	5.7-6.2 / 1.3-3.4	268.53
A55-BQ2.7-W1C	4,650 (0.5ms) / 2,860 (0.9ms)	1.5-2.0 / 1.4-2.3	870
A55-CQ2.7-W1C	9,800 (0.5ms) / 1,200 (1ms)	0.8-1.3 / 0.3-1.3	784.4
A55-CQ2.7-H1C	6,790 (0.5ms) / 985 (2.2ms)	1.3-1.8 / 3.0-5.2	183.16
A55-GCQ2.7-H1S	2,670 (0.5ms) / 457 (3.4ms)	3.3-3.8 / 2.2-5.6	20.8
A55-WQ2.7-xxS	2,010 (0.5ms) / 613 (4.9ms)	5.3-5.8 / 4.9-9.8	52.91
A55-SWQ2.7-xxS	2,060 (0.5ms) / 731 (4.7ms)	3.9-4.4 / 3.5-8.2	20.67
A55-SSQ2.7-xxS	3,060 (0.5ms) / 823 (4.4ms)	3.1-3.6 / 2.9-7.3	20.65
A55-SCQ2.7-xxS	4,700 (0.5ms) / 790 (2.7ms)	3.4-3.9 / 2.7-5.4	45.54
A55-MVQ2.7-W1C	4,880 (0.5ms) / 496 (6.7ms)	9.6-10.1 / 5.2-11.9	94.14

Table 41. Virtual Sensor load and acceleration results for the F55 impact analyses.

Case ID	Max. Acceleration [g]	Window Time [ms]	Max. Force in VS [N]
A55-RF55-C1C	17,500 (0.5ms) / 8,570 (2ms)	14.7-15.2 / 13.6-15.6	99
A55-RF55-B1C	4,573 (0.5ms) / 8,000 (0.2ms)	2.9-3.4 / 3.6-3.8	171.2
A55-GF55-C1C	9,780 (0.5ms) / 4,530 (2.6ms)	30.6-31.1 / 30.2-32.8	349.8
A55-GF55-W1C	9,580 (0.5ms) / 5,620 (2.2ms)	11.5-12.1 / 11.4-13.6	117.3
A55-BF55-V3C	3,880 (0.5ms) / 3,240 (0.8ms)	4.7-5.2 / 4.7-5.5	236.3
A55-BF55-W1C	13,300 (0.5ms) / 9,210 (0.8ms)	5.6-6.2 / 5.4-6.2	282.1
A55-CF55-W1C	5,900 (0.5ms) / 2,800 (1.1ms)	4-4.5 / 3.8-4.9	215.9
A55-CF55-H1C	9,010 (0.5ms) / 5,920 (1.2ms)	6.5-7 / 5.1-6.3	559.6
A55-WF55-xxS	8,320 (0.5ms) / 2,630 (5.4ms)	28.4-28.9 / 24.6-30	37.7
A55-SWF55-xxS	5,350 (0.5ms) / 3,830 (1.1ms)	7.8-8.3 / 7.8-8.9	181.4
A55-SSF55-xxS	15,500 (0.5ms) / 13,300 (1.1ms)	9.2-9.7 / 8.8-9.9	287.4
A55-SCF55-xxS	11,100 (0.5ms) / 9,020 (1.3ms)	6.2-6.7 / 6.2-7.5	353.8
A55-MVF55-W1C	5,468 (0.5ms) / 1,549 (2.7ms)	28.3-28.8 / 27.4-30.1	78.97

Figure 78 and Figure 79 compare the load and acceleration levels for all the impact analyses, categorizing them based on the UAS type. There is no clear trend in the load and acceleration results. However, the impact conditions were not identical for all the analyses. Furthermore, the UAS architecture and the VS assembly vary depending on the UAS. Nevertheless, it was possible to extract valuable information by observing the load and acceleration values.

The Q2.7 VS observed the highest loads for most of the analyses. It is important to remark that the impact velocity of the Q2.7 sUAS was slightly lower for some cases and significantly lower (72%) for the surface impact cases (see Table 32). In most of the analyses, the Q2.7 polycarbonate carcass failed, exposing the PCB and the battery. Because of this, the VS was subjected to secondary impacts, which are more critical in terms of loads and accelerations. Additionally, in this UAS the PCB is attached to the battery carcass. In some of the impact scenarios, it was observed that following the failure of the UAS carcass, the PCB experienced compression between the battery and the target. This impact event is critical for the VS, given the high impact velocity and the high mass of the battery compared to the PCB. Figure 80 illustrates the PCB secondary impact with the battery and the rotorcraft shaft.

For the F55 UAS, most of the energy is absorbed by the composite skin and the internal components located at the front. However, the high aligned mass of this UAS combined with the high impact velocity and the conservative nature of the failure associated with the composite skin and frames led to significant load levels in the VS. Again, the VS for this UAS is attached to the PCB and unprotected from secondary impacts, which are critical in terms of load and accelerations. For this UAS, the VS was located approximately and the center of its length. Compared to a quadcopter architecture, more components are located closer to the impact surface, which translates into a lower load transferred to the VS. However, the high stiffness-to-mass ratio of the

composite materials in this UAS intensifies the vibrations caused by the impact. Therefore, this UAS observed the highest acceleration levels.

The VS of the F2.55 UAS observed the lowest accelerations and loads. The foam structure absorbs most of the impact energy. Additionally, this structure bends under compression and stops the high-mass components from aligning in the impact direction. Furthermore, the VS in this UAS was protected by the simplified camera. The loads collected at the VS are conservative since the rigid connectors rigidify the connection region, leading to zero energy-absorption. In some of the analyses, this caused the failure of the elements attached to the rigid connectors, which resulted in the VS detached from the camera. The VS resultant acceleration was under the 1,500g limit specified in JESD22-B104C for 8 of 14 analyses. This indicates that foam structures are suitable for reducing the shock vibrations caused by the secondary impacts.

Note that only in 8 of 41 analyses did the maximum VS resultant acceleration not exceed the 1,500g limit. This suggests that the time window used for micro SD FDRs (0.5ms) may be very conservative or that a higher limit should be considered for this type of aircraft.

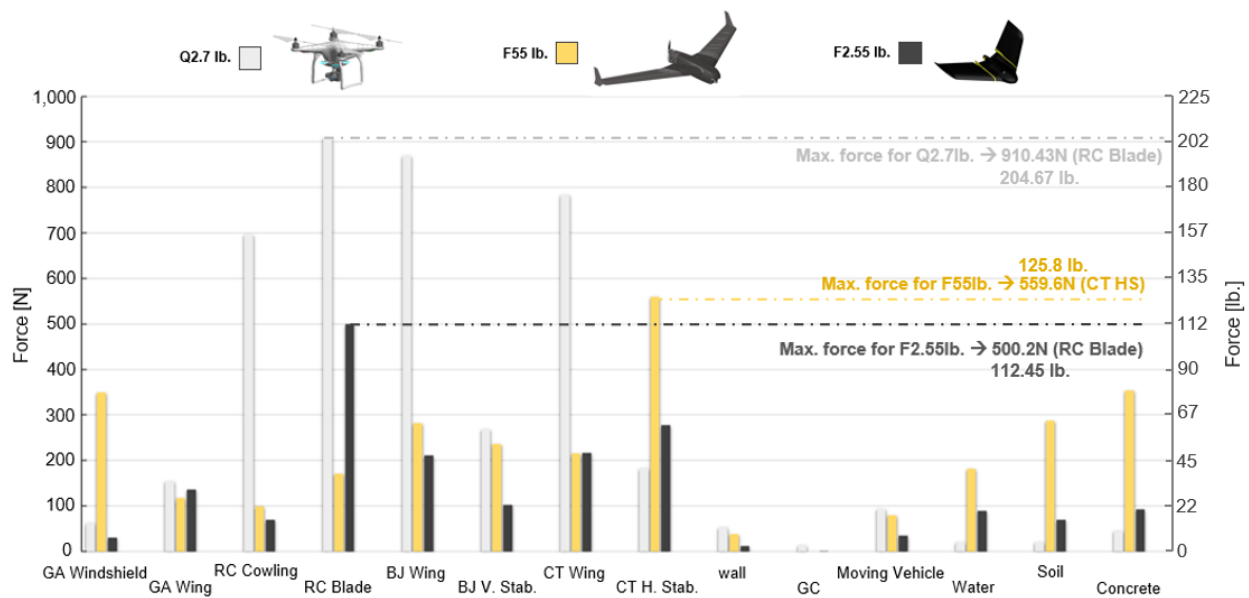


Figure 78. Virtual Sensor load results categorized by UAS type.

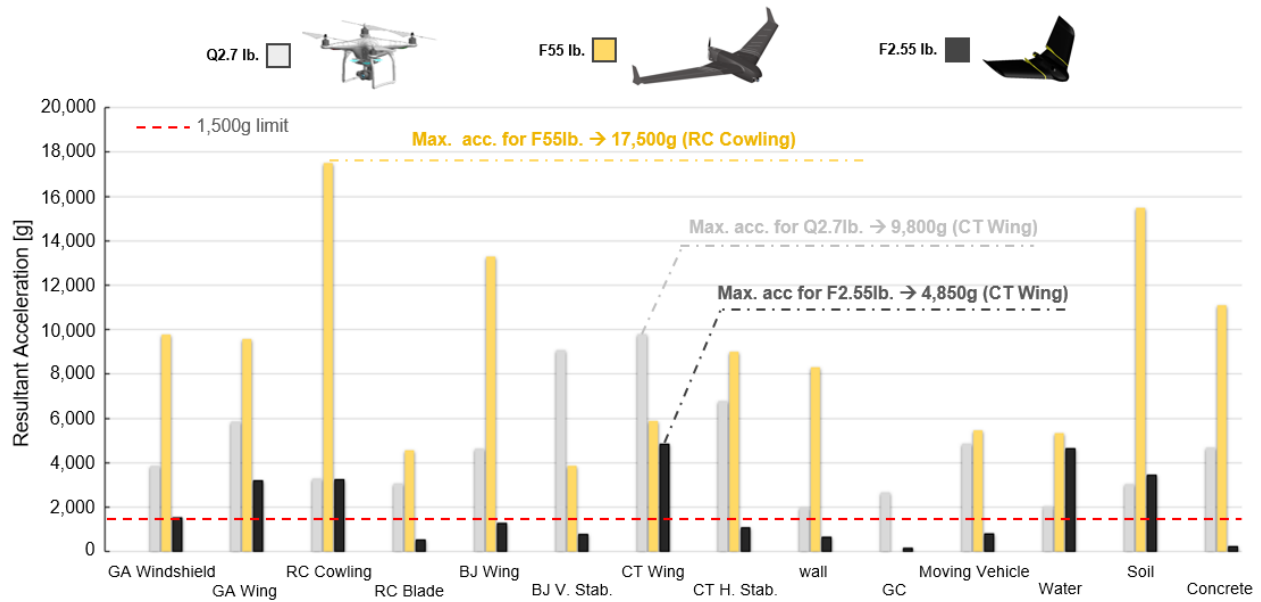


Figure 79. Virtual Sensor acceleration results categorized by UAS type.

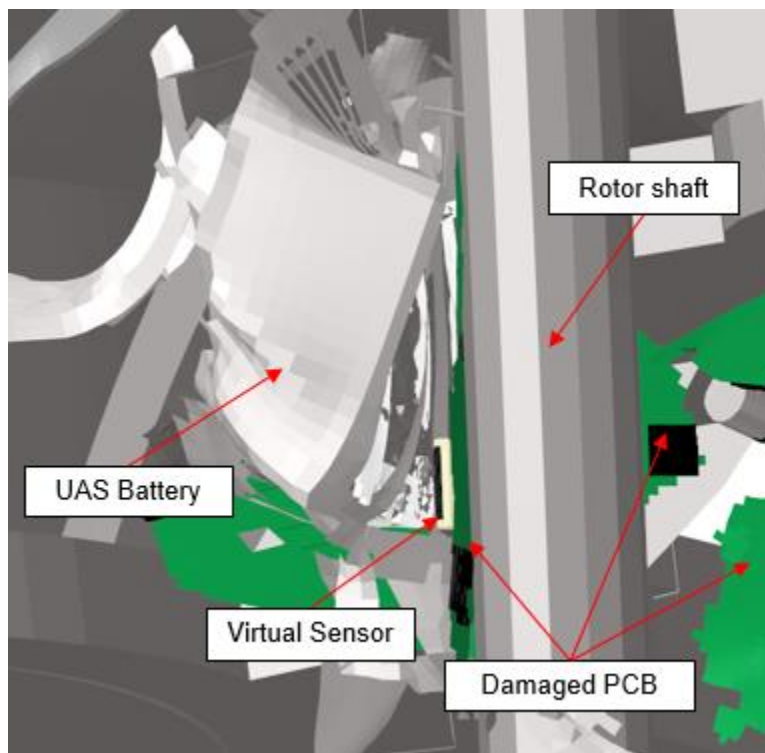


Figure 80. Compression of the PCB and Virtual Sensor by the battery for the Q2.7 sUAS.

6. CONCLUSIONS

The crash survivability requirements for FDRs have undergone continuous adaptation since the introduction of the first crash-protected unit. The current standards are the result of extensive research and feedback from accident investigations. Although the fast-growing number of UAS operations have increased the number of incidents involving these types of aircraft, the lack of data for these events has led to an existing gap between the standards for traditional and lightweight flight recording systems. While documents like EUROCAE ED-155 have addressed some of these gaps for lightweight FDRs, it remains uncertain if these requirements are applicable to sUAS.

In the present task, the most common devices to store flight data in sUAS were reviewed. It was observed that most of the current sUAS brands use micro SD cards as the preferred technology to store the data. NIAR has evaluated the mechanical performance of two different types of micro SD cards for static compression, penetration resistance, and low-intensity fire loading conditions. Additionally, NIAR has studied crash-scenarios involving sUAS by utilizing advanced numerical models developed during previous ASSURE programs. The cutting-edge numerical methodologies to analyze similar devices were reviewed and applied in several preliminary simulations of electronic board drop tests. It was found that simplifying the chips in the numerical models by using the smeared properties is a powerful methodology to predict the transient response of the electronic boards without incurring a high computational cost. Additional methodologies to define the appropriate damping and post-processing settings were developed and verified through the LVI validation exercise of a DJI Phantom III PCB.

NIAR modified three sUAS finite element models (Quadcopter 2.7lb., Fixed-wing 2.55lb., and Fixed-wing 55lb.) by including a representative model of a sUAS FDR (Virtual Sensor). These models have been included in several crash analyses involving the sUAS and a variety of targets, such as aircraft structures, pedestrians, vehicles, buildings, and ground surfaces. The targets were selected to consider most of the possible crash-scenarios for the type of sUAS considered in this work. Considering the type of metrics defined in the mechanical standards for crash survivable FDRs, the loads in every direction, the resultant acceleration, and the impulse transferred to the VS were extracted from the analyses.

Based on the results from the 41 impact scenarios and the mechanical tests performed during the present effort, the following conclusions were extracted:

- The analyzed micro SD specimens remained readable after static crush testing in the load range between 70-2,785lb. (311.38-12,388.3N) and after a penetrating load with a 3/8" spherical indenter up to 30lb. (133.45N). The lower load range for the penetration resistance tests shows the structural limitations of these devices under dynamic loading conditions. On the numerical side, the maximum loads observed for the F2.55, Q2.7, and F55 sUAS were 500.2N (112.45lb.), 910.43N (204.67lb.), and 559.6N (125.8lb.), respectively. These predicted loads occur during a shorter period of time (0.5-3ms) than the analyzed penetration loads. The duration of these loads hinders the use of traditional mechanical tests such as the ones utilized in this work. Additionally, the affected area in the simulations differ from case to case and it cannot be associated to a specific indenter geometry. However, these values can be used as a reference for comparison with the failure loads obtained in the penetration resistance tests and the loads specified in the standards. The most similar condition described in the FDR mechanical standards is the penetration resistance. The latest versions of TSO-C123 [4] and TSO-C124 [5] specify an impact with

a 500lb. (2224.11N) weight dropped from a height of 10 feet. The ED-155 does not require penetration resistance for fixed recorders; for deployable recorders, it requires the equivalent of an impact that simulates a landing velocity of 25m/s (80ft/s) onto a hard surface. The maximum load observed at the VS exceeds the minimum failure load of 35lb. obtained in the penetration resistance tests for 21 out of 41 analyses. This indicates that the flight data could be lost in more than 50% of the impact scenarios analyzed in this work. However, it is uncertain whether the penetration resistance loads outlined in TSO-C123 [4], TSO-C124 [5] and ED-155 accurately reflect those observed during a sUAS crash scenario. Therefore, consideration of new criteria specific to these aircraft may be necessary. In that case, the loads obtained during this work should serve as a guideline for the development of qualification tests.

- The maximum average accelerations observed for the F2.55, Q2.7, and F55 sUAS for a time window of 0.5ms were 4,850g, 9,800g, and 17,500g, respectively. It was observed that the recording devices used in sUAS are not required to comply with any mechanical standard. However, two of the most common commercially available brands (SanDisk and ATP) test these devices for a shock acceleration profile with a magnitude of 1,500g and a duration of 0.5ms. It is important to remark that only in 8 out of the 41 analyzed crash scenarios the maximum average acceleration level did not exceed this 1,500g level. The technical documentation of these devices does not specify if a failure occurs for shock magnitudes higher than this value. However, the acceleration values obtained from the simulations suggest that a crash-protection is essential to achieve a high probability of survival for the shock magnitudes expected in the analyzed crash conditions.
- Note that in this work, the FDR models replicated the mechanical behavior of the current sUAS recording devices. These devices are not crash-protected. Therefore, the loads and accelerations obtained from the numerical analyses should be considered critical when designing a lightweight crash-protection for sUAS FDRs.
- The highest loads were observed for the Q2.7lb. sUAS, which is a quadcopter architecture. The polycarbonate carcass failed in most of the simulations, leading to an unprotected FDR, which was then subjected to secondary impacts causing high loads and accelerations. The highest accelerations were observed for the F55lb. sUAS, which is a fully composite fixed-wing architecture. The composite skin and frames absorbed most of the impact energy by failing, which resulted in high-magnitude vibrations. The lowest loads and accelerations were observed for the F2.55 lb., a foam-based fixed-wing architecture. The foam body absorbed most of the impact energy in all the cases and redirected the high-mass components stopping them from aligning with the impact trajectory. Additionally, for this sUAS, the VS was protected by the camera. This shows that the sUAS architecture and its construction materials affect the loads and accelerations observed at the FDR.
- The maximum temperature at which the micro SD cards were tested was 200°C. The specimens remained readable for all the tests.

6.1 Future Research

The following topics could be addressed in future studies for sUAS FDRs:

1. Expand the numerical simulation matrix to study the VS location's influence on the loads and accelerations.

2. Design a lightweight housing able to withstand the critical conditions obtained during the present work. Note that depending on the sUAS type and operation, the housing should offer protection for other hazardous conditions not analyzed during this work, such as water/fluid immersion, low and high temperature, and hydrostatic pressure.
3. Perform numerical analyses, including a detailed finite element model of a prototype crash-protected FDR into the crash simulations developed under this task. Optimize the material use and the design based on the simulation results. It is recommended that the crash-protected FDR is valid for any sUAS architecture.
4. Develop dynamic mechanical tests similar to the ones developed in [44] to understand the effect of the shock duration and magnitude and support the numerical analyses to find the conditions that best represent an actual crash scenario involving a sUAS.
5. Use the results of the dynamic experimental test to build more robust FEMs of an FDR for a sUAS. Additionally, use the experimental results to calibrate the post-processing filters for loading conditions representative of a crash scenario.
6. Consider a broader temperature range along with soak times for the low-intensity fire tests.

7. REFERENCES

- [1] Higgins, J. and Branscomb, K., “Literature Review for ASSURE A55 – Identify Flight Recorder Requirements for Unmanned Aircraft Systems (UAS) Integration into the National Airspace System (NAS)”, Federal Aviation Administration, Report A11L.UAS.101_A55, 2022.
- [2] H. Thompson, M., “A vision of future crash survivable recording systems”, Allied Signal, Redmond, WA 98073.
- [3] Bailey, T., “Flight Data Recorders: Built to Survive”, The Aircraft Electronics Association – Avionics News, January 2006, 38-47.
- [4] Federal Aviation Administration. (December 19, 2013). Technical Standard Order: Cockpit Voice Recorder Equipment.
- [5] Federal Aviation Administration. (April 10, 2007). Technical Standard Order: Flight Data Recorder Systems.
- [6] EUROCAE, ED-112A: Minimum Operational Performance Specification for Crash Protected Airborne Recorder Systems, 2013.
- [7] EUROCAE, ED-155: Minimum Operational Performance Specification for Lightweight Flight Recording Systems, 2009.
- [8] <https://www.dji.com/>
- [9] <https://www.intel.com/content/www/us/en/homepage.html>
- [10] <https://us.yuneec.com/>
- [11] <https://www.kittyhawk.aero/>
- [12] <https://www.parrot.com/us/drones>
- [13] <https://www.rcgeeks.co.uk/blogs/news/dji-mavic-2-expert-review-hands-pro-zoom>
- [14] <https://www.mmagram.top/ProductDetail.aspx?iid=356135298&pr=87.88>
- [15] Intel Falcon 8+ - User’s Manual.
- [16] <https://www.hensoldt.net/products/avionics/sferirec-lcr100/>
- [17] <https://www.uavnavigation.com/products/peripherals/flight-data-recorder>
- [18] ETSO-2C197 A1 (https://www.easa.europa.eu/download/etso/ETSO-2C197_A1.pdf)
- [19] JEDEC JESD22-B104C (<https://www.jedec.org/standards-documents/docs/jesd-22-b104c>)
- [20] MIL-STD 883-2-2002.3 (<http://scipp.ucsc.edu/groups/fermi/electronics/mil-std-883.pdf>)
- [21] EN60529 (<https://www.en-standard.eu/search/?q=EN60529>)
- [22] IEC 605:1989 (<https://webstore.iec.ch/publication/2452>)
- [23] <https://www.westerndigital.com/products/memory-cards/sandisk-extreme-uhs-i-microsd#SDSQXAV-1T00-GN6MA>
- [24] <https://www.atpinc.com/products/industrial-microsd-usd-cards>

- [25] Lall, P., “Computational Methods and High-Speed Imaging Methodologies for Transient-Shock Reliability of Electronics”, International Conference on Thermal, Mechanical and Multi-Physics Simulation Experiments in Microelectronics and Micro-Systems (EuroSime), 2007, 1-13.
- [26] Zhu, L. and Marcinkiewicz, W., “Drop Reliability Analysis of CSP Packages at Board and Product Levels Through Modeling Approaches”, IEEE Transactions on Components and Packaging Technologies, 2005, 28(3), 449-456.
- [27] Meng, J. et al., “Drop qualification of MEMS components in handheld electronics at extremely high acceleration”, 13th InterSociety Conference on Thermal and Thermomechanical Phenomena in Electronic Systems, 2012, 1020-1027.
- [28] Agwai, A., et al., “Damage prediction for electronic package drop test using finite element method and peridynamic theory”, Electronic Components and Technology Conference, 2009, 565-569.
- [29] Pradeep, L., et al., “Models for Reliability of Fine-Pitch BGAs and CSPs in Shock and Drop Impact”, IEEE Transactions on Components and Packaging Technologies, 2006, 29 (3), 464-474.
- [30] Lall, P., et al., “Design envelopes and optical feature extraction techniques for survivability of SnAg leadfree packaging architectures under shock and vibration”, Electronic Components and Technology Conference, 2008, 1036-1047.
- [31] Signetics, (https://www.signetics.com/img/FCFBGA_MUF.pdf)
- [32] Yan Tee, T., et al., “Novel Numerical and Experimental Analysis of Dynamic Responses under Board Level Drop Test”, IEEE, 2004, 133-140.
- [33] Liu, S., et al., “Drop Test and Simulation of Portable Electronic Devices”, 6th International Conference on Electronic Packaging Technology, 2005, 1-4.
- [34] Chung, S. and Kwak, J.B., “Comparative Study on Reliability and Advanced Numerical Analysis of BGA Subjected to Product-Level Drop Impact Test for Portable Electronics”, MDPI (Electronics), 2020, 9(9), 1515.
- [35] Scheijgrond, P. L. W., et al., “Digital image correlation for analyzing portable electronic products during drop impact tests”. 6th International Conference on Electronic Packaging Technology, 2005, 121-126.
- [36] Zhou, C. Y., et al., “Drop/impact tests and analysis of typical portable electronic devices”, International Journal of Mechanical Sciences, 2008, 50(5), 905-917.
- [37] Yeh, Meng-Kao and Huan, Tzu-Heng, “Drop Test and Finite Element Analysis of Test Board”, Procedia Engineering, 2014, 79, 238-243.
- [38] Wang, Y., et al., “Modeling and simulation for a drop-impact analysis of multi-layered printed circuit boards”, Microelectronics Reliability, 2005, 46, 558-573.
- [39] Yan Tee, T., “Effect of impact pulse parameters on consistency of board level drop test and dynamic responses”, Electronic Components and Technology Conference, 2005, 1, 665-673.

- [40] Lall, P. et al., “Cohesive-Zone Modeling and Life-Prediction of Leadfree Electronics Under Shock-Impact”, Society for Experimental Mechanics – SEM Annual Conference and Exposition on Experimental and Applied Mechanics, 2009.
- [41] LS- DYNA Keyword User’s Manual Volume I. 2017, Livermore Software Technology Corporation: Livermore, CA.
- [42] D. Y. R. Chong et al., "Drop reliability performance assessment for PCB assemblies of chip scale packages"(CS^P)", 7th Electronic Packaging Technology Conference, 2005, 262-269.
- [43] Diehl, T., et al, “Using Digital Signal Processing (DSP) to Significantly Improve the Interpretation of ABAQUS/Explicit Results”, Proceedings – ABAQUS User’s Conference, United Kingdom, May 25-28, 1999.
- [44] Kordowski, P., et al., “Miniaturized flight data recorder for unmanned aerial vehicles and ultralight aircraft^{ts}”, 5th IEEE International Workshop on Metrology for AeroSpace (Italy), 2018, 484-488.
- [45] Olivares, G., Gomez, L., Espinosa de los Monteros, J., Baldrige, R., and Marco, R., “Annex B NIAR Final Report Task A14: UAS Ground Collision Severity Evaluation 2017-2018”, Federal Aviation Administration, Report DOT/FAA/AR-XX/XX, 2019.
- [46] Olivares, G., Gomez, L., Espinosa de los Monteros, J., Baldrige, R., Zinzuwadia, C., and Aldag, T., “Volume II – UAS Airborne Collision Severity Evaluation – Quadcopter”, Federal Aviation Administration, Report DOT/FAA/AR-XX/XX, 2017.
- [47] Olivares, G., Gomez, L., Marco, R., Ly, H., Calderon del Rey, J., Duling, C., Zwiener, M. and Perrin, Z., “Volume VI – UAS Airborne Collision Severity Evaluation – 14 CFR Part 29 Rotorcraft”, Federal Aviation Administration, Report DOT/FAA/AR-XX/XX, 2022.
- [48] Olivares, G., Gomez, L., Espinosa de los Monteros, J., Baldrige, R., and Zinzuwadia, C., NIAR Internal Report UAS-0001 Search and Rescue Drone, 2019.
- [49] Olivares, G., Gomez, L., Marco, R., “Volume VII – UAS Airborne Collision Severity Evaluation – 14 CFR Part 23 General Aviation”, Federal Aviation Administration, Report DOT/FAA/AR-XX/XX, 2022.
- [50] Man, M., Lovingfoss, R. and Hooper, E., “Cytec Cycom 5320-1 T650 3k-PW Fabric Qualification Material Property Data Report”, NCAMP Test Report Number CAM-RP-2012-017 Rev NC, 2015.
- [51] Olivares, G., Gomez, L., Baldrige, R., Marco, R., Ly, H., “Large sUAS Airborne Collision Severity Evaluation with 14 CFR 25 Aircraft – ATO Office of Safety”, Federal Aviation Administration, Report DOT/FAA/AR-XX/XX, 2020.
- [52] D’Altri, A. M., et al., “A 3D detailed micro-model for the in-plane and out-of-plane numerical analysis of masonry panels”, Computers & Structures, 2018, 206, 18-30.
- [53] A. Thomas, M. et al., “Constitutive Soil Properties for Cuddeback Lake, California and Carson Sink, Nevada”, National Aeronautics and Space Administration, Report NASA/CR-2008-215345, 20–8.